JOURNAL OF THE
AERO/SPACE SCIENCES

VOLUME 25 OCTOBER, 1958 NUMBER 10

ST. LOUIS
OCT 8 1958
PUBLIC LIBRARY

CONTENTS

Magnetogasdynamics of Hypersonic Couette Flow ..... Z. O. BLEVISS 601

The Transonic Flow Field of an Axial Compressor Blade Row .... JAMES E. MCCUNE 616

Thermal Stress in Curved Beams ..... BRUNO A. BOLEY AND EUVAL S. BARREKETTE 627

The Boundary-Layer Equation for Axially Symmetric Flow Past a Body of Revolution —Motion of a Sphere ..... DAVID MEKSYN 631

Utilization of Experimental Results in Flutter Analysis ... ERIK MOLLÖ-CHRISTENSEN 635

An Experimental Study of the Turbulent Boundary Layer Behind the Initial Shock Wave in a Shock Tube ..... WALTER A. MARTIN 644

Readers' Forum 653

Published by
INSTITUTE OF THE AERONAUTICAL SCIENCES, INC.

JOURNAL OF THE AERO/SPACE SCIENCES

(formerly Journal of the Aeronautical Sciences)

Editor: W. R. SEARS

Director, Graduate School of Aeronautical Engineering, Cornell University

Associate Editor: ROBERT R. DEXTER *Managing Editor:* RITA J. TURINO

Editorial Assistant: CAROLINE TAYLOR

Editorial Committee

Aerodynamics and Fluid Mechanics

Holt Ashley
H. Julian Allen
Dean R. Chapman
Francis H. Clauser
Hugh L. Dryden
John C. Evvard
Antonio Ferri
Alexander Flax
Wallace D. Hayes
R. T. Jones
Carl Kaplan
H. W. Liepmann
C. C. Lin
H. F. Ludloff
Harold Luskin
Clark B. Millikan
Henry T. Nagamatsu
H. J. E. Reid
George S. Schairer
G. B. Schubauer
John Stack
Theodore Theodorsen
Arthur N. Tifford
Th. von Kármán

Flight Testing

R. R. Gilruth
Melvin N. Gough
W. L. Howland
W. F. Milliken, Jr.

Rotating Wing Aircraft

F. B. Gustafson
K. H. Hohenemser
Bartram Kelley
R. B. Maloy
Ralph McClarren
R. H. Miller
R. H. Prewitt
Igor I. Sikorsky

Structures

John E. Duberg
R. R. Heldenfels
N. J. Hoff
Samuel Levy
J. F. McBrearty
W. Ramberg
E. E. Sechler
F. R. Shanley
C. R. Strang
S. Timoshenko

Meteorology

C. F. Brooks
D. M. Little
F. W. Reichelderfer
K. C. Spengler

Vibration and Flutter

Lee Arnold
M. A. Biot
R. L. Bisplinghoff
Harold A. Cheilek
I. E. Garrick
Martin Goland

Aircraft Design

W. E. Beall
E. H. Heinemann
Hall L. Hibbard
Richard Hutton
C. L. Johnson
A. A. Kartveli
F. K. Teichmann

Electronics

K. C. Black
M. V. Kiebert, Jr.
David S. Little
Paul Rosenberg
Giles J. Strickroth

Physiologic Problems

H. G. Armstrong
Louis H. Bauer
Robert J. Benford
W. Randolph Lovelace, II
Ross A. MacFarland

Flight Propulsion

William Bollay
George W. Brady
R. P. Kroon
Frank E. Marble
Abe Silverstein
E. S. Taylor

Instruments

Alan G. Binnie
Charles H. Colvin
Frank R. Cook
C. S. Draper
S. G. Eskin
C. F. Savage
R. C. Sylvander

SUBSCRIPTION RATES

JOURNAL OF THE AERO/SPACE SCIENCES (formerly Journal of the Aeronautical Sciences), Published Monthly. United States and Possessions: 1 Year, $15.00; Single Copies, $1.50. Foreign Countries Including Canada (American Currency Rates): 1 Year, $16.00; Single Copies, $1.50.

AERO/SPACE ENGINEERING, Published Monthly. United States and Possessions: 1 Year, $5.00; Single Copies, $0.50. Foreign Countries Including Canada (American Currency Rates): 1 Year, $6.00; Single Copies, $0.50.

Notices of change of address should be sent to the Institute at least 30 days prior to actual change of address.

Manuscripts for publication, proofs, and all correspondence should be addressed to the Editorial Office of the JOURNAL.

Publication Office, 20th and Northampton Sts., Easton, Pa. Correspondence regarding subscriptions may be addressed to the Editorial Office of the JOURNAL OF THE AERO/SPACE SCIENCES, 2 East 64th Street, New York 21, N.Y.

© Copyright, 1958, by the Institute of the Aeronautical Sciences, Inc.

Second-Class Mail Privileges Authorized at Easton, Pa. Acceptance for mailing at a special rate of Postage provided for in the Act of August 24, 1912. Authorized April 29, 1937.

JOURNAL OF THE AERO/SPACE SCIENCES

VOLUME 25 OCTOBER, 1958 NUMBER 10

Magnetogasdynamics of Hypersonic Couette Flow

Z. O. BLEVISS*

Douglas Aircraft Company, Inc.

SUMMARY

When the gas in a high-speed laminar boundary layer becomes ionized due to viscous heating, it becomes an electrical conductor and it can be made to interact with a magnetic field to alter skin friction, heat transfer, total drag, etc. The calculation of magnetogasdynamic effects on high-speed laminar boundary layers is extremely complex and no solutions with realistic assumptions have been obtained. A very simple pure shear flow, usually called Couette flow, is investigated in this paper because it contains many important features of boundary-layer flow and because it can be solved exactly with a minimum of assumptions about the gas.

Couette flow is the fluid motion produced when a viscous fluid contained between two infinitely extended plane parallel walls is set into steady motion by the relative movement of the walls in their own planes. The exact solution for compressible Couette flow but with no magnetic field was given by Illingworth.[2] Liepmann and Bleviss[3] showed how easily effects like equilibrium dissociation and ionization can be included in the solution and drew attention to the fact that a study of this type of flow is very helpful in understanding the flow in a high-speed laminar boundary layer.

In the present paper, the Couette flow problem is extended to include a uniform externally imposed magnetic field normal to the walls. Assuming thermodynamic equilibrium and reasonable variations of electrical conductivity, viscosity, and Prandtl Number with temperature, numerical solutions are presented for air for the case of the insulated wall (no heat transfer to the wall) for Mach Numbers from 10 to 30 and for the case of heat transfer for Mach Numbers of 20 and 30. The effects of the magnetic field upon the velocity, temperature, electrical current density, and induced magnetic field distributions and upon the skin friction, heat transfer, and total drag—i.e., skin friction plus the magnetic stress due to the interaction of the electrically conducting fluid with the magnetic field—are shown.

Comparing results with magnetic field to results without magnetic field for a given high-speed laminar boundary layer, the present investigation shows that relatively weak magnetic fields produce large increases in the total drag, large reductions in the skin friction, and at the same time have relatively little effect on the heat transfer. Whereas the total drag without magnetic field is skin-friction drag, the total drag with magnetic field is primarily magnetic drag. This implies that if the comparison is made on the basis of the same total drag the heat transfer for the magnetic case will be much less than that for the nonmagnetic case.

The expected qualitative and quantitative applicability of the Couette flow results to the boundary layer is discussed.

Received March 7, 1958. Revised and received June 25, 1958.

* Design Specialist, Aerodynamics Research Group.

The author would like to acknowledge many stimulating and enlightening discussions with Prof. H. W. Liepmann, whose continual interest has been of great benefit in this problem. The general features of this problem and some preliminary results were presented by Professor Liepmann at the Second Lockheed Magneto-hydrodynamics Symposium, Palo Alto, California, Dec. 16, 1957.

SYMBOLS

B	=	magnetic field strength (magnetic flux density). m.k.s. unit is weber/meter^2. Unit used in presentation of results is gauss (1 weber ÷ meter^2 = 10^4 gauss).
B_0	=	imposed magnetic field (see Fig. 1)
B_x, B_y, B_z	=	Cartesian components of $\vec{B}$ (see Fig. 1)
C_d	=	$\tau_\infty/[(1/2)\rho_\infty U^2]$ = total drag coefficient
C_f	=	$\tau_w/[(1/2)\rho_\infty U^2]$ = skin-friction coefficient
C_h	=	$q_w/(h_w - h_r)\ \rho_\infty U$ = heat-transfer coefficient
$C_{h\infty}$	=	$q_\infty/(h_w - h_r)\ \rho_\infty U$ = heat-transfer coefficient for moving wall
C_p	=	specific heat at constant pressure
E	=	electric field intensity (volt/meter)
h	=	specific enthalpy (enthalpy per unit mass)
$\bar{h}$	=	h/h_∞
$h_{0_{max}}$	=	maximum enthalpy for zero magnetic field
j	=	current density (ampere/meter^2)
J	=	total current per unit length in x direction (ampere/meter)
k	=	thermal conductivity
M_∞	=	free-stream Mach Number
N_H	=	$\sqrt{\sigma_{0_{max}}/\eta_\infty}\ B_0\delta$ = Hartmann Number
p	=	fluid mechanical pressure
$\boldsymbol{P}$	=	fluid mechanical stress tensor
P_{ik}	=	components of fluid mechanical stress tensor [see Eq. (6c)]
Pr	=	$\eta C_p/k$ = Prandtl Number
q	=	heat flux
R_M	=	$\mu\sigma_{0_{max}}\delta U$ = magnetic Reynolds Number

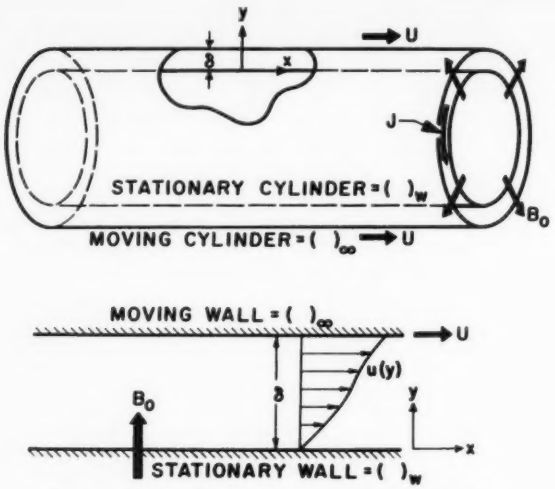

FIG. 1. Couette flow with transverse magnetic field.

R_δ = $\rho_\infty U\delta/\eta_\infty$ = fluid Reynolds Number based on free-stream properties and δ
T = absolute temperature
$\bar{T}$ = T/T_∞
$\boldsymbol{T}$ = Maxwell stress tensor
T_{ik} = components of Maxwell stress tensor [see Eq. (6d)]
u = velocity component in x direction (see Fig. 1)
$\bar{u}$ = u/U
U = velocity of moving wall or free stream (see Fig. 1)
V = total velocity
x, y, z = right-hand Cartesian coordinate system (see Fig. 1)
$\bar{y}$ = y/δ
γ = ratio of specific heats in free stream = 1.40
δ = distance between walls or boundary-layer thickness (see Fig. 1)
δ_{ik} = components of unit tensor (Kronecker delta)
ϵ = dielectric constant (farad/meter)
η = viscosity
$\bar{\eta}$ = η/η_∞
μ = magnetic permeability (henry/meter)
ρ = density
σ = electrical conductivity (mho/meter)
$\sigma_{0_{max}}$ = maximum electrical conductivity for zero magnetic field
$\bar{\sigma}$ = σ/σ_{0max}
τ = shear stress in Couette flow
$\bar{\tau}$ = τ/τ_w
$\boldsymbol{\tau}$ = viscous part of fluid mechanical stress tensor
τ_{ik} = components of viscous part of fluid mechanical stress tensor

Subscripts

$( )_0$ = zero magnetic field
$( )_r$ = recovery conditions—i.e., conditions at stationary wall with zero heat transfer
$( )_w$ = conditions at stationary wall or body (see Fig. 1)
$( )_\infty$ = conditions at moving wall or in free stream (see Fig. 1)
$\vec{( )}$ = a vector

INTRODUCTION

AT HYPERSONIC SPEEDS, the gas in a high-speed laminar boundary layer becomes ionized due to viscous heating. The gas then becomes an electrical conductor and it can be made to interact with a magnetic field to alter the skin friction, heat transfer, total drag, etc. The exact calculation of magnetogasdynamic effects on high-speed laminar boundary layers is extremely complicated and no solutions with realistic assumptions have been obtained. Some indication of these difficulties can be found in reference 1, where the incompressible, laminar, flat-plate boundary layer with a uniform magnetic field normal to the plate is treated approximately. Because of these difficulties, a very simple pure shear flow that contains many of the important features of boundary-layer flow is investigated here. The really significant advantage gained by resorting to this simpler problem is that it can be solved exactly for all Mach and Reynolds Numbers with a minimum number of assumptions about the gas. This simple flow, usually called Couette flow, then represents an excellent test case to study the effects of a magnetic field on recovery temperature, skin friction, heat transfer, etc. because the physics of the problem is not hidden behind a formidable mathematical and numerical apparatus.

Couette flow is the fluid motion produced when a viscous fluid contained between two infinitely extended plane parallel walls is set into steady motion by the relative movement of the walls in their own planes (see lower sketch in Fig. 1). Consider the two walls at $y = 0$ and $y = \delta$ and let the upper wall move with constant velocity U relative to the lower wall which will be taken to be stationary. In the comparison with the boundary layer the moving wall corresponds to the free stream outside the boundary layer, the stationary wall corresponds to the body, and δ is the boundary-layer thickness. When the electromagnetic boundary conditions are considered it will be found convenient to interpret Couette flow as an approximation to the fluid motion produced in a viscous fluid contained in the annular region between two coaxial circular* cylinders of infinite length sliding relative to each other along their common axis (see upper sketch in Fig. 1), the thickness δ of the annular region being small compared with the cylinder radii. This configuration corresponds to a boundary layer on the slender afterbody of a body of revolution. The notation in this report has been chosen to correspond as closely as possible to the usual boundary-layer notation. The stationary wall will be referred to as the "wall" and all quantities there will be denoted by the subscript w—i.e., τ_w, T_w, etc. Except where specifically stated otherwise, the upper wall ($y = \delta$) will correspond to the "free stream" and will be denoted by the subscript ∞ (the "free-stream" velocity is denoted by U).

The exact solution for compressible Couette flow when no electromagnetic effects are considered was given by Illingworth.[2] Liepmann and Bleviss[3] showed

* The cylinder cross sections need not be circular. However, the normal distance δ between the cylinders must be constant around the circumference and must be small compared with the smallest radius of curvature. For convenience, the cylinder cross sections will always be taken circular.

how easily effects like equilibrium dissociation and ionization can be included in this solution, and they drew attention to the fact that a study of this type of flow can be very helpful in understanding the flow in a high-speed laminar boundary layer.

In the present report, the Couette flow problem is extended to include a uniform externally applied magnetic field normal to the walls. In the case of the sliding cylinders, the magnetic field will be radial (see Fig. 1). Unless stated otherwise, the magnetic field will be attached to the stationary wall. This is the case that is most interesting practically.

General Equations

Before writing down the equations that govern the Couette flow problem, it is helpful to write down some of the general equations and discuss briefly certain features of these equations. The steady continuum flow of a viscous, compressible, electrically conducting, electrically neutral (i.e., charge free) gas is considered. The rationalized m.k.s. system of electromagnetic units is used.

From Maxwell's equations there is obtained

$$\text{curl } \vec{E} = 0 \tag{1}$$

$$\text{div } \vec{B} = 0 \tag{2}$$

$$\vec{j} = \text{curl } (\vec{B}/\mu) \tag{3}$$

Ohm's law gives

$$\vec{j} = \sigma(\vec{E} + \vec{V} \times \vec{B}) \tag{4}$$

where the conductivity σ is assumed to be a scalar. The $\vec{V} \times \vec{B}$ term is an effective electric field arising from the motion of the conducting fluid relative to the magnetic field.

The fluid mechanical equations will now be discussed. The continuity equation has its usual form

$$\text{div } (\rho \vec{V}) = 0 \tag{5}$$

A convenient form of the momentum equation is

$$\text{div } (\rho \vec{V}\vec{V} - \boldsymbol{P} - \boldsymbol{T}) = 0 \tag{6a}$$

The dyadic product $\vec{V}\vec{V}$ in the transport term denotes the second-order tensor with the components

$$(\vec{V}\vec{V})_{ik} = V_i V_k \tag{6b}$$

$\boldsymbol{P}$ is the usual fluid mechanical stress tensor with the components

$$P_{ik} = -p\delta_{ik} + \tau_{ik} \tag{6c}$$

where τ_{ik} is the viscous part of the tensor (see, e.g., reference 4, pp. 333 to 338). $\boldsymbol{T}$ is the Maxwell stress tensor with the components

$$T_{ik} = (B_i B_k/\mu) + \epsilon E_i E_k - (1/2)\,[(|B|^2/\mu) + \epsilon|E|^2]\,\delta_{ik} \tag{6d}$$

Div $\boldsymbol{T}$ is equal to the ponderomotive force per unit volume $\vec{j} \times \vec{B}$ acting on the fluid due to the interaction of the current and the magnetic field. Inserting the $\vec{j} \times \vec{B}$ term in Eq. (6a) leads to the more usual form of the momentum equation

$$\text{div } (\rho \vec{V}\vec{V} - \boldsymbol{P}) = \vec{j} \times \vec{B} \tag{6e}$$

The energy equation can be written in the following equivalent forms:

$$\text{div } \{\rho \vec{V}[h + (V^2/2)] - \boldsymbol{\tau}\vec{V} + \vec{q}\} = (\vec{j}^2/\sigma) + \vec{V}\cdot(\vec{j} \times \vec{B}) = \vec{j}\cdot\vec{E} \tag{7a}$$

$$\text{div } \{\rho \vec{V}[h + (V^2/2)] - \boldsymbol{\tau}\vec{V} + \vec{q} + \vec{E} \times (\vec{B}/\mu)\} = 0 \tag{7b}$$

Here, h is the specific enthalpy, $\vec{q}$ is the heat flux vector, and $\boldsymbol{\tau}$ is the viscous part of the fluid mechanical stress tensor [see Eq. (6c)]. $\vec{E} \times (\vec{B}/\mu)$ is the Poynting vector and div $[\vec{E} \times (\vec{B}/\mu)]$ represents the rate of transport (per unit area) of electromagnetic energy out of a fluid element.

In general, the boundary conditions to be imposed on $\vec{E}$ and $\vec{B}$ are not easily determined. In the Couette flow problem, $\vec{E}$ will be set equal to zero—i.e., there will be no self-generated or externally imposed electric field. The physical situation that corresponds to $\vec{E} = 0$ is discussed in the next section. This means that no energy can be added to or removed from a fluid element by electromagnetic means and the energy equation reduces to its usual fluid mechanical form. The effect of the magnetic field is then confined to retarding the flow and increasing the dissipation of the energy of motion into heat.

Equations for Couette Flow With $\vec{E} = 0$

It is clear from the simple geometry and type of motion that the velocities in the y and z directions will be zero for Couette flow—i.e., $v = w = 0$—and that nothing can vary in the x and z direction—i.e., $\partial/\partial x = \partial/\partial z = 0$. The continuity equation is then identically satisfied and the transport terms in the momentum and energy equations are identically zero. From the z component of the momentum equation it follows, as expected, that $B_z = 0$, the subscript denoting the component of $\vec{B}$. Eq. (2) reduces to

$$dB_y/dy = 0$$

so that

$$B_y = \text{constant} = B_0 \tag{8}$$

where B_0 is the uniform externally imposed magnetic field.

With $\vec{E} = 0$, Eqs. (3) and (4) become

$$j = -(1/\mu)\,(dB_x/dy) = \sigma B_0 u \tag{9}$$

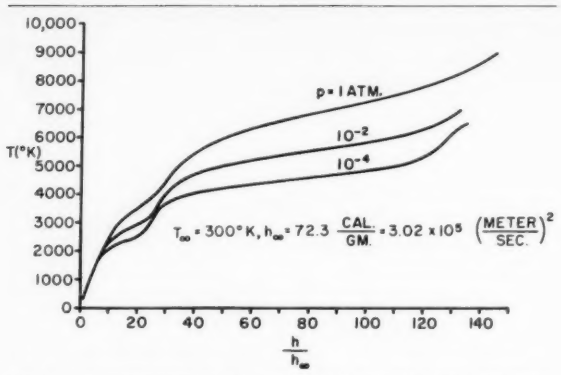

FIG. 2. Temperature as a function of enthalpy and pressure.

where j denotes the z (and only) component of the current density vector in the right-hand coordinate system of Fig. 1. In this equation and in the remainder of this report μ is taken to be constant and equal to its vacuum value.

The x and y components of the momentum equation reduce to

$$(d\tau/dy) + (B_0/\mu)(dB_x/dy) = (d\tau/dy) - \sigma B_0^2 u = 0 \quad (10)$$

$$(dp/dy) + (d/dy)(B_x^2/2\mu) = (dp/dy) - \sigma B_0 B_x u = 0 \quad (11)$$

The first forms of these equations come from Eq. (6a) and contain the Maxwell stress tensor components, while the second forms come from Eq. (6e). The two forms are readily interchanged by using Eqs. (9). τ is used here to denote the shear stress component τ_{yx}, this being the only viscous component that remains.

The energy equation reduces to

$$(d/dy)(\tau u - q) = 0 \quad (12)$$

q denotes the y component of the heat flux vector, this being the only component that remains.

The thermodynamics that will be needed here is the same as that described in reference 3 so that only a brief description will suffice. Thermodynamic equilibrium is assumed throughout. The probable validity of this assumption in boundary-layer problems will be discussed later. The equilibrium thermodynamic properties of air, the gas used in all the calculations in this report, are now available in a number of reports for wide ranges of temperature and pressure (see, e.g., references 5–9). The tables and/or Mollier charts in these references contain the thermal and caloric equations of state [i.e., $f(p, \rho, T) = 0$ and $h = h(p, T)$] and thus define completely the thermodynamic state of the gas. Then a knowledge of any two thermodynamic variables yields all of the others. In this report, as in reference 3, h rather than T turns out to be the natural variable, the other variable being p. Thus, all quantities that depend on the state of the gas will be considered to be functions of h and p. A plot of $T(h, p)$ obtained from these references is given in Fig. 2. h/h_∞ rather than h is used in this plot for convenience in the calculations where h_∞ is the free-stream enthalpy used in the calculations.

The usual Newtonian expression for τ will be assumed—i.e.,

$$\tau = \eta(du/dy) \quad (13)$$

where η denotes the viscosity coefficient.

Likewise, the usual expression for q will be assumed,

$$q = -k(dT/dy) \quad (14)$$

Here, k is an effective thermal conductivity that combines the usual thermal conductivity and a thermal conductivity that can be defined for the heat transfer in the y direction that arises because the dissociation energies are transported by the mass diffusion that is, in turn, caused by the variations in the gas composition (see, e.g., reference 10). The sign is chosen so that heat flows from higher to lower temperatures. As noted above, it is convenient to write q in terms of h and p. Thus, Eq. (14) can be rewritten in the following form, using the fact that $h = h(p, T)$:

$$q = (\eta/Pr)[-(dh/dy) + (\partial h/\partial p)_T (dp/dy)] \quad (15)$$

Here $Pr = \eta C_p/k$ is an effective Prandtl Number and $(\partial h/\partial p)_T$ is to be obtained from the equation of state of the gas. In reference 3 (no magnetic field) the pressure was strictly constant and the second term did not appear. However, here a new feature arises, in that the induced-magnetic-pressure variations induce fluid pressure variations [see Eq. (11)], and both terms in Eq. (15) would presumably have to be carried in general.

The transport parameters σ, η, and Pr will now be briefly considered. For a more complete discussion see Appendix (A). In general, these parameters are all functions of h and p. η and σ are given as functions of h and p in Figs. 3 and 4, respectively. Pr is assumed to be constant in the formulas and calculations that follow. However, it should be emphasized that it is a simple matter to include a variable Prandtl Number in this problem if it should be desirable, and the procedure will be indicated in the next section.

The two Eqs. (9) together with Eqs. (10), (11), (12), (13), and (15) constitute a system of seven equations to be solved simultaneously for the seven unknowns B_x, u, j, τ, p, q, and h. Since there are six first-order ordinary differential equations to be solved [Eqs. (9) (omitting j), (10), (11), (12), (13), and (15)], six boundary conditions are required. It should be noted that, if $\vec{E}$ were not zero, more equations and boundary conditions would be involved.

Five of the boundary conditions are the usual ones imposed by fluid mechanical considerations. They are

$$\text{at } y = 0: \quad u = 0, \quad h = h_w \text{ or } q = q_w$$

$$\text{at } y = \delta: \quad u = U, \quad h = h_\infty, \quad p = p_\infty$$

The sixth boundary condition is to be imposed on B_x and requires some discussion. First, consider the physical situation that satisfies the condition $\vec{E} = 0$. This can be seen by referring to the sliding cylinder configuration in Fig. 1. It is clear that the axial velocity u and the radial magnetic field B_0 will lead to a circumferential current density given by Eq. (9). If δ is constant and flow conditions are identical around the circumference, the distribution of electric current being driven around the annulus by the effective electric field $\sigma(\vec{V} \times \vec{B})$ is the same at all positions around the circumference, and, thus, no electric field will be self-generated. If, in addition, no external electric field is imposed, the current is driven only by the effective electric field $\sigma(\vec{V} \times \vec{B})$ and it is evident from Eq. (4) that this configuration satisfies the condition $\vec{E} = 0$. Now, note that this configuration is essentially a multilayer coil (solenoid) of infinite length, the magnitude and distribution of the current being known, of course, only after the problem is solved. It is well known that such a coil induces a magnetic field only in the axial direction and that the induced magnetic field is zero at the outer edge of the windings and is constant everywhere inside the coil. (See, for example, reference 18.) Thus, the boundary condition on B_x is

$$B_x = 0 \quad \text{at} \quad y = \delta$$

Since the current has the same sign throughout the annulus, B_x will increase monotonically from zero at the moving cylinder to a maximum value at the stationary cylinder.

To completely specify the problem it is necessary to make some remarks about the properties of the walls. Since the moving wall corresponds to the non-ionized free stream, its conductivity will be assumed zero. It is not necessary to specify μ for the moving wall although the vacuum value is indicated. If the moving wall were an electrical conductor, currents and a magnetic field would be induced in it and it would be necessary to specify μ. The solution is unaffected by the properties of the stationary wall (or body). Since the magnetic field is attached to the body no currents can be induced in it. If the body is ferromagnetic, μ and B_x will change discontinuously at $y = 0$ but the solution for $y \geq 0$ will be unaffected.

At this point, a number of properties of the flow can be deduced with little effort.

Changing the sign of B_0 changes the sign of j and B_x but does not essentially alter the solution. The reason is that the magnetic terms in the momentum Eqs. (10) and (11) enter as products or squares of these quantities. Thus, $\vec{j} \times \vec{B}_0$, which is the magnetic term in Eq. (10), always opposes the fluid motion, whatever the sign of B_0. Likewise, $\vec{j} \times \vec{B}_x$, which is the magnetic pressure term in Eq. (11), always alters the fluid pressure in the same way regardless of the sign of B_0. It should be pointed out, however, that there is a way in which changing the sign of B_0 will alter the solution. This will occur if B_0 changes sign in the z direction—i.e., circumferentially around the annulus—because then the current flow around the annulus changes sign and an electric field will be generated. Note that changing the sign of B_0 in the x direction will not affect the solution.

The first forms of Eqs. (10) and (11) can be integrated to give

$$\tau + (B_0 B_x/\mu) = \text{constant} = \tau_\infty \tag{16}$$

$$p + (B_x^2/2\mu) = \text{constant} = p_\infty \tag{17}$$

using the fact that $B_x = 0$ at $y = \delta$. These equations show that both the shear stress τ and the pressure p decrease monotonically from the free stream to the wall. The well-known possibility of "holding a conducting gas away from a wall" by magnetic pressure is indicated here.

The total current J and the maximum value of the induced magnetic field are, using Eqs. (9),

$$J = \int_0^\delta j\,dy = -(1/\mu)\int_{(B_x)_{max}}^0 dB_x = (B_x)_{max}/\mu = B_0\int_0^\delta \sigma u\,dy \tag{18}$$

If the quantities under the last integral are made nondimensional using maximum values, there is obtained

$$J = (B_x)_{max}/\mu = \sigma_{max} B_0 \delta U \int_0^1 (\sigma/\sigma_{max})(u/U)d(y/\delta) \tag{19}$$

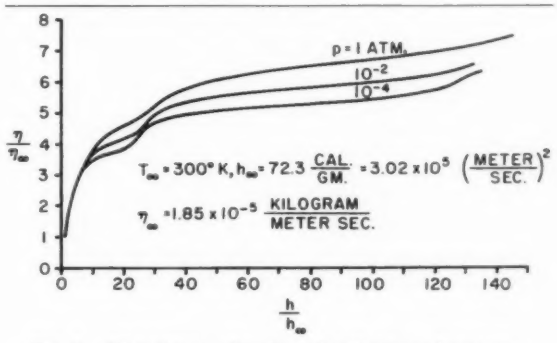

FIG. 3. Viscosity as a function of enthalpy and pressure.

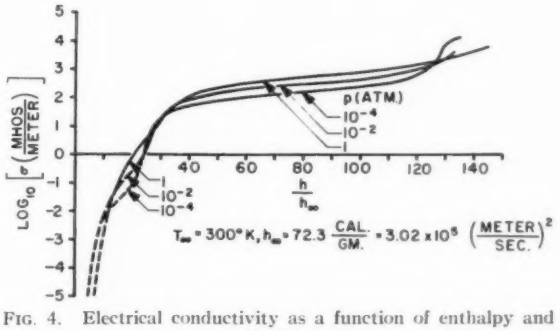

FIG. 4. Electrical conductivity as a function of enthalpy and pressure.

For a given set of boundary conditions, σ/σ_{max} and u/U must be functions only of y/δ and, therefore, the value of the integral is independent of δ. This means that the magnitudes of the total current and the induced magnetic field are determined by the product $B_0\delta$ for given boundary conditions. It is clear that the B_x can be made small or large compared with B_0 by varying δ. The actual relative magnitudes of B_x and B_0 in a given problem when the boundary conditions B_0 and δ are prescribed will depend, of course, on the other factors in Eq. (19).

From Eq. (19) it is seen that B_x will be small compared with B_0 if σ_{max} is small enough, or, better, if the magnetic Reynolds Number $\sigma_{max}\mu U\delta$ is much less than unity. It should be pointed out that, even when B_x is small compared with B_0, it is not correct to neglect B_x compared with B_0 in the general magnetic force term $\vec{j} \times \vec{B} = \vec{j} \times (\vec{B}_0 + \vec{B}_x) = \vec{j} \times \vec{B}_0 + \vec{j} \times \vec{B}_x$. (One might be tempted to do this in order to obtain a simpler problem which is a close approximation to the original problem.) One cannot neglect the B_x term because $\vec{j} \times \vec{B}_0$ and $\vec{j} \times \vec{B}_x$ are normal to each other and are therefore involved in different components of the momentum equation [see Eqs. (10) and (11)]. This means that $\vec{j} \times \vec{B}_x$ must be compared with other terms in its momentum equation (i.e., dp/dy) rather than with $\vec{j} \times \vec{B}_0$ to determine whether or not it is negligible. Furthermore, it should be noted that setting $B_x = 0$ and retaining $\vec{j} \times \vec{B}_0$ would be an inconsistent procedure because $\vec{j}$ would then be zero [see Eqs. (9)]; indeed, if B_x were strictly set equal to zero all magnetic effects would disappear. This inconsistency is not evident if only the second form of Eq. (10) is considered since B_x is apparently not involved. However, the equivalent first form of Eq. (10) clearly shows the difficulty.

Since it is necessary to retain $\vec{j} \times \vec{B}_0$ in the present problem, it is necessary to retain B_x in Eq. (10). However, it may be possible to neglect B_x in Eq. (11) if the free-stream pressure is not too low, regardless of the relative magnitudes of B_x and B_0. In this paper it will be assumed that B_x can be neglected in Eq. (11) and that, therefore, the pressure is constant throughout the flow field. This assumption is justified later by substituting the calculated results into Eqs. (11) and (15) and showing that the pressure effects are actually negligible.

The foregoing remarks about the induced magnetic field are easily generalized. If the induced field is small compared with the applied field, the induced field component parallel to the applied field can be set equal to zero to obtain a simpler problem which is a close approximation to the original problem. Whether or not the induced field components normal to the applied field can be neglected must be determined by considerations similar to those discussed above for the B_x component.

Solution of the Couette Flow Equations With p = Constant

With p constant, the system of equations and the boundary conditions may be summarized as follows:

$$j = -(1/\mu)\,(dB_x/dy) = \sigma B_0 u \tag{20}$$

$$(d\tau/dy) + (B_0/\mu)\,(dB_x/dy) = (d\tau/dy) - \sigma B_0^2 u = 0 \tag{21}$$

$$(d/dy)\,(\tau u - q) = 0 \tag{22}$$

$$\tau = \eta(du/dy) \tag{23}$$

$$q = -(\eta/Pr)\,(dh/dy) \tag{24}$$

At $y = 0$: $u = 0$, $h = h_w$ or $q = q_w$

At $y = \delta$: $u = U$, $h = h_\infty$, $B_x = 0$

Taking p to be constant greatly simplifies the task of solving the Couette flow equations. Aside from reducing the order of the system of equations by eliminating the unknown p, the unknown B_x is now uncoupled from u and h. In other words, after substituting Eqs. (23) and (24) into (21) and (22), the momentum and energy equations can be solved for u and h without explicitly involving B_x. B_x can then be obtained from Eq. (20). The coupling of all of the equations when p is not constant is due to the fact that η and σ are functions of the unknowns h and p, and p involves B_x explicitly. In the present simplified problem the momentum and energy equations are still coupled since η and σ are functions of the unknown h.

When the flow is incompressible, η, σ, C_p, and Pr are all constant, and the solution of this system of equations is trivial. Now, all of the equations are essentially uncoupled. For example, u can be obtained from Eq. (21) after substituting for τ from Eq. (23), then h and B_x can be obtained from Eqs. (22) and (20), respectively. The results are useful since they can be compared with the corresponding boundary-layer solution. The results are listed in Appendix (B) and some comparisons with Rossow's results are made.

Since $\eta(h, p_\infty)$ and $\sigma(h, p_\infty)$ are not given analytically it is obvious that an "exact" solution must be carried out numerically. It should be noted that attempts have been made to obtain relatively simple analytic solutions, by making crude but simple analytical approximations to $\eta(h, p_\infty)$ and $\sigma(h, p_\infty)$, but without success. Since the numerical solutions are easily obtained, it does not appear to be fruitful to attempt more involved analytical work. It might be mentioned that all of the numerical work was carried out by the author using slide rule and graphical integration.

The purpose of the present section is twofold—first to present the equations for the quantities of interest in the forms that were found most suitable for the numerical work, and second, to deduce, where possible

properties of the solution by examination of these equations.

As in references 2 and 3, the appropriate independent variable turns out to u instead of y. It will be convenient to write all of the results in nondimensional form.

The second form of Eq. (21) can be written

$$(d\tau/du)\ [\eta(du/dy)] - \eta\sigma B_0^2 u = 0$$

$$\tau d\tau = \eta\sigma B_0^2 u\, du$$

Integrating from the wall ($\tau = \tau_w$, $u = 0$) and solving for τ,

$$\tau = \tau_w \sqrt{1 + (2B_0^2/\tau_w^2)\int_0^u \eta\sigma u\, du}$$

This equation can be written in the nondimensional form

$$\bar{\tau} = \frac{\tau}{\tau_w} = \sqrt{1 + 2\left(\frac{N_H}{C_f R_\delta/2}\right)^2 \int_0^{\bar{u}} \bar{\eta}\bar{\sigma}\bar{u}\, d\bar{u}} \qquad (25)$$

where the following notation has been used:

$$\bar{u} = u/U, \quad \bar{\eta} = \eta/\eta_\infty, \quad \bar{\sigma} = \sigma/\sigma_{0max}$$

σ_{0max} = maximum conductivity when there is zero magnetic field

$C_f = \tau_w/(1/2)\rho_\infty U^2$ = skin-friction coefficient

$R_\delta = \rho_\infty U\delta/\eta_\infty$ = free-stream Reynolds Number based on the length δ

$N_H = B_0\delta\sqrt{\sigma_{0max}/\eta_\infty}$ = a Hartmann Number

σ_{0max} is used because it is easily obtained and is constant for a given set of boundary conditions. σ_{0max} is obtained from Fig. 4, using $\bar{h}_{0max}$, which may be calculated from the equation given in Appendix (C). Except for B_0, the zero subscript will always denote zero magnetic field. $\bar{\eta}$ and $\bar{\sigma}$ are functions of $\bar{u}$ through $\bar{h}(\bar{u}) = (h/h_\infty)\ (\bar{u})$, which must be determined before the integration can be carried out.

It is clear that $\bar{\tau} \geq 1$ and increases monotonically from unity at the wall ($\bar{u} = 0$) to a maximum value $\bar{\tau}_\infty$ at $\bar{u} = 1$. This was noted in the previous section, using a different argument. It is seen that B_0 and δ enter the equation as the product $B_0\delta$. This is a general result that can be deduced from the forms of Eqs. (20) and (21).

To obtain an equation for the enthalpy as a function of velocity—i.e., $h(u)$—the energy equation (22) is used. One integration can be carried out immediately to give

$$\tau u - q = -q_w \qquad (26)$$

Substituting for τ and q, using Eqs. (23) and (24), this becomes

$$\eta u(du/dy) + (\eta/Pr)\ (dh/dy) = -q_w$$

and can be further written as

$$[d(u^2/2)/dy] + (1/Pr)\ (dh/dy) = -(q_w/\eta)$$

To indicate how easily a variable Pr can be included in the results, it will be assumed, for the moment, that $Pr = Pr(h, p_\infty)$. Integrating the above equation,

$$\frac{u^2}{2} + \int_{h_w}^{h} \frac{dh}{Pr} = -q_w \int_0^y \frac{dy}{\eta} = -q_w \int_0^u \frac{du}{\tau} \qquad (27)$$

At the upper wall this becomes

$$(U^2/2) + \int_{h_w}^{h_\infty} (dh/Pr) = -q_w \int_0^U (du/\tau) \qquad (28)$$

The recovery enthalpy h_r is the enthalpy at the wall for zero heat transfer there—i.e., $h_w = h_r$ for $q_w = 0$. From Eq. (28),

$$\int_{h_\infty}^{h_r} (dh/Pr) = U^2/2 \qquad (29)$$

For constant Pr

$$\bar{h}_r = (h_r/h_\infty) = 1 + (Pr\,U^2/2h_\infty) = 1 + [(\gamma - 1)/2]Pr M_\infty^2 \qquad (30)$$

where γ is the ratio of specific heats for the free stream, M_∞ is the free-stream Mach Number, and it has been assumed that the free stream is cool enough so perfect gas formulas apply there. It is seen that the recovery temperature is not altered by the magnetic field. It is expected that the same result holds for the boundary layer just as in the incompressible case.[1] Note that, if pressure variations were included, there would be an additional term in Eq. (30) that would depend on the pressure gradient and then the magnetic field would alter the recovery temperature. For the cases calculated here this effect is negligible.

If q_w is eliminated between Eqs. (27) and (28) there obtains

$$\int_{h_w}^{h} (dh/Pr) = \int_{h_w}^{h_r} (dh/Pr) \times \left[\int_0^u (du/\tau)\Big/\int_0^U (du/\tau)\right] - (u^2/2) \qquad (31)$$

For constant Pr this can be written

$$\bar{h} = \bar{h}_w + (\bar{h}_r - \bar{h}_w)\left[\int_0^{\bar{u}} (d\bar{u}/\bar{\tau})\Big/\int_0^1 (d\bar{u}/\bar{\tau})\right] - [(\gamma - 1)/2]\ Pr M_\infty^2 \bar{u}^2 \qquad (32)$$

For zero magnetic field, $\bar{\tau} = 1$ and the ratio of integrals is simply $\bar{u}$. With a magnetic field the ratio of integrals is always greater than $\bar{u}$ except at the end points where it coincides with $\bar{u}$. This can be seen in the following way. Since $\bar{\tau}$ increases with $\bar{u}$ the integral in the numerator falls below $\bar{u}$, the deviation from $\bar{u}$ increasing with $\bar{u}$. Thus, if this integral were plotted against $\bar{u}$ it would be convex upward. Then, the ratio of integrals, which coincides with $\bar{u}$ at the end points, is also convex upward and hence must be greater than $\bar{u}$. This means that for the same value of $\bar{u}$ the enthalpy $\bar{h}$ with magnetic field is greater than the enthalpy $\bar{h}_0$ without magnetic field—i.e., $\bar{h}(\bar{u}) > \bar{h}_0(\bar{u})$—except at the end points

where they coincide. Since $\bar{u}(\bar{y})$ and $\bar{u}_0(\bar{y})$ are generally different, it cannot be concluded that $\bar{h}(\bar{y}) > \bar{h}_0(\bar{y})$. However, it is clear that the magnetic field will increase the temperature over part if not all of the flow field. This result is, of course, expected from the general physics of the problem.

For an insulated wall (zero heat transfer), $h_w = h_r$ and Eq. (32) becomes

$$\bar{h} = 1 + [(\gamma - 1)/2]\, PrM_\infty{}^2(1 - \bar{u}^2) \qquad (32a)$$

which is the result for zero magnetic field. This means that $\bar{h}(\bar{u}) = \bar{h}_0(\bar{u})$, not that $\bar{h}(\bar{y}) = \bar{h}_0(\bar{y})$. The expected increased temperatures show up through the fact that $\bar{u}(\bar{y})$ and $\bar{u}_0(\bar{y})$ are different.

An expression for the skin friction is obtained from Eq. (23), which can be written

$$\tau_w dy = \eta du/\bar{\tau}$$

Integrating and writing in nondimensional form, this becomes

$$(C_f R_\delta/2)\bar{y} = \int_0^{\bar{u}} \bar{\eta}(d\bar{u}/\bar{\tau})$$

Then

$$(C_f R_\delta/2) = \int_0^1 \bar{\eta}(d\bar{u}/\bar{\tau}) \qquad (33)$$

and the velocity distribution is given implicitly by

$$\bar{y} = \int_0^{\bar{u}} \bar{\eta}(d\bar{u}/\bar{\tau}) \Big/ \int_0^1 \bar{\eta}(d\bar{u}/\bar{\tau}) \qquad (34)$$

Comparing the skin friction with and without a magnetic field,

$$C_f R_\delta/(C_f R_\delta)_0 = \int_0^1 \bar{\eta}(d\bar{u}/\bar{\tau}) \Big/ \int_0^1 \bar{\eta}_0 d\bar{u} \qquad (35)$$

It is convenient to retain R_δ so that different boundary-layer thicknesses can be accounted for in any comparison with and without magnetic field. In general $\bar{\eta}(\bar{u}) > \bar{\eta}_0(\bar{u})$, except for the heat insulated wall, in which case $\bar{\eta}(\bar{u}) = \eta_0(\bar{u})$, this following from the previous results for $\bar{h}(\bar{u})$. Then, for the insulated wall the magnetic field decreases $C_f R_\delta$. At hypersonic speeds $\bar{h}$ will be large enough over most of the flow field so that $\bar{\eta}(\bar{h})$ varies slowly (see Fig. 3). Then $\bar{\tau}$ is expected to increase much more than $\bar{\eta}$ and it is expected that the magnetic field decreases $C_f R_\delta$ in general. This is the result obtained for incompressible Couette and boundary-layer flow.

The total drag (stress) on the body is the skin friction plus the force (stress) due to the interaction of the moving conductor and the magnetic field. One way to obtain the total drag is to integrate the force per unit volume $\vec{j} \times \vec{B}_0$ across the flow field and add τ_w to it. An equivalent procedure is to note that the total stress is the fluid mechanical plus the Maxwell stress [see Eq. (16)] and is equal to τ_∞. τ_∞ is obtained readily from the second form of Eq. (21) by integrating from 0 to δ—i.e.,

$$\tau_\infty - \tau_w = B_0{}^2 \int_0^\delta \sigma u\, dy$$

If the total drag (stress) coefficient is defined by

$$C_d = \tau_\infty/(1/2)\rho_\infty U^2$$

the result, in nondimensional form, is

$$C_d = C_f\left[1 + \left(\frac{N_H}{C_f R_\delta/2}\right)^2 \int_0^1 \frac{\bar{\eta}\bar{\sigma}\bar{u}\, d\bar{u}}{\bar{\tau}}\right] \qquad (36)$$

Eq. (23) can be written in the form

$$\tau_\infty dy = \eta du/(\tau/\tau_\infty)$$

Integrating from 0 to δ, writing in nondimensional form, and comparing with the total drag with no magnetic field gives

$$C_d R_\delta/(C_f R_\delta)_0 = \int_0^1 [\bar{\eta} d\bar{u}/(\tau/\tau_\infty)] \Big/ \int_0^1 \bar{\eta}_0 d\bar{u} \qquad (37)$$

It is clear that the $C_d R_\delta$ is always increased by a magnetic field even though $C_f R_\delta$ is reduced. Incompressible Couette and boundary-layer flows yield the same result.

The wall heat-transfer rate q_w can be obtained from Eq. (28). Taking Pr constant, using Eq. (30), and solving for q_w yields

$$q_w = (h_w - h_r)\left[Pr \int_0^U (du/\tau)\right]^{-1} \qquad (38)$$

Defining the heat-transfer coefficient by

$$C_h = q_w/(h_w - h_r)\rho_\infty U$$

Eq. (38) becomes

$$C_h = \left[\rho_\infty UPr \int_0^U (du/\tau)\right]^{-1}$$

This equation can be written in the following two nondimensional forms:

$$C_h = C_f\left[2Pr \int_0^1 (d\bar{u}/\bar{\tau})\right]^{-1} \qquad (39)$$

$$C_h = C_d\left\{2Pr \int_0^1 [d\bar{u}/(\tau/\tau_\infty)]\right\}^{-1} \qquad (40)$$

The ratio of the heat transfer with magnetic field to that without magnetic field is then

$$C_h R_\delta/(C_h R_\delta)_0 = [C_f R_\delta/(C_f R_\delta)_0]\left[\int_0^1 (d\bar{u}/\bar{\tau})\right]^{-1} =$$

$$\int_0^1 \bar{\eta}(d\bar{u}/\bar{\tau}) \Big/ \int_0^1 \bar{\eta}_0 d\bar{u} \int_0^1 (d\bar{u}/\bar{\tau}) =$$

$$[C_d R_\delta/(C_f R_\delta)_0]\left\{\int_0^1 [d\bar{u}/(\tau/\tau_\infty)]\right\}^{-1} \qquad (41)$$

It is seen that $(C_h R_\delta)/(C_h R_\delta)_0$ is always greater than $(C_f R_\delta)/(C_f R_\delta)_0$ and always less than $(C_d R_\delta)/(C_f R_\delta)_0$. The third expression, containing the three integrals, shows that the magnetic field decreases both the numerator and denominator, that they are roughly the same magnitude, and that, hence, the magnetic field does not have a large effect on $C_h R_\delta$.

Eq. (39) shows the important fact that Reynold's analogy—i.e., the proportionality of heat transfer and skin friction—no longer holds when there is a magnetic

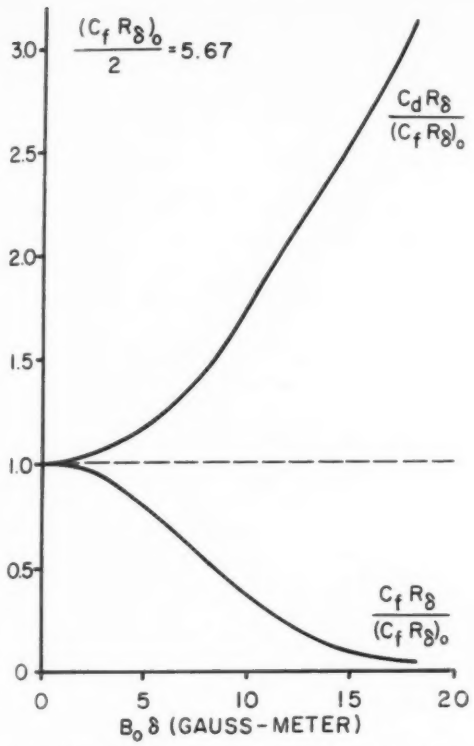

FIG. 5. Magnetic effects on skin friction and total drag for the heat insulated wall, $M_\infty = 30$ ($T_\infty = 300°$K., $p = 10^{-2}$ atm).

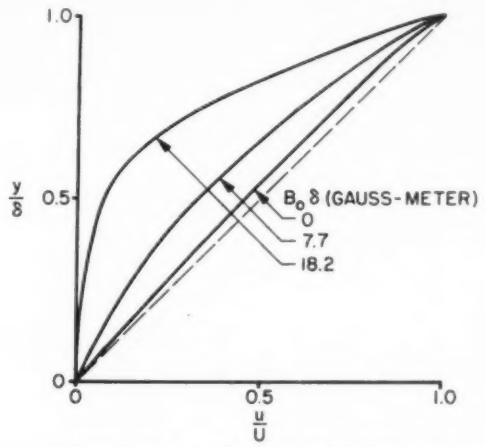

FIG. 6. Magnetic effects on velocity distribution for the heat insulated wall, $M_\infty = 30$ ($T_\infty = 300°$K., $p = 10^{-2}$ atm).

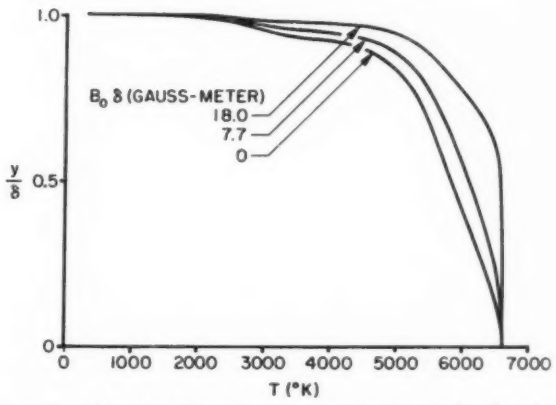

FIG. 7. Magnetic effects on temperature distribution for the heat insulated wall, $M_\infty = 30$ ($T_\infty = 300°$K., $p = 10^{-2}$ atm).

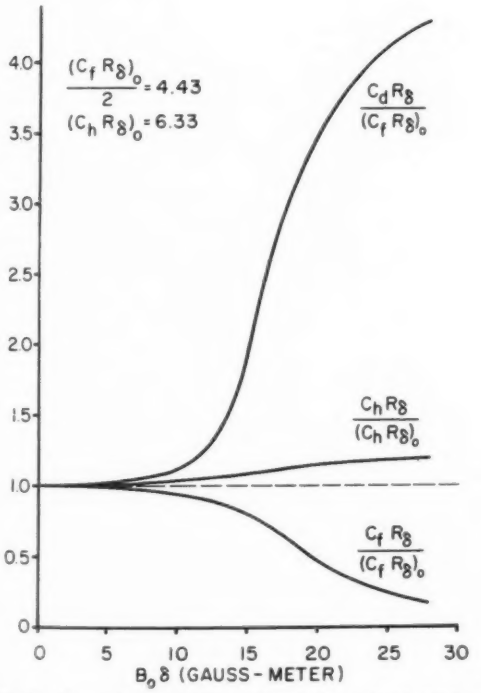

FIG. 8. Magnetic effects on skin friction, total drag, and heat transfer for the heat-transfer case, $M_\infty = 30$ ($T_\infty = 300°$K., $T_w = 1{,}200°$K., $p = 10^{-2}$ atm).

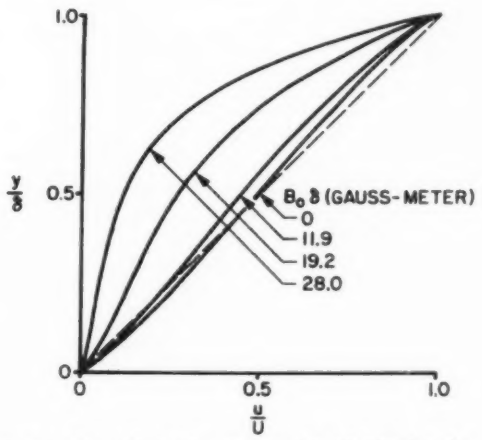

FIG. 9. Magnetic effects on velocity distribution for the heat-transfer case, $M_\infty = 30$ ($T_\infty = 300°$K., $T_w = 1{,}200°$K., $p = 10^{-2}$ atm).

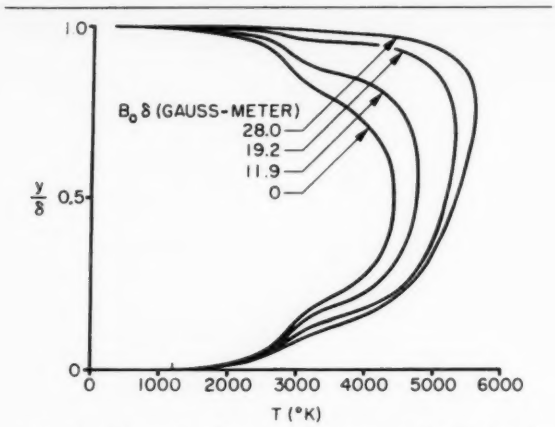

FIG. 10. Magnetic effects on temperature distribution for the heat-transfer case, $M_\infty = 30$ ($T_\infty = 300°$K., $T_w = 1{,}200°$K., $p = 10^{-2}$ atm).

field. Incompressible Couette and boundary-layer flows show the same result.

The induced magnetic field is obtained by integrating Eq. (20). The result is

$$B_x = [B_0 R_M/(C_f R_\delta/2)] \int_{\bar{u}}^{1} (\bar{\eta}\bar{\sigma}\bar{u}\, d\bar{u}/\bar{\tau}) \qquad (42)$$

where $R_M = \mu\sigma_{0max}\delta U$ is a magnetic Reynolds Number. The current density is

$$j\delta = (B_0 R_M/\mu)\, \bar{\sigma}\bar{u} \qquad (43)$$

and, using Eq. (19), the total current is

$$J = \frac{(B_x)_{max}}{\mu} = \frac{B_0 R_M}{\mu(C_f R_\delta/2)} \int_0^1 \frac{\bar{\eta}\bar{\sigma}\bar{u}\, d\bar{u}}{\bar{\tau}} \qquad (44)$$

The procedure for solving these equations numerically will now be considered briefly. A more detailed discussion is given in Appendix (D). The general procedure is to solve Eq. (25), which comes from the momentum equation, and Eq. (32), which comes from the energy equation, simultaneously, using an iteration scheme. The shear stress distribution $\bar{\tau}(\bar{u})$ and the enthalpy distribution $\bar{h}(\bar{u})$ are thus obtained and are then used to calculate all other desired quantities from the equations given in this section. For the case of the heat insulated wall, Eq. (32) reduces to Eq. (32a), and no iteration is needed since $\bar{h}(\bar{u})$ can now be obtained without knowing $\bar{\tau}(\bar{u})$.

CALCULATED RESULTS FOR AIR

Using the data given in Figs. 2, 3, and 4 and the equations of the previous section, calculations have been carried out for the following cases: (1) heat insulated wall for values of the free-stream Mach Number M_∞ from 10 to 30 in steps of 5, and (2) one case of heat transfer ($T_w = 1{,}200°$K.) for $M_\infty = 20$ and 30. Other pertinent values used in the calculations are

$$T_\infty = 300°\text{K.}, \quad p_\infty = 10^{-2}\text{ atm}, \quad \gamma = 1.40, \quad Pr = 0.70$$

The free-stream pressure corresponds roughly to 100,000 ft. altitude.

For convenience in the discussion of the results, it will be assumed that comparisons with and without magnetic field are made for the same value of δ—i.e., $R_\delta = (R_\delta)_0$. Then, skin friction, heat transfer, and total drag can be referred to explicitly, rather than $C_f R_\delta$, etc. The results will, however, always be presented in the more general form with R_δ exhibited. In the m.k.s. system, B has the units (webers/meter^2). However, in the presentation of the results, the more familiar gauss unit is used [1 (weber/meter^2) = 10^4 gauss].

No attempt will be made in this paper to determine what constitutes practical magnetic field strengths from the design point of view. However, for discussion purposes, a rough classification of what will be referred to as moderate or reasonable magnetic field strengths will be given. Magnetic field strengths of the order of 500 gauss or less will be referred to as reasonable since they can be produced with relative ease over a fairly large area without the use of extremely heavy equipment. Note that a steady field strength of 10^4 gauss may be taken as a practical maximum in the laboratory.

Heat Insulated Wall

Although this case is probably not very practical because of the high temperatures at the wall, it is interesting to examine the effects of a magnetic field and to compare the results for this case with the results for the heat-transfer case which will be given later.

Only the results for $M_\infty = 30$ are presented, the results being typical for all the Mach Numbers considered except for the magnetic field strengths required. Results for $M_\infty = 30$ are presented in Figs. 5, 6, and 7. Fig. 5 shows that a tenfold decrease in skin friction and a threefold increase in total drag are obtained with the very reasonable magnetic field strength $B_0 \doteq 17.5$ gauss when $\delta = 1$ meter, and the still reasonable value $B_0 = 175$ gauss when $\delta = 0.1$ meter. It is clear from Fig. 6 and Eq. (26) that the rate of work done τu on a fluid element and the heat flux q out of the element are decreased near the stationary wall and increased near the moving wall by the magnetic field. Fig. 7 shows that the net effect is an increased temperature across the flow field and an increased heat transfer to the moving wall.

The large effects caused by relatively weak magnetic fields can, of course, be traced to the relatively large electrical conductivities associated with the high temperatures. The maximum conductivity for the case presented is about 1,600 mhos/meter. This should be compared with 10^7 mhos/meter for copper and 10^{-} mhos/meter for a good electrical insulator like glass. For $M_\infty = 20$, the maximum conductivity is about 170 mhos/meter and $B_0\delta = 40$ gauss-meter produces the same changes in skin friction and total drag as mentioned above for $M_\infty = 30$. For $M_\infty = 10$ the maximum conductivity is about 0.06 mhos/meter and comparable magnetic effects are obtained for $B_0\delta \doteq 2{,}00$ gauss-meter. According to the rough classification used

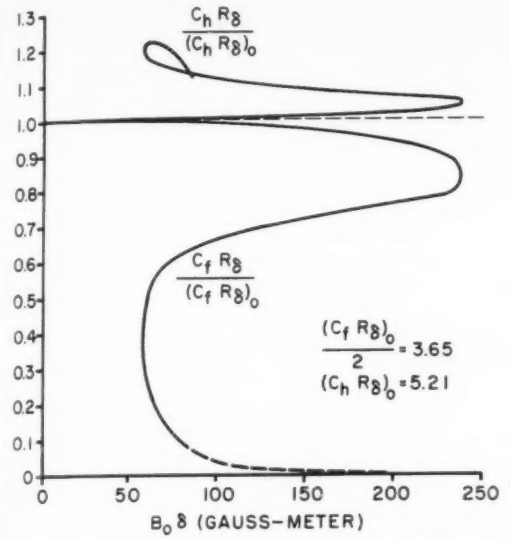

FIG. 11. Magnetic effects on skin friction and heat transfer for the heat-transfer case, $M_\infty = 20$ ($T_\infty = 300°K.$, $T_w = 1{,}200°K.$, $p = 10^{-2}$ atm).

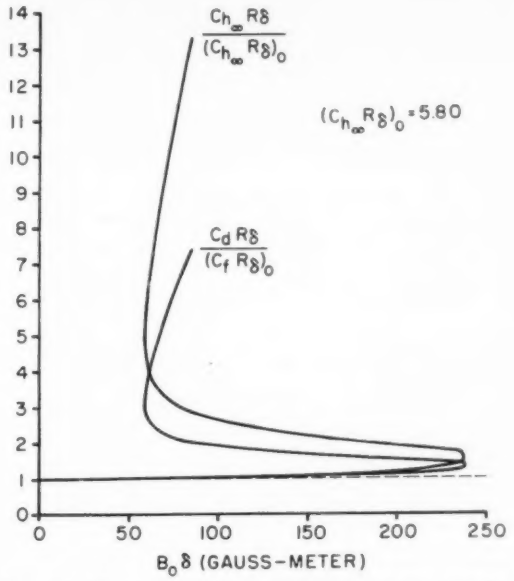

FIG. 12. Magnetic effects on total drag and heat transfer to the moving wall for the heat-transfer case, $M_\infty = 20$ ($T_\infty = 300°K.$, $T_w = 1{,}200°K.$, $p = 12^{-2}$ atm).

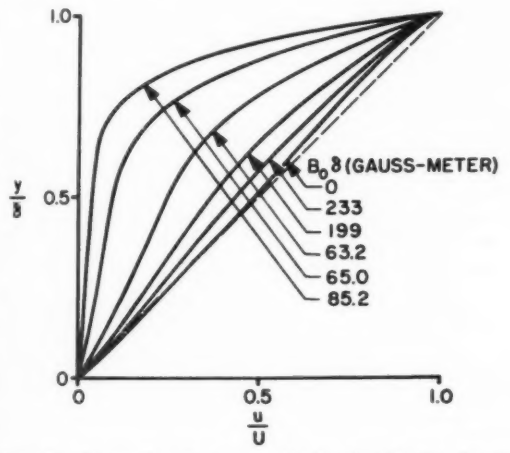

FIG. 13. Magnetic effects on velocity distribution for the heat-transfer case, $M_\infty = 20$ ($T_\infty = 300°K.$, $T_w = 1{,}200°K.$, $p = 10^{-2}$ atm).

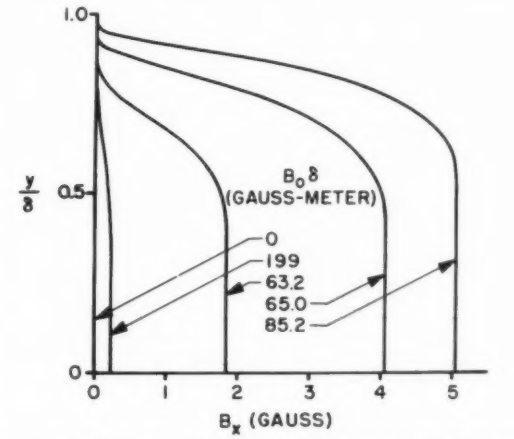

FIG. 15. Magnetic effects on induced magnetic field distribution for the heat-transfer case, $M_\infty = 20$ ($T_\infty = 300°K.$, $T_w = 1{,}200°K.$, $p = 10^{-2}$ atm).

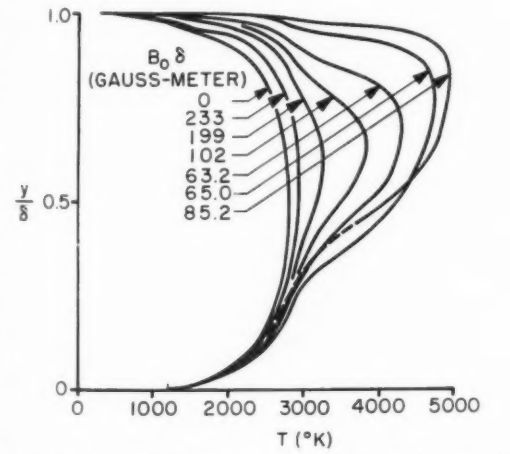

FIG. 14. Magnetic effects on temperature distribution for the heat-transfer case, $M_\infty = 20$ ($T_\infty = 300°K.$, $T_w = 1{,}200°K.$, $p = 10^{-2}$ atm).

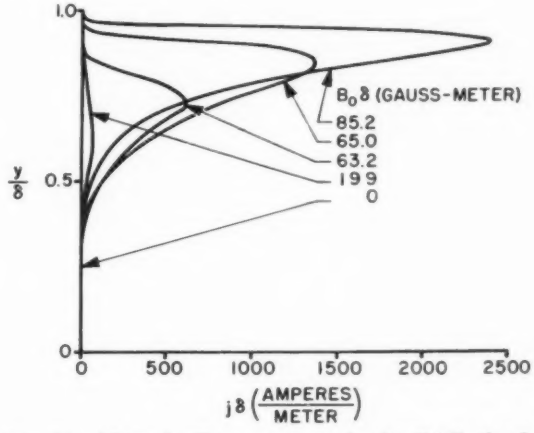

FIG. 16. Magnetic effects on current density distribution for the heat-transfer case, $M_\infty = 20$ ($T_\infty = 300°K.$, $T_w = 1{,}200°K.$, $p = 10^{-2}$ atm).

in this report, the magnetic field strength required for $M_\infty = 10$ is not considered reasonable.

Heat-Transfer Case

Results for $M_\infty = 30$ are presented in Figs. 8, 9, and 10. Fig. 8 shows that, for the reasonable magnetic field corresponding to the value of $B_0\delta = 25$, a 400 per cent increase in total drag is accompanied by only a 20 per cent increase in the heat transfer. Fig. 10 shows the pronounced heating effect of the magnetic field, the maximum temperature being increased from about 4,400°K. for $B_0\delta = 0$ to about 5,600°K. for $B_0\delta = 28$. The small effect of the magnetic field on the wall heat transfer shows that the temperature reduction due to decreased viscous heating near the stationary wall and the temperature increase due to increased heating near the moving wall are about equal near the stationary wall. These changes in viscous heating also explain the shift of the maximum temperature position towards the moving wall.

Results for $M_\infty = 20$ are presented in Figs. 11 through 16.

Consider, for the moment, the skin-friction curve in Fig. 11. The solid curve represents calculations and the dashed curve is drawn in to illustrate the probable continuation of this curve. The peculiar hysteresis character of the result can be traced to the fact that, when there is no magnetic field, enthalpies at all points in the flow field are low enough so that σ varies rapidly with h (see Fig. 4). A simplified problem based on a crude model of this flow that retains the essential σ variation with h has been studied and found to exhibit the same hysteresis property. The reason this behavior is not found for the case $M_\infty = 30$ is that, there, the enthalpies at most points of the flow field are high enough that σ varies relatively slowly with h (see Fig. 4). Furthermore, this behavior does not occur for the insulated wall for any Mach Number because the maximum conductivity is fixed for all values of $B_0\delta$ and this essentially restricts the variation of σ for most points in the flow field. If the skin-friction curve is divided into three branches by the two vertical tangents to the curve, it is clear that the branch contained between these tangents must represent unstable flows. This means that, if $B_0\delta$ is increased from zero, the skin-friction will follow the upper stable branch until the vertical tangent point at 237 gauss-meter is reached. Further increase of $B_0\delta$ will cause the skin friction to drop abruptly to the corresponding value on the lower stable branch. Note that this hysteresis effect makes it possible to obtain large effects with reasonable magnetic field strengths.

In Fig. 11 the short portion of one stable branch of the heat-transfer curve shows the heat transfer decreasing with increasing $B_0\delta$. This may also be seen in Fig. 14, where a portion of one curve has been dashed for clarity. The trend of the heat-transfer curve indicates that it will probably drop below unity for large enough values of $B_0\delta$.

In Fig. 12, C_{h_∞} denotes the heat-transfer coefficient at the moving wall. Except for the temperature boundary conditions, which do not essentially change the problem, it is easily deduced from symmetry that C_f and C_{h_∞} correspond to the skin friction and heat transfer at the stationary wall when the magnetic field is attached to the moving wall—i.e., when the magnetic field is fixed with respect to the free stream. Furthermore, C_f and C_h give the results for the moving wall. Such problems have been considered in reference 1.

Note in Fig. 15 that the induced field B_x will be small compared with the applied field if δ corresponds to reasonable boundary-layer thicknesses of the order of a meter or less. However, the same conclusion cannot be drawn for $M_\infty = 30$.

Boundary-Layer Considerations

In this brief section a few remarks will be made about the expected applicability of these Couette flow results to laminar boundary layers.

One of the primary differences between a boundary layer and Couette flow is its freedom to grow. Boundary-layer thicknesses with and without magnetic field will in general be different. Rossow[1] has shown that the incompressible boundary layer grows when the magnetic field is applied. The present results indicate that one effect of the magnetic field is to increase the temperatures in the boundary layer and thereby further increase its thickness. Estimates of the boundary-layer growth due to the heating effect alone indicate that $R_\delta/(R_\delta)_0$ will always be greater than $C_hR_\delta/(C_hR_\delta)_0$ given by the Couette flow calculations. It is expected, then, that for a boundary layer a magnetic field will actually decrease the heat transfer, the decrease being estimated to be of the order of 15 to 30 per cent. Furthermore, the skin-friction reductions are expected to be greater than indicated for Couette flow and the increases in total drag, while still present, will not be as pronounced as in Couette flow.

It is expected that the hysteresis effect will be present in boundary layers and that the strengths of the magnetic fields to produce the effects will be of the order indicated by the present results.

Discussion of Some Assumptions

One assumption in the calculations is that the pressure is constant throughout the flow field. This assumption can lead to errors in two ways: (1) by changing the values of η and σ and (2) by modifying the heat transfer as shown in Eq. (15).

Consider the first source of error, and note from Figs. 3 and 4 that relatively large changes in pressure would be required to significantly alter η and σ. Using the values of the induced field obtained from the calculations, the maximum magnetic pressures $(B_x)_{max}^2/2\mu$ were compared with the free-stream pressure $p_\infty = 10^{-2}$ atm. In all cases the ratio of the magnetic to free-stream pressure was found to be of the order of

10^{-2} or less and, thus, the changes in pressure are truly negligible. Consider, now, what will happen if p_∞ is reduced, say, to the value of 10^{-4} atm. Because of the relatively small effects on η and σ, the calculated results would be about the same as obtained in this report. Now, the maximum magnetic pressure is of the order of p_∞ for some cases, and reductions in fluid pressure to vacuum near the wall are indicated. For such conditions the analysis of this paper would clearly not apply. From such considerations it is expected that the present analysis cannot be applied for values of p_∞ much below 10^{-3} atm.

Consider now the second source of error. Using the above results for the pressure changes, the ratio of the second term to first term in Eq. (15) was calculated and found to be less than 10^{-2} for all cases. Here, again, reductions in p_∞ will increase the second term (it actually increases both factors) and violate the assumption of constant pressure.

Another assumption that has been used is that σ is a scalar and is independent of the magnetic field strength. For this assumption to hold it is necessary that the Larmor or cyclotron frequency ω_L of the electron be much less than the collision frequency ω_C of the electrons (see, for example, references 11 and 12). For a magnetic field strength of $B = 1$ gauss the Larmor frequency is $\omega_L = 2.8 \times 10^6$ cps and ω_L increases proportionally with B. Based on a collision cross section of 10^{-15} cm.^{2} [see Appendix (A)], the collision frequency for the pressure of 10^{-2} atm. is about 4×10^8 and varies proportionally with the pressure. It is clear that if it is required that $\omega_L/\omega_C \leq 0.1$ then B must be of the order of, or less than, 10 gauss. Field strengths of this magnitude can always be obtained by making δ large enough. Examination of the results shows that for reasonable boundary-layer thicknesses of the order of 1 meter or less the condition $\omega_L \ll \omega_C$ will not be satisfied. If the properties of σ are not drastically changed for $\omega_L \approx \omega_C$ then the present results will be applicable to boundary layers. It should be remarked that when ω_L is not much less than ω_C, σ has a tensor character, the circumferential current will be decreased as compared to the current for a scalar σ, currents other than circumferential will occur, and the conductivity will be a function of the magnetic field strength.

The last assumption to be discussed is that of thermodynamic equilibrium. This means that the reaction times are short compared with the time for an air particle to traverse the length of the body and to diffuse across the boundary layer. The effect of diffusion across the boundary layer will not be considered. If

$$t_{\text{ion.}} \text{ (ionization time)} \gg t_{\text{traverse}} \text{ (traverse time)}$$

then the boundary layer will be essentially an electrical insulator and magnetic fields will have little or no effect. If

$$t_{\text{ion.}} \geq t_{\text{diss.}} \text{ (dissociation time)}$$

then the equilibrium case indicates the maximum possible magnetogasdynamic effects. Note, however, that if $t_{\text{ion.}}$ is much shorter than both $t_{\text{diss.}}$ and t_{traverse} the ionization and conductivity in the boundary layer will be greater than for the case of thermodynamic equilibrium and the magnetic effects would be enhanced. The various possibilities are discussed because little is known of ionization times in air, and the last possibility is at least suggested by Blackman.[13]

Probable Effects of Seeding

The term "seeding" refers to the insertion into the boundary layer of small amounts of some foreign material that ionizes at appreciably lower temperatures than air—e.g., potassium. In this way relatively large electrical conductivities in the boundary layer can be obtained at the lower Mach Numbers.

Clearly, the probable effect of seeding is to shift the magnetogasdynamic effects shown in this paper to lower Mach Numbers and to show larger effects at the Mach Numbers given here.

Concluding Remarks

To illustrate some of the implications of the results obtained here, consider, for purposes of discussion, a body traveling at hypersonic speeds. Let the body be slender enough so that the drag on the body is primarily due to skin friction. Let the average surface temperature of the body be maintained at a value of the order of that used in the heat-transfer case in this discussion—i.e., $T_w = 1{,}200°$K.

The drag must show up as heat produced by viscous dissipation. Part of the heat is found in the body and part is found in the wake of the boundary layer. If the total drag (skin friction) of this body is increased—e.g., by increasing the speed—the heat transfer increases in proportion. The increased dissipation associated with the increased drag shows up again as heat in both the body and the wake.

Now, consider what happens when the magnetic field is turned on. The total drag will increase and the magnetic field acts as a brake. The results show that large total drag increases are obtained with relatively weak magnetic fields. At the same time, large reductions in skin friction occur and the heat transfer is practically unaltered. The total drag is primarily magnetic drag—i.e., the force produced on the body via the magnetic field due to the interaction of the electrically conducting boundary layer with the magnetic field—because of the large reduction in skin friction. Since the heat transfer is unchanged, the heating associated with the increased drag must show up entirely in the boundary-layer wake. Note that the effect of increasing the total drag without increasing the heat transfer can be obtained by attaching a drag producing device (e.g., a parachute) to the rear of the body.

The ratio of the total drag coefficient to the average heat-transfer coefficient is an important parameter in these considerations. For the slender body with no magnetic field this ratio is of the order of unity (Reyn-

olds' analogy) and, from the present results, this ratio is much greater than unity for the magnetic case.

From these considerations, it can be inferred that if the magnetic and nonmagnetic cases are compared on the basis of the same total drag, the heat transfer for the magnetic case will be much less than for the nonmagnetic case.

It is interesting to note that a very blunt body at high speeds is similar to the magnetic case in that the ratio of total drag coefficient to average heat-transfer coefficient is large compared with unity. The drag of the blunt body is primarily pressure drag and the dissipative heating is mainly in the wake of the bow shock wave.

Appendix (A)—Transport Coefficients

Electrical Conductivity, σ

The electrical conductivity of air has been measured by Lamb and Lin.[14] In order to obtain values of conductivity for a wide variety of pressures, σ was calculated using the following simple kinetic theory formula (see, e.g., reference 14):

$$\sigma = (e^2/S\sqrt{m_e kT})\,(N_e/N) \tag{A-1}$$

where

e = charge of an electron
m_e = mass of an electron
k = Boltzmann constant
T = absolute temperature
S = averaged collision cross section for scattering of electrons
N_e = number density of electrons—i.e., number per unit volume
N = number density of particles other than electrons

All numerical constants have been absorbed into the unknown S. S is a weak function of T (see reference 14) but will be taken to be constant in this paper. Examination of the results of reference 14 shows that the value of $S = 10^{-15}$ cm.^{2} will give sufficiently accurate results for our purposes. N_e and N were obtained from tables of the equilibrium composition of air given in references 5 and 7.

Data for N_e has been given for 3,000°K. and up. The calculated values of σ were extrapolated to lower temperatures in a reasonable way on a plot of σ versus T. The dashed portions of the curves in Fig. 4 indicate the extrapolated values, the wiggles in the curves arising from the wiggles in the T versus h curves of Fig. 2.

Viscosity Coefficient, η

Exact calculations of η at high temperatures are not available. To the accuracy of existing knowledge, Greifinger[15] indicates that the Sutherland formula is a reasonable approximation for the range of temperatures of interest here. Dommett[16] shows somewhat poorer agreement with Sutherland's formula. Sutherland's formula is considered to be sufficiently accurate for the present study, and the following form has been used:[17]

$$\eta/\eta_\infty = [(T_\infty + 114)/(T + 114)]\,(T/T_\infty)^{3/2} \tag{A-2}$$

Prandtl Number, Pr

References 15 and 16 and references therein indicate that for the range of temperatures occurring in this paper the Prandtl Number is nearly constant. The Prandtl Number has, therefore, been taken constant here.

Appendix (B)—Incompressible Couette Flow

The results for incompressible Couette flow with the magnetic field fixed to the stationary wall are summarized below.

$$\bar{u} = \sinh(N_H\bar{y})/\sinh N_H \tag{B-1}$$

$$C_f R_\delta/2 = N_H/\sinh N_H \tag{B-2}$$

$$\bar{T}_r = 1 + (Pr\,U^2/2C_pT_\infty) \tag{B-3}$$

$$\bar{T} = \bar{T}_w + (\bar{T}_r - \bar{T}_w)\bar{y} - (Pr\,U^2/2C_pT_\infty)\,[\sinh^2(N_H\bar{y})/\sinh^2 N_H] \tag{B-4}$$

$$C_h R_\delta = 1/Pr \tag{B-5}$$

$$C_d R_\delta/2 = (C_f R_\delta/2)\cosh N_H = N_H \cosh N_H/\sinh N_H \tag{B-6}$$

$$B_x/B_0R_M = [\cosh N_H - \cosh(N_H\bar{y})] \div N_H \sinh N_H \tag{B-7}$$

$$j\delta = (B_0R_M/\mu)\,[\sinh(N_H\bar{y})/\sinh N_H] \tag{B-8}$$

These results exhibit most of the qualitative features of the incompressible boundary-layer problem solved by Rossow.[1] Note here that the recovery temperature is independent of the magnetic field. Eq. (B-5) shows that the heat transfer is also independent of the magnetic field for fixed R_δ. If Rossow's result for the growth of the boundary layer is used, it is found that a reduction in heat transfer, approximately equal to that given by Rossow, occurs.

Rossow also studied the effects of a magnetic field attached to the free stream. The Couette flow results for this case again show qualitative agreement with Rossow's results. The Couette flow results for a magnetic field attached to the moving wall are summarized below.

$$\bar{u} = 1 - \{\sinh[N_H(1 - \bar{y})]/\sinh N_H\} \tag{B-9}$$

$$C_f R_\delta/2 = N_H \cosh N_H/\sinh N_H \tag{B-10}$$

$$\bar{T}_r = 1 + (Pr\,U^2/C_pT_\infty) \times [(N_H \cosh N_H/\sinh N_H) - (1/2)] \tag{B-11}$$

$$\bar{T} = 1 + [\bar{T}_w - 1 + (Pr\,U^2/2C_pT_\infty)]\,(1 - \bar{y}) - (Pr\,U^2/2C_pT_\infty)\{\sinh^2[N_H(1 - \bar{y})]/\sinh^2 N_H\} \tag{B-12}$$

$$C_h R_\delta = 1/Pr \tag{B-13}$$

The heat transfer is not independent of the magnetic field for fixed R_δ since the recovery temperature is not independent of the magnetic field.

Appendix (C)—Maximum Enthalpy for Zero Magnetic Field

This result is easily obtained in an obvious way from Eq. (32) with $\bar{\tau} = 1$. The result is

$$\bar{h}_{0max} = \bar{h}_w + [2(\gamma - 1)PrM_\infty{}^2]^{-1} \times \{[(\gamma - 1)/2]PrM_\infty{}^2 + 1 - \bar{h}_w\}^2$$

Appendix (D)—Numerical Procedure for Solving Equations

Consider the simple case of the heat insulated wall. For given boundary conditions, $\bar{h}(\bar{u})$ is given by Eq. (32a). $\bar{\eta}(\bar{u})$ and $\bar{v}(\bar{u})$ are then obtained from Figs. 3 and 4 and the integration in Eq. (25) can be carried out. For a given value of $2N_H/C_fR_\delta$, $\bar{\tau}(\bar{u})$ is given by Eq. (25). $C_fR_\delta/2$ can then be obtained using Eq. (33), and N_H and, thus, $B_0\delta$, are finally obtained. The fact that $B_0\delta$ is obtained from the calculations explains the odd values shown in the Figures.

Consider now the general case with heat transfer. To start the iteration, assume $\bar{\tau}(\bar{u})$ (e.g., the distribution for zero magnetic field, $\bar{\tau}(\bar{u}) = 1$, might be used). Then, using $\bar{h}(\bar{u})$ obtained from Eq. (32), $\bar{\eta}(\bar{u})$ and $\bar{v}(\bar{u})$ are obtained from Figs. 3 and 4 and the integration in Eq. (25) is carried out. Assuming a value for $2N_H/C_fR_\delta$, a new $\bar{\tau}(\bar{u})$ is obtained from Eq. (25) and is substituted back into Eq. (32). The iteration is repeated until two successive distributions $\bar{\tau}(\bar{u})$ agree to within the desired accuracy. It was found that if $2N_H/C_fR_\delta$ was held constant throughout a series of iterations, the iteration scheme did not converge. However, if $2N_H/C_fR_\delta$ was modified at each iteration so that the value of $\bar{\tau}$ for some fixed value of $\bar{u}$ was held constant, the iteration scheme converged rapidly, never requiring more than three iterations. $B_0\delta$ is obtained from the resulting value of $2N_H/C_fR_\delta$ after $C_fR_\delta/2$ is calculated using Eq. (33).

References

[1] Rossow, Vernon J., *On Flow of Electrically Conducting Fluids Over a Flat Plate in the Presence of a Transverse Magnetic Field*, NACA TN 3971, May, 1957.

[2] Illingworth, C. R., *Some Solutions of the Equations of Flow of a Viscous Compressible Fluid*, Cambridge Philosophical Society Proceedings, Vol. 46, pp. 469–478, 1950.

[3] Liepmann, H. W., and Bleviss, Z. O., *The Effects of Dissociation and Ionization on Compressible Couette Flow*, Douglas Aircraft Company, Inc., Report No. SM-19831, May, 1956.

[4] Liepmann, H. W., and Roshko, A., *Elements of Gasdynamics*, John Wiley and Sons, Inc., New York, 1957.

[5] Gilmore, F. R., *Equilibrium Composition and Thermodynamic Properties of Air to 24,000°K.*, Project Rand, RM-1543, August 24, 1955.

[6] Hilsenrath, J., and Beckett, C. W., *Tables of Thermodynamic Properties of Argon-Free Air to 15,000°K.*, MIPR-AEDC-1, Arnold Engineering Development Center, AEDC-TN-56-12, September, 1956.

[7] Treanor, C. E., and Logan, J. G., Jr., *Tables of Thermodynamic Properties of Air from 3,000°K. to 10,000°K.*, Cornell Aeronautical Laboratory, Report No. AD-1052-A-2, Tech. Note No. AFOSR-TN-56-343, June, 1956.

[8] Feldman, Saul, *Hypersonic Gas Dynamics Charts for Equilibrium Air*, AVCO Research Laboratory, January, 1957.

[9] Korobkin, I., and Hastings, S. M., *Mollier Chart for Air in Dissociated Equilibrium at Temperatures of 2,000°K. to 15,000°K.*, NAVORD Report 4446, May 23, 1957.

[10] Broadwell, James E., *A Simple Model of the Nonequilibrium Dissociation of a Gas in Couette and Boundary Layer Flow*, Douglas Aircraft Company, Inc., Report No. SM-22888, August, 1957.

[11] Cowling, T. G., *Magnetohydrodynamics*, Interscience Publishers, Inc., New York, 1957.

[12] Spitzer, Lyman, Jr., *Physics of Fully Ionized Gases*, Interscience Publishers, Inc., New York, 1956.

[13] Blackman, V. H., *Experiments Using a Hydromagnetic Shock Tube*, Paper presented at the Second Magnetohydrodynamics Symposium, Lockheed Research Laboratory, Palo Alto, California, December 16, 1957.

[14] Lamb, Lawrence, and Lin, Shao-Chi, *Electrical Conductivity of Thermally Ionized Air Produced in a Shock Tube*, Journal of Applied Physics, Vol. 28, No. 7, pp. 754–759, July, 1957.

[15] Greifinger, P. S., *Transport Coefficients of Dissociating and Slightly Ionizing Air*, Rand RM-1794, April, 1957.

[16] Dommett, R. L., *Thermodynamic Properties of Air at High Temperatures*, Royal Aircraft Establishment, Technical Note No. G.W. 429, August, 1956.

[17] Howarth, L., (Ed.), "Modern Developments in Fluid Dynamics: High Speed Flow," Young, A. D., *Boundary Layers*, Vol. I, p. 388, Oxford University Press, 1953.

[18] Sommerfeld, A., *Electrodynamics*, p. 25, Academic Press, Inc., New York, 1952.

An Authorized Binding for
Journal of the Aero/Space Sciences

Arrangements have been made by the Institute of the Aeronautical Sciences for members and subscribers to have their Journals bound carefully and economically. Simply write for details to:

Publishers' Authorized Bindery Service

5809 West Division St. Chicago 51, Ill.

The Transonic Flow Field of an Axial Compressor Blade Row†

JAMES E. McCUNE*
Cornell University

SUMMARY

The general three-dimensional theory for compressible flow through axial compressor blade rows[1, 2] is applied to transonic cases. Because of the occurrence in the transonic range of acoustic resonance, the theory is modified to include first-order viscous and heat-conduction effects. This approach is adequate to bring most transonic compressor problems within the realm of linear treatment.

Numerical examples of the behavior of a transonic blade row are presented and discussed. The results indicate a smooth transition from the subsonic to the transonic, or mixed-flow, regimes—i.e., the degeneracy encountered in two-dimensional transonic applications of the small-perturbation theory is completely absent. At the same time, the results emphasize the failure of any strip theory, or "blade-element," approximation in the transonic range and thereby cast serious doubt upon the usefulness of transonic cascade studies.

SYMBOLS

a	= speed of sound
A	= $B^{2/3}(1 - h)$ = similarity parameter
B	= number of blades in blade row
$c(r)$	= local blade chord
$c_{ax}(r)$	= axial projection of local blade chord
c_v	= specific heat at constant volume, undisturbed fluid
c_p	= specific heat at constant pressure, undisturbed fluid
C_p	= $(p - p_\infty)/(1/2)\rho_\infty U^2$
C_d	= section drag coefficient
C_{DW}	= total wave-drag coefficient per blade
C_Q	= total torque coefficient per blade
C_k	= coefficients for determining K_{nk}
$g(x)$	= profile shape function
h	= r_H/r_T = hub ratio
k	= thermal conductivity
L	= $2\pi r_T/B$ = blade spacing
M_{ax}	= axial Mach Number
M_T	= resultant Mach Number at tips
$M_T^{(m-k)}$	= resultant tip Mach Number for resonance of mode
m, k	= summation indexes
n	= mB
p	= static pressure
p_∞	= static pressure of undisturbed fluid
Pr	= Prandtl Number
$\boldsymbol{q}(x, r, \theta)$	= perturbation velocity vector = (u, v_r, v_θ)
$Q_{mB-k}(x)$	= Fourier expansion coefficients for radial thickness distribution
r_T	= radius of tips = radius of shroud
r_H	= radius of hub
r_S	= radius of sonic cylinder
R	= gas constant = $c_p - c_v$
Re	= Reynolds Number = Ur_T/ν
t	= t_1 = time
T	= temperature
T_∞	= temperature of undisturbed fluid
U	= axial speed
Δv_n	= discontinuity in velocity normal to mean (helical) surface of blades
(x_1, r_1, θ_1)	= space-fixed cylindrical coordinates
(x, r, θ)	= rotor-fixed cylindrical coordinates
β	= $(1 - M_{ax}^2)^{1/2}$
γ	= ratio of specific heats, c_p/c_v
ϵ	= dimensionless acoustic diffusivity, Eq. (14)
μ, μ'	= shear and bulk viscosities, undisturbed fluid
ν	= kinematic viscosity, undisturbed fluid
ρ	= density
ρ_∞	= density of undisturbed fluid
σ	= $\omega r/U$ = dimensionless radius
σ_T	= $\omega r_T/U$ = dimensionless tip radius
σ_S	= $\omega r_S/U = \beta/M_{ax}$ = dimensionless radius of sonic cylinder
$\tau(r)$	= local thickness to chord ratio
τ_0	= thickness to chord ratio at hub
$\phi(x_1, r_1, \theta_1, t_1)$	= perturbation velocity potential, space-fixed system
$\varphi(x, r, \theta)$	= perturbation velocity potential, rotor-fixed system
ω	= angular velocity of blade row, rad. per unit time

Presented at the Propulsion Aerodynamics Session, Twenty-Sixth Annual Meeting, IAS, New York, January 27–30, 1958. Revised and received April 7, 1958.

† This paper is the second in a series of two articles and is derived from a portion of the author's Ph.D. thesis at Cornell University.[2] This research has been supported in part by the Office of Scientific Research of the United States Air Force. The author wishes to express his gratitude for the guidance and encouragement of Dr. William R. Sears and Dr. Nicholas Rott during the performance of this study.

* Now, Research Associate. Formerly, National Science Foundation Fellow.

INTRODUCTION

INTEREST in the transonic compressor derives from the experimentally observed fact that relatively efficient operation of axial compressors can be obtained throughout the transonic regime, and from the circumstance that maximum thrust for a given jet engine requires maximum mass flow through the engine, which in turn implies transonic Mach Numbers at the diffuser exit. Consequently, the transonic compressor blade row, with a subsonic resultant Mach Number at the hub and a near-sonic or supersonic resultant Mach Number at the tips (see Fig. 1), is of considerable interest to the designer.

The transonic blade row, thus defined, has not previously yielded to systematic investigation. The usual approximation, which assumes a two-dimensional flow field in each elemental compressor annulus, is no longer applicable because of the complicated, three-dimensional nature of the interference pattern between

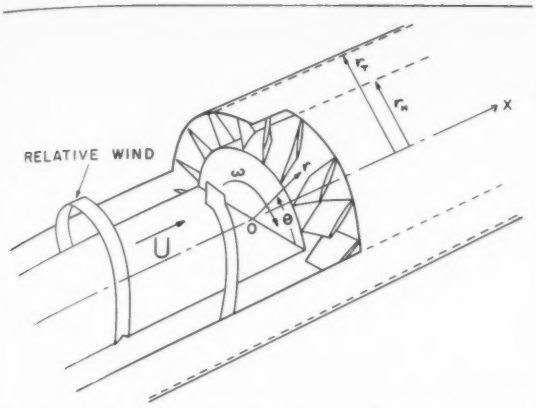

FIG. 1. Blade row geometry and notation, showing cylindrical coordinates fixed in rotor. Helical arrow indicates incoming flow viewed from rotor.

blades and because of the strong influence on one another of different radial elements of the same blade. Furthermore, no theory that is linear in the usual sense of acoustics—i.e., linearized by assuming small disturbances—exists for steady, two-dimensional transonic flows. As a result, a whole region of the flow field cannot be treated at all by a first-order two-dimensional approximation.

Yet compressors do run in the transonic regime, and in fact do so with quite acceptable efficiencies. Designers of these machines, in the absence of a satisfactory theory to guide them, having relied upon experiment, using cascade tests in many cases. In the transonic regime, however, the results of such experiments are difficult to interpret, not only because of the theoretical difficulties described above, but because of the impossibility of setting up experimentally a truly periodic transonic flow in two dimensions. Application of the cascade experiment to actual blade rows in the transonic case, therefore, is open to serious doubt; the results of the present investigation tend to emphasize this fact.

The General Method

The linearized (acoustic) theory contains the approximation that disturbances propagate relative to the undisturbed fluid at a sound speed appropriate to the undisturbed condition. Consequently, if this theory is applied to sources and sinks moving exactly at the unperturbed sound speed, disturbances will, according to the theory, accumulate. The accumulation is particularly severe in steady two-dimensional cases because of the reinforcement of each source by its identical neighbors, and in these cases the theory cannot be applied. In two-dimensional steady flow, the accumulation may be relieved by going to higher order theories that take into account, for example, propagation at the local speed of sound relative to local fluid velocities.

There are important physical cases, however, in which relief of the accumulation occurs even within the acoustic approximation. Examples that are well known include unsteady two-dimensional transonic flows as well as the familiar wing-sweepback effect in steady three-dimensional flows. The present study of rotating machinery in transonic operation will provide a further example of three-dimensional relief. Although one source (or radial element of a blade) may be operating at a resultant Mach Number of unity, its immediate neighbors are not, and their disturbances will not reinforce those of the sonic source. Because of this, no degeneracy of the acoustic theory occurs and a first-order flow pattern in the usual sense exists.

For these reasons, the method adopted by the author[1] has been to abandon the two-dimensional approximation at the outset and to study, to first order in small disturbances, the complete three-dimensional flow pattern of an axial compressor blade row of arbitrary geometry. This general approach, and its application to nonlifting subsonic and supersonic blade rows, was the subject of an earlier paper.[2] In that paper, and in reference 1, the way in which the two-dimensional theory can be extracted rigorously from the three-dimensional was investigated. It was found that so long as the resultant tip Mach Number is not too close to unity (it may be either subsonic or supersonic), the classical two-dimensional cascade theories can be obtained by taking the limit as the blade number and the tip radius simultaneously approach infinity while the hub ratio approaches unity. Relaxation of this limit leads to three-dimensional corrections to the usual strip-theory approximation.

As one must expect, when the resultant tip Mach Number approaches unity, the above limiting process is no longer possible, and the first-order flow field is inherently three-dimensional. Consequently, one must make use of the complete three-dimensional formulas to obtain, for example, the first-order pressure distribution and wave energy losses of a transonic blade row. Moreover, the occurrence of acoustic resonance when the tip Mach Number exceeds one must be taken into account and is handled within the present theory by including the effects of viscous damping in the field.

Since the number of blades is large, and this number determines the order of the Bessel functions that occur in the general solution, advantage can be taken of the asymptotic formulas for cylinder functions of large order.[1–4] As a matter of fact, it is this procedure that makes possible the extraction of the strip theory—i.e., two-dimensional theory in each flow annulus with the radius as a parameter—from the general three-dimensional theory in subsonic and supersonic cases.[2]

The Three-Dimensional Solution

Assuming small-perturbations and inviscid potential flow outside of thin boundary layers, one can construct the general three-dimensional solution for flow through axial compressor blade rows by superposition of cylindrical wave functions [see Eqs. (13) and (15) of refer-

ence 2]. Basic to this analysis is the familiar acoustic wave equation.

The general solutions obtained in this way are applicable to blade rows of arbitrary geometry (within limits consistent with the assumption of small perturbations) over a wide range of Mach Numbers. They are degenerate, of course, if the *axial* Mach Number approaches unity, but no such degeneracy occurs if the *relative* Mach Number anywhere in the flow annulus becomes unity.

We are interested here only in the latter case, for which the sonic cylinder—i.e., that cylinder on which the undisturbed relative Mach Number is unity—is within or near the flow annulus. This can occur only when the axial Mach Number is subsonic, and then Eq. (13) of reference 2 applies—viz., for nonlifting blade rows,

$$\varphi(r,\theta,x) = -\frac{B}{2\pi\beta^2}\int_0^{[c(r)/\sqrt{\sigma^2+1}]_{max}} \sum_{m=1}^{\infty}\sum_{k=1}^{\infty} \frac{Q_{mB-k}(\xi)}{\lambda_{mB-k}} R_{mB}\left(K_{mB-k}\frac{r}{r_T}\right) \exp\left\{imB\left(\theta - \frac{\omega\xi}{U}\right) + \frac{imB}{\sigma_S{}^2}\frac{\omega}{U}(x-\xi) - \lambda_{mB-k}\frac{\omega}{U}|x-\xi|\right\} d\xi - \frac{B}{4\pi\beta^2}\int_0^{[c(r)/\sqrt{\sigma^2+1}]_{max}} \frac{Q_{0k}(\xi)}{\lambda_{0k}} R_0\left(K_{0k}\frac{r}{r_T}\right)\exp\left\{-\lambda_{0k}\frac{\omega}{U}|x-\xi|\right\} d\xi \quad (1)$$

where $c(r)$ is the local blade chord and $\sigma = \omega r/U$.

It will be seen that the contribution of each particular solution (or mode) of the wave equation to this general solution is proportional to $Q_{mB-k}(x)/\lambda_{mB-k}$. The coefficients $Q_{mB-k}(x)$ depend only on the blade geometry,[2] whereas the quantities λ_{mB-k} are of the form

$$\lambda_{mB-k} = (mB/\beta\sigma_T) \times \sqrt{(K_{mB-k}{}^2/m^2B^2) - (\sigma_T{}^2/\sigma_S{}^2)} \quad (2)$$

The eigenvalues K_{mB-k} are the solutions of the transcendental equations

$$R'_{mB}(hK_{mB-k}) = R'_{mB}(K_{mB-k}) = 0 \quad (3)$$

which guarantee vanishing radial velocities at the hub and at the shroud. The functions $R_{mB}(z)$ are normalized linear combinations of Bessel and Neumann functions occurring in each particular solution and are defined in reference 2.

Because the number of blades in an axial compressor blade row is generally large, we find ourselves seeking solutions to Eqs. (3) in terms of cylinder functions of very large order. In that case, advantage can be taken of the asymptotic formulas developed by Watson[3] or Olver,[4] and this procedure leads to numerical techniques that can be greatly simplified through the use of a correlating parameter involving the hub ratio and number of blades.[1, 2] In fact, when n is large, the eigenvalues K_{nk} can be written

$$K_{nk}{}^2/n^2 = 1 + (2C_k/n^{2/3}); \quad (n = mB)$$

and in the limit of very large n the coefficients C_k become functions of $Am^{2/3}$ alone, where

$$A = B^{2/3}(1-h)$$

Examples of the coefficients $C_k(A)$ are provided in Fig. 3 of reference 2.

Resonance

A very important feature of the general solution (1) is that under certain conditions one or more of the λ_{mB-k} can vanish. This occurrence is a kind of acoustic resonance and requires special consideration. In fact, it is a phenomenon peculiar to transonic operation, and, therefore, the applicability of the present theory to the transonic regime depends upon our success in treating resonant modes.

The phenomenon of transonic resonance was noticed by Davidson[5] but was not treated in his paper. That it occurs only in the transonic (mixed-flow) regime follows from the fact that if $\lambda_{nk} = 0$

$$\sigma_T/\sigma_S = K_{nk}/n \qquad (n = mB) \quad (4)$$

It can be shown[3] that $K_{nk} > n$ for $n > 0$, and, consequently, resonance appears only when the radius of the sonic cylinder is less than that of the shroud (and is really important only when it is actually within the flow annulus).

Modification of the Theory

Resonant modes have the property of remaining unchanged in form upstream and downstream of the matching plane. Once excited, they require no energy addition to sustain themselves. Since the compressor blading nevertheless puts energy into these modes, no finite steady-state amplitude is possible in the absence of a method for draining energy away from them. If, however, a realistic mechanism, such as viscosity, for extracting wave energy from the system is included within the analysis, a finite amplitude can be established.

Viscous Damping

The original assumptions that led to Eq. (1) do not exclude the possibility of taking into account the first-order effects of viscous damping and heat conduction in the field. External to thin boundary layers, a potential solution still has meaning since no mechanism for producing first-order vorticity is present except shear at solid boundaries. Hence, we may put

$$\boldsymbol{q} = \nabla\phi(x_1, r_1, \theta_1, t_1)$$

to first order, even though we include small but finite viscous damping in the theory.

In analogy with the treatment of one-dimensional sound wave damping given by Stokes and improved by Kirchhoff,[6] we may begin by linearizing the Navier-

Stokes and energy equations to obtain

$$\partial \boldsymbol{q}/\partial t_1 = -(1/\rho_\infty)\nabla_1 p + \{[(4/3)\mu + \mu']/\rho_\infty\} \times \operatorname{grad}_1 \operatorname{div}_1 \boldsymbol{q} - \nu \operatorname{curl}_1{}^2 \boldsymbol{q} \quad (5)$$

$$(1/p_\infty)(\partial p/\partial t_1) - (\gamma/\rho_\infty)(\partial \rho/\partial t_1) = (k/c_v)(\nabla_1{}^2 T/\rho_\infty T_\infty) \quad (6)$$

where μ, μ', c_v, k, γ, p_∞, T_∞, and ρ_∞ all refer to the undisturbed fluid. μ' is the bulk viscosity (assumed zero for monatomic gases) and is included because of its importance in the damping of sound waves[7] when rotational degrees of freedom are present.

Eq. (6) simply states that to first order a fluid particle can gain or lose thermal energy only through heat conduction. The treatment given by Stokes neglects heat conduction and in effect assumes the Prandtl Number $\equiv \mu c_p/k$ to be infinite. Kirchhoff took heat conduction into account in his analysis.[6]

Eqs. (5) and (6) can be reduced in conjunction with the linearized continuity equation

$$(\partial \rho/\partial t_1) + \rho_\infty \operatorname{div}_1 \boldsymbol{q} \quad (7)$$

and the equation of state

$$p = \rho R T \quad (8)$$

to give a modified acoustic wave equation for the perturbation potential in the form

$$\nabla_1{}^2\phi = (1/a^2)\phi_{t_1 t_1} - \{(4/3) + (\mu'/\mu) + [(\gamma - 1)/Pr]\}(\nu/a^2)(\partial/\partial t_1)\nabla_1{}^2\phi \quad (9)$$

where $a^2 \equiv \gamma(p_\infty/\rho_\infty)$. In the derivation of Eq. (9), terms of order ν^2 have been neglected in addition to second-order terms in any disturbance quantities.* Eqs. (5) through (9) are all referred to a space-fixed coordinate system.

The corresponding pressure formula can be written in the form

$$p' = p - p_\infty = -\rho_\infty \phi_{t_1} + [(4/3)\mu + \mu']\nabla_1{}^2\phi \quad (10)$$

in which the usual acoustic formula can be recognized when $\mu = \mu' = 0$.

Consistency

It would be well to pause here to consider the consistency of the present approach in neglecting higher-order inertia terms [for example, the $\boldsymbol{q}\cdot\nabla\boldsymbol{q}$ term in Eq. (5)] while keeping first-order viscous terms proportional to ν. Simple dimensional analysis shows these terms to be in the ratio of a Reynolds Number based on the perturbation velocity and the appropriate wave length of the problem (in this case, L/m for the mth mode, where L is the spacing of the blades).

However, the question of consistency actually requires deeper analysis than the simple process, implied above, of taking ratios, since the terms in question have opposite cumulative effects on the fluid motion. It is well known that the higher order inertia terms in the equations of motion represent "steepening" terms that tend to create shock waves as a given plane disturbance propagates away from its source. Sooner or later these terms would always cause the violation of the assumption of small-perturbations in plane flow if it were not for the operation of viscous damping in preventing the steepening.

The acoustic (first-order) theory is generally considered adequate, therefore, for any small disturbance that damps out in a distance short compared with the distance required for steepening of the wave into a shock. The question of consistency, then, becomes one of deciding which mechanism—that of steepening or that of damping—first becomes predominant.

In the case of one-dimensional sound waves, both the damping distance and the steepening distance can be calculated. It turns out that the acoustic theory is more applicable to high-frequency disturbances than to low-frequency ones, so long as lagging internal degrees of freedom other than rotation are not too important.[7]

In the present case of cylindrical geometry there is evidence that the wave forms, particularly in the case of resonant modes, will not steepen at all. Maslen and Moore[8] considered waves in an infinite cylindrical tube and showed that if second-order terms are included in the calculations the resulting strong waves do not steepen into shock waves as would be expected in other geometries. For this reason the author is encouraged to believe that the inclusion of viscous mechanisms within the linear theory is, in this case, justified.

The above arguments pertain only to the consistency of including viscous terms in a first-order calculation. This is not to say that higher order terms, viscous or inertial, might not become important; indeed, we shall see later that certain isolated nonlinear effects will become significant in some practical cases.

The Solution in the Presence of Viscosity

In coordinates that advance (at a speed U) and rotate (at a speed ω, see Fig. 1) with the blade row, the flow is steady, and in these coordinates (r, θ, x) particular solutions of Eq. (9) can be obtained in the form, with $\varphi(r, \theta, x) = \phi(r_1, \theta_1, x_1, t_1)$,

$$\varphi_{nk} = A_{nk} \exp\{in\theta + (\omega/U) \times [(inM_{ax}{}^2/\beta^2) \pm \lambda_{nk}']x\} R_n[K_{nk}(r/r_T)] \quad (11)$$

where the $R_n(z)$ are the cylinder functions defined in reference 2, satisfying Eqs. (3).

The solutions (11) are identical with the solutions of the ordinary wave equation[2] that were used to build up the general solution (1), with the exception that the quantities λ_{nk} are replaced by

$$\lambda_{nk}' = \sqrt{\lambda_{nk}{}^2 - in\epsilon\{(n^2/\sigma_S{}^2)[(8/\sigma_S{}^4) + (11/\sigma_S{}^2) + 3] - (K_{nk}{}^2/\sigma_T{}^2)[(9/\sigma_S{}^2\beta^2) + (1/\sigma_S{}^2) + (3/\beta^2) + 1]\}}, \quad (n > 0) \quad (12)$$

* For a rather complete account of this procedure, particularly as it applies to plane sound waves, see Lighthill.[7]

$$\lambda_{0k}' = (K_{0k}/\sigma_T\beta) + (\epsilon/2)\,[1 - (K_{0k}^2/\sigma_T\beta^2)] \quad (13)$$

where

$$\epsilon \equiv \{(4/3) + (\mu'/\mu) + [(\gamma - 1)/Pr]\}\,(\sigma_T/\sigma_S^2)\,(1/Re); \quad Re \equiv Ur_T/\nu \quad (14)$$

Eqs. (12) and (13) hold, provided terms of order ϵ^2 are neglected. Moreover, because of the linearity of Eq. (9), the general solution can again be obtained by appropriate superposition of the particular solutions, and the result is simply given by Eq. (1) with λ_{nk} everywhere replaced by λ_{nk}' for $n = mB \geqslant 0$.

Typical values of ϵ for turbomachinery in general use are on the order of 10^{-5} to 10^{-7}, and, in all such cases, the difference between λ_{0k} and λ_{0k}', as well as the viscous term in Eq. (10), can be neglected entirely. However, in transonic operation, when it is possible for one or more of the functions λ_{nk} to vanish for $n > 0$, the importance of the correction terms in Eq. (12) is clear; the viscous terms in fact establish the steady-state amplitude of the resonant modes. Indeed, exactly at resonance we have

$$\lambda'_{mB-k} = e^{\pi i/4}\,(m^{3/2}\epsilon^{1/2}/\sigma_S\beta^2)B^{3/2} \quad (15)$$

This result is in analogy with the result obtained by Stokes for the damping rate of one-dimensional acoustic waves. We note that the amplitude of resonant modes decreases with the 3/2 power of the blade number, and we may conclude from this that the present analysis is meaningful primarily for configurations having a large number of blades.

Even when the number of blades is large, however, exact resonance ($\lambda_{nk} \equiv 0$) of, say, the fundamental mode $m = 1$, $k = 1$ may imply sufficiently large disturbance magnitudes for nonlinear effects to become important. This problem remains to be investigated, but the analysis of reference 8 suggests that a successful method of iteration to obtain higher order terms associated with a given resonant mode could be developed. Even so, this would still leave the problem of treating the possibly important coupling between the resonant mode and the nonresonant ones.

Pressure Coefficients and Forces on the Blades

The limitation of the present solution [Eq. (1)] to the nonlifting, or thickness, problem actually implies that the blades of the rotor (or turbine wheel) are what Busemann has called "limp bodies." That is, the mean camber line of each blade adjusts itself to the local interference pattern induced by its neighbors in such a way that there is no lift. A useful compressor blade row, of course, provides lift, but through the linearization of the problem, the lifting and thickness problems can be studied separately. It is felt that because of the appearance in the transonic regime of wave drag associated with thickness, the thickness problem is not only of interest in itself, but also provides an indication of events in the more general case.

As pointed out by Rott,[9] no wave-energy loss (and hence no wave drag) can occur until the resultant tip Mach Number is greater than unity. Once $\sigma_T/\sigma_S > 1$, however, some of the functions λ_{nk} will be imaginary, and a net loss of wave energy by acoustic radiation will occur. In that case there will appear a drag on the blades associated entirely with the structural thickness provided. It is one of the purposes of the present theory to compute this drag force and the resulting torque that must be supplied to turn the blade row.

If we define the pressure coefficient

$$C_p(r, \theta, x) \equiv p'/(1/2)\rho_\infty U^2 = -[2(u + \sigma v_\theta)/U] \quad (16)$$

we may calculate the section drag coefficient per blade from the formula

$$C_d(r) \equiv D(r)/(1/2)\rho_\infty U^2 c_{ax}(r) = \int_0^1 C_p(r, \omega x/U, x)\,[\Delta v_n(r, x)/U]\,d(x/c_{ax}) \quad (17)$$

where $c_{ax}(r)$ is the axial projection of the local chord, and $\theta = \omega x/U$ defines the zeroth blade surface. The total wave drag and total torque coefficients can be obtained by appropriate integration of $C_d(r)$ over the span.[1]

Numerical Examples*

Specification of the Geometry

The theory described above has been used to compute numerical examples of the pressure distribution over the blades of a nonlifting axial compressor blade row operating in the transonic regime. A blade row containing 64 blades and having a hub ratio of 0.9 was assumed. (The parameter A defined earlier is then equal to 1.6.)

In order to simplify the computation of the coefficients $Q_{mB-k}(x)$, the axial projection of the chord, c_{ax}, was taken to be constant over the span of each blade, and the blade profiles at each radial station were assumed to be similar.

These assumptions lead to the relation, consistent with the present linear theory,

$$\Delta v_n(r, x) = g(x)\tau(r) \quad (18)$$

where $\tau(r)$ is the local thickness to chord ratio, and $\tau g(x)/2U$ is the rate of change with *axial* position of the half-thickness about the mean (chordwise) camber line. (It is merely a matter of convenience to write the specification of the profile shape in terms of the axial position instead of the position measured along the helical blades themselves.)

Consistent with the geometrical configuration treated in reference 2, $\tau(r)$ was assumed to be of the form

$$\tau(r) = \tau_0 h(r_T/r)\,\sqrt{(h^2\sigma_T^2 + 1)/(\sigma^2 + 1)} \quad (19)$$

where τ_0 is the thickness ratio at the hub. This distribution has the advantage of providing a radially

* The numerical results reported here were largely obtained using the IBM 650 Magnetic Drum Calculator at the Cornell University Computing Center.

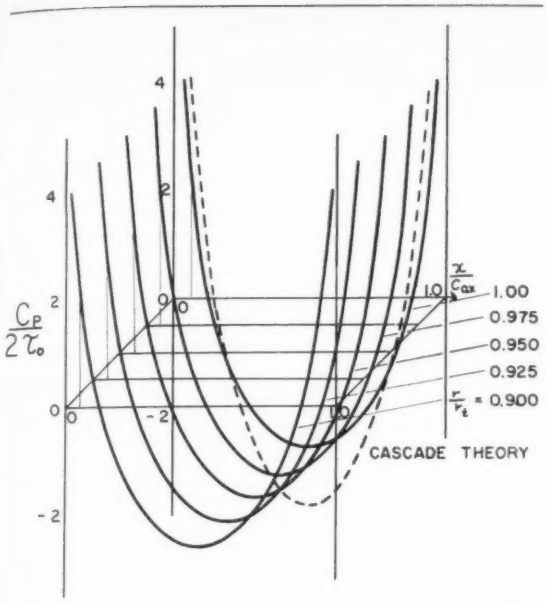

FIG. 2. Transonic pressure distribution at $M_T = 0.98$ for an axial compressor blade row with parabolic-arc profiles and $B = 64$, $h = 0.9$, $(A = 1.6)$, $L = 2C_{ax}$, $M_{ax} = 0.6$. The solid lines give the pressure coefficients over the chord at five different radial stations ranging from hub to tip. The broken line gives the corresponding results from two-dimensional cascade theory applied at the tips.

decreasing thickness as well as thickness ratio, typical of usual design.

With this particular geometry the coefficients $Q_{mB-k}(x)$ can be obtained from the set of numbers $Q_{mB-k}{}^*$ (see Table 2, reference 2) through the relations

$$Q_{mB-k}(x) = h\tau_0\sqrt{h^2\sigma_T{}^2 + 1}\; g(x)\; (Q^*{}_{mB-k}/\sigma_T) \quad (20)$$

once the profile shape is specified. For parabolic-arc profiles, such as those used for the subsonic examples in reference 2, we have

$$g(x) = 4U[1 - (2x/c_{ax})] \quad (21)$$

Finally, a value of the solidity ratio, L/c_{ax}, equal to 2.0 completes the geometrical specification of the examples.

Operating Conditions

In order to span the transonic regime, six different operating conditions for the above blade row were assumed. In each of these the axial Mach Number M_{ax} was taken equal to 0.6, and the resultant Mach Numbers at the tips,

$$M_T \equiv M_{ax}\sqrt{\sigma_T{}^2 + 1} \quad (22)$$

were given the values 0.98, 1.00, 1.033, 1.050, 1.071, and 1.090 to define the six different transonic cases. The first two Mach Numbers belong to what we shall call the "lower transonic regime," the middle three to the "mixed-flow regime." The final Mach Number, 1.090, yields a slightly supersonic relative Mach Number at the hub, but the sonic cylinder is still very near the flow annulus.

The Lower Transonic Regime—$M_T = 0.98$ and 1.00

The first two cases, with resultant tip Mach Numbers of 0.98 and 1.00, are quite similar and essentially subsonic in character. In both cases all the parameters λ_{nk} are real, the pressure distributions are symmetrical (for symmetrical blades), and no wave drag occurs. The pressure distributions given by three-dimensional, linear theory in these two cases are presented in Figs. 2 and 3 as functions of x/c_{ax} at several different radial stations. At each Mach Number, singularities at the leading and trailing edges, typical of linearized subsonic theories, appear. In both cases the singularities are integrable.

In the first case, with a tip Mach Number of 0.98, it is possible to compare the results with the pressure distribution according to the two-dimensional Prandtl-Glauert theory. It will be seen that, although the form of the distributions is similar, differences between the two are of such a magnitude as to emphasize the failure at this point of the technique developed earlier[1, 2] of computing three-dimensional "corrections" to two-dimensional theory. Three-dimensional effects take on vastly increased importance when the tip Mach Number approaches unity.

There is, of course, no linearized theory of two-dimensional flow that can be used for comparison with the three-dimensional results in Fig. 3 ($M_T = 1.0$). The very existence of these results provides a satisfying verification of the earlier conjectures of Rott,[9] and of the statements made earlier in this paper regarding three-dimensional relief of the usual transonic degeneracy of the linear theory. The form of the pressure distribution given in Fig. 3 is such as to indicate a

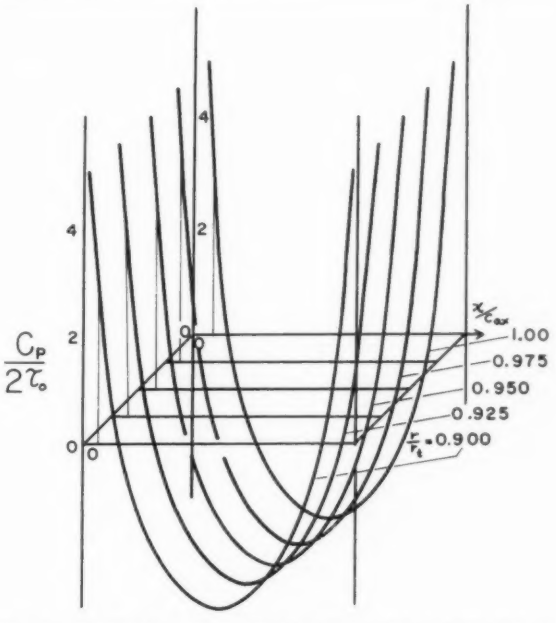

FIG. 3. Transonic pressure distribution at $M_T = 1.00$, $M_{ax} = 0.6$, for the same blade row parameters as in Fig. 2.

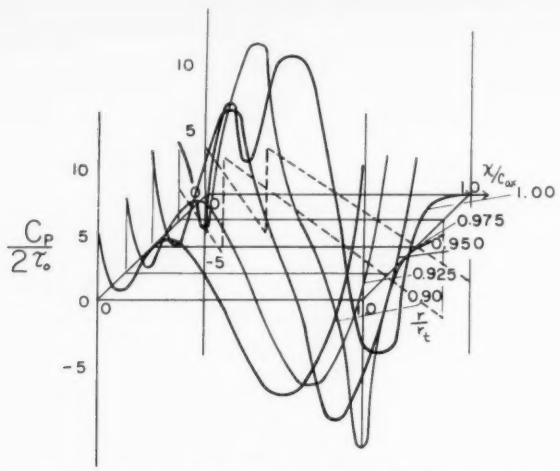

FIG. 4. Transonic pressure distribution at $M_T = 1.033$, $M_{ax} = 0.6$, for the same blade row parameters as in Fig. 2. The values of ϵ [Eq. (14)] used for this and subsequent calculations for $M_T > 1$ correspond to $Re = 6.5 \times 10^6$, $Pr = 0.7$, $\gamma = 1.4$, $\mu' = 0$. At this Mach Number the sonic cylinder is approximately midway between the hub and the tip. The broken lines represent the pressure coefficients according to Ackeret theory applied at r/r_T equal to 0.975 and 1.0.

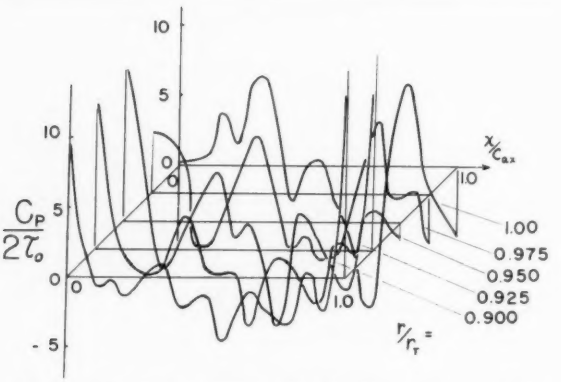

FIG. 5. Transonic pressure distribution at $M_T = 1.050$, $M_{ax} = 0.6$, for the same blade row parameter as in Fig. 2. The values of Re, Pr, γ, and μ' are the same as in Fig. 4.

smooth transition from the subsonic to the transonic regimes.

The Mixed-Flow Regime

The results for the mixed-flow regime (Figs. 4 through 6) verify still further the absence of transonic degeneracy. In these cases, however, the phenomenon of transonic acoustic resonance comes into play, and the amplitude of resonant mode must be established by taking into account viscous damping as outlined earlier. As the Mach Number M_T approaches the value for resonance of any particular mode, viscous damping affects, and finally controls, the amplitude of this mode; it turns out, however, that the viscous effects are important only in a very narrow range of Mach Number for each mode.

The values of ϵ used for these calculations are equivalent to a Reynolds Number of 6.5×10^6 with $Pr = 0.7$ and $\gamma = 1.4$, if $\mu' = 0$. They range from 2.29×10^{-7} for $M_T = 1.033$ to 2.47×10^{-7} for $M_T = 1.090$.

In spite of the smooth transition from the subsonic to the mixed-flow regimes, the pressure distributions plotted in Figs. 4–6 for $M_T = 1.033$, 1.050, and 1.071 indicate that several interesting and unusual effects remain to be explained in this range. As will be discussed below, essentially two phenomena predominate; namely, the expected transonic acoustic resonance—or, at least, near-resonance*—and strong interference between blades. At the tip Mach Number of 1.033 the phenomenon of near-resonance is particularly significant, but it also contributes to the unusual appearance of the pressure distributions at $M_T = 1.050$ and 1.071. To illustrate the importance of the near-resonant modes in the latter case, the pressure distributions at $r/r_T = 0.90$ and 1.0 are plotted again in Fig. 7 with the nearly resonant modes suppressed—i.e., with the coefficients of the nearly resonant modes put equal to zero.

At $M_T = 1.033$ the pressure distribution bears some qualitative resemblance to the Ackeret theory applied at $r/r_T = 1.0$ and $r/r_T = 0.975$. Interference from the rear portion of the blade just in advance of the one in question appears near the leading edge, as it would in the two-dimensional theory, and there is a general compression over the forward part of the blade followed

* A mode is here considered to be "nearly resonant" when its λ_{nk}^2 function is reduced by a factor of 10 or greater compared with the λ_{nk}^2 functions of the next higher and lower modes at a particular Mach Number. Exactly at resonance ($\lambda_{nk} = 0$), neither the real part nor the imaginary part of the function dominates and the only drag associated with an exactly resonant mode is that due to viscous losses. However, a mode can be nearly resonant and still have a dominantly subsonic (λ_{nk} real) or a dominantly supersonic (λ_{nk} imaginary) character. This will have an important effect on the build-up of wave drag. A given mode is on the "subsonic side" of its resonant condition if its λ_{nk} is real and on the "supersonic side" if its λ_{nk} is imaginary.

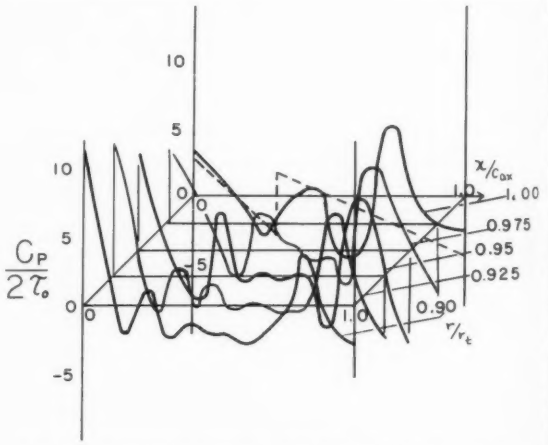

FIG. 6. Transonic pressure distribution at $M_T = 1.071$, $M_{ax} = 0.6$, for the same blade row parameters as in Fig. 2. The sonic cylinder is approximately at the hub in this case, and the values of Re, Pr, γ, and μ' are the same as in Fig. 4. The broken line represents the pressure coefficient according to Ackeret theory applied at the tips.

by an expansion rearward. The much greater magnitude of the pressure coefficients, especially near the tips, than those of the Ackeret theory is partly accounted for by the approach to acoustic resonance of the mode $m = 1, k = 1$.

At $M_T = 1.0331$, four modes are severely resonated (namely, the m–k modes 1–1, 5–2, 6–2, and 10–3), but the convergence of the series is so rapid that the 1–1 mode dominates the final results. The near-resonance of the 1–1 mode, which has a nearly constant radial amplitude, is particularly interesting because it forces the pressure distribution over the inboard half of the blading to appear largely supersonic in character, even though this portion of the blading is operating subsonically. This happens because the mode 1–1 is on the supersonic side of its exactly resonant condition. In addition, the resonance of fundamental modes such as 1–1 or 2–1 has important implications with regard to the build-up of wave drag as the tip Mach Number increases above unity. This will be discussed below.

To study further the effects of Reynolds Number in the region of resonance of the fundamental mode, numerical calculations have been made at $M_T = 1.033$ for $Re = 6.5 \times 10^4$ and $Re = 6.5 \times 10^7$ (besides 6.5×10^6). The results show that at this Mach Number the effects of viscosity in limiting the resonance of the mode 1–1 are very small when the Reynolds Number is of order 10^6 or greater, but that at $Re = 6.5 \times 10^4$ the amplitude of the near-resonant mode, and the magnitude of the resulting wave drag, are reduced significantly. These results indicate the narrowness, at typical Reynolds Numbers, of the viscous-affected range of M_T, since exact resonance of the mode 1–1 is at $M_T = 1.0292$ (see later discussion.)

Closer to resonance, viscous effects become more and more important. The amplitude at resonance of nearly all the modes, as established by viscous damping, is sufficiently small to keep these cases within the realm of the linear theory. Nevertheless, a check on the amplitude assumed by mode 1–1 at $M_T = 1.0292$ shows that if the Reynolds Number is on the order of 10^6 the nonlinear effects discussed previously must be accounted for, whereas at Reynolds Numbers on the order of 10^4 the linear theory remains sufficient. Since practical Reynolds Numbers for axial flow compressors in aeronautics fall in the range of 10^4 to 10^7, it is clear that further study may be required at a few isolated conditions of resonance.*

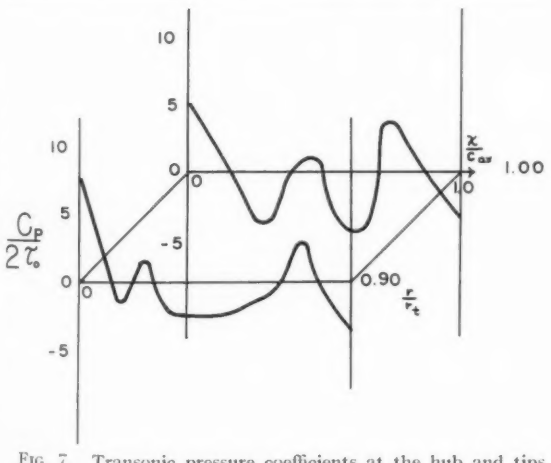

FIG. 7. Transonic pressure coefficients at the hub and tips for $M_T = 1.071$, $M_{ax} = 0.6$, with resonant modes suppressed. This Figure is constructed from Fig. 6 by subtracting the contributions of the nearly resonant modes—viz., m–k = 2–2, 3–3, 4–4, 7–6, and 10–8.

The fact that the pressure distribution at $M_T = 1.033$ is forced by the transonic resonance of the fundamental mode to take on an essentially supersonic character even inboard of the sonic cylinder is a very striking illustration of the failure in this range of any two-dimensional theory based on the strip-theory approximation. When resonant modes are excited the conditions at a given blade section can be strongly dependent on conditions at all the other blade sections. No strip-theory, or "blade-element," approximation is then possible.

At $M_T = 1.050$ (Fig. 5) modes 3–2 and 10–5 are nearly resonant, while modes 2–2 and 7–4 are also weakly excited. These resonant modes contribute to the tortured appearance of the pressure pattern; however, in contrast to the resonance of the fundamental mode, they do not force an essentially supersonic type of pressure distribution at sections operating subsonically, both because they are higher modes (having from two to four nodes over the span) and because all of them except mode 10–5 are on the *subsonic* side of their exactly resonant conditions.

Very roughly, then, the pressure pattern at $M_T = 1.050$ seems to be one that changes from a predominantly supersonic character near the tips to a predominantly subsonic character near the hub, and the changeover occurs in the region of the sonic cylinder. Superposed on this dominant pattern is a smaller-scale structure, or waviness, due primarily to the near-resonance of the modes mentioned above.

In addition to the main features just described, interference between blades, particularly interference between different radial stations of different blades, can be recognized at this Mach Number. This phenomenon is clearer, however, at $M_T = 1.071$ and will be discussed in detail for that case.

When the tip Mach Number reaches 1.071 (Fig. 6) modes 3–3, 7–6 and 10–8 become strongly resonant. In addition, modes 2–2 and 4–4 are only slightly less resonant than the above modes and also contribute to the unusual appearance of the pressure distribution. To illustrate their effect, Fig. 7 was constructed from Fig. 6 by removing the contributions of all the nearly resonant modes. Comparison of Figs. 6 and 7 will show

* On the other hand, Lighthill[2] states that the rate of acoustic attenuation in air can be from 2 to 100 times that given by Kirchhoff, due to the presence of H_2O molecules or other non-classical dissipative effects. This means that in actual practice the effective Reynolds Number for the dissipative process we are considering here can be much smaller and that the present linear treatment may be adequate for nearly all practical cases.

that the phenomenon of resonance satisfactorily accounts for the small-scale waviness of the pressure distribution over the inboard section. On the other hand, resonance will not explain the large recompression region over the entire rearward span of the blade.

This recompression cannot be explained on the basis of two-dimensional theory, either; in fact, in the transonic regime the strip theory is generally misleading. The Ackeret theory applied at the tips indicates that a disturbance from the leading edge of the tip of a given blade cannot interfere with the trailing edge of the blade in advance of it (Fig. 6). The Ackeret theory does indicate, however, that the root sections of the two blades will interfere in this way. Strip theory therefore, predicts a recompression only over part of the blade span.*

In order to understand the existence of the compression over the whole span, it is convenient to make use of the three-dimensional theory of Ordway,[10] in which the criteria for interference between points in a rotating cylindrical system are made available. It is possible, as the Ordway theory shows, for the root section near the leading edge of a given blade to interfere with the entire rearward span of the blade in advance of it. This is because the root section is operating nearly at the sonic cylinder and disturbances from this region propagate along very shallow and severely distorted Mach "cones." All this is symptomatic of the transonic regime, and close study of the Ordway theory clearly shows the failure of the two-dimensional approximation in this regime.

In sum, the pressure distributions in the transonic (mixed-flow) regime are strongly affected by the phenomenon of resonance and by patterns of interference explainable only from three-dimensional analysis. Furthermore, one is led to conclude from the Figures that the approximation of two-dimensional flow in each elemental compressor annulus breaks down, and that neither cascade theory nor cascade experiment is safely applicable in the transonic regime.

On the other hand, although some nonlinear effects remain to be investigated, the present linear theory can be regarded as largely successful in treating the transonic blade row. Indeed, it has isolated for further study such nonlinear effects as do appear important in the mixed-flow regime at some Reynolds Numbers, and has provided a complete coverage of the transonic regime at other Reynolds Numbers. Its applicability is improved (within limits) by the existence in atmospheric air of nonclassical dissipative effects.[7]

* On the other hand, two-dimensional theory does predict interference over the whole span from the rear portion of the blade just in advance of the one in question, causing the expansion region near the leading edge that is also obtained in the three-dimensional theory. It will be noted, in fact, that the Ackeret theory applied at the tips agrees very well at this particular Mach Number with the magnitude and extent of the interference region over the forward part of the blade. This close agreement must be counted as coincidental, however, since it arises from the cancellation of opposite effects. For example, when the resonant modes are suppressed (Fig. 7), the agreement is no longer more than qualitative.

The Case $M_T = 1.090$

In this case (Fig. 8) the radius of the sonic cylinder is slightly less than the hub radius and the resultant Number at the hub is greater than unity. Although this condition is not included in our definition of "transonic" (see Introduction) it is of obvious interest not only in itself but also as some indication of the way in which the theory makes its transition from the transonic to the supersonic regimes.

At this Mach Number, several important modes, including 1–2, 1–3, 2–3, and 2–4, are still subsonic in form—i.e., their λ_{mB-k}'s are still real. The resonances of these modes remain to be passed through. Also, modes 7–7 and 8–8 are mildly resonant and contribute the small-scale waviness that is still present at this Mach Number.

Aside from the effects of resonance, however, the presence of three-dimensional interference patterns, especially over the rearward portion of the blades, dominates the scene in this case. Once again, the Ackeret theory predicts qualitatively the nature of the interference pattern over the forward part of the blades, but only three-dimensional analysis can explain the recompression region over the rearward part.

It is clear, therefore, that transition, within the theory, from the transonic to the supersonic regimes is far from accomplished at $M_T = 1.090$. The sonic cylinder is still too near the flow annulus, and some important modes have not yet changed form. On the other hand, modes 1–2, 1–3, 2–3, and 2–4 will all have changed from subsonic to supersonic character by the time the tip Mach Number reaches 1.16, so it appears that more or less complete transition to the supersonic regime can safely be expected for $M_T \approx 1.20$. When this transition is accomplished, the strip theory can once again be expected to apply with reasonable accuracy.

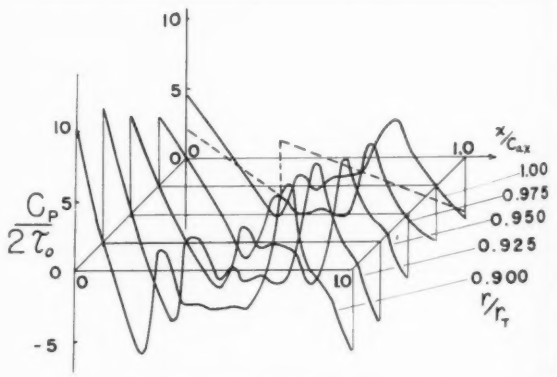

FIG. 8. Transonic pressure distribution at $M_T = 1.090$, $M_{ax} = 0.6$, for the same blade row parameters as in Fig. 2. The radius of the sonic cylinder is slightly less than the hub radius in this case. The values of Re, Pr, γ, and μ' are the same as in Fig. 4. The broken line represents the pressure coefficient according to Ackeret theory applied at the tips.

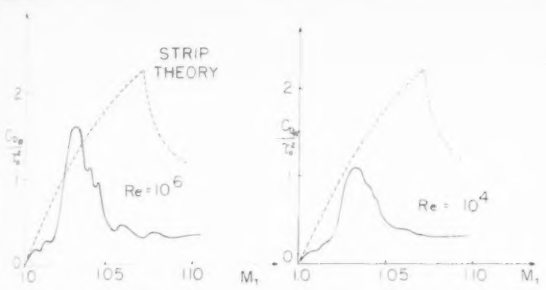

FIG. 9. Examples of two possible drag-rise curves for different Reynolds Numbers. Plotted are conjectured values of the total wave-drag coefficient (per blade) versus the tip Mach Number for a blade row of geometry similar to that of Figs. 2 through 8. The broken line indicates the values, independent of *Re*, according to two-dimensional, linearized (Ackeret) strip theory.

It should be mentioned that for tip Mach Numbers sufficiently great for all or most of the λ_{nk} to be imaginary (say $M_T \gtrsim 1.10$) the convergence of the series becomes markedly slower than in the case for lower Mach Numbers. It is then helpful to make use of the technique of averaging partial sums in order to improve the numerical accuracy of the results.

WAVE DRAG

Any finite drag obtained using the pressure coefficients computed from the present theory is identifiable as wave drag in the usual sense, with the exception that wave energy contained in resonant modes is partly lost through viscous dissipation, a process allowed for through the use of Eq. (9) in transonic, resonant cases. Nevertheless, in such transonic flows, no effort will be made to separate the two types of losses; the total drag computed will be referred to as "wave drag."

The pressure distributions plotted in Figs. 4, 5, 6, and 8 have been used to obtain the total wave drag and total torque coefficients (per blade) at the corresponding tip Mach Numbers. These results,

$$C_{DW} \equiv \int_h^1 C_d(r)\, d\left(\frac{r}{r_T}\right)$$

$$C_Q \equiv \int_h^1 C_d(r)\, \frac{r}{r_T}\, \frac{\sigma}{\sqrt{1+\sigma^2}}\, d\left(\frac{r}{r_T}\right)$$

M_T	C_{DW}/τ_0^2	C_Q/τ_0^2
1.033	1.540	1.196
1.050	0.544	0.396
1.071	0.305	0.233
1.090	0.312	0.2355

provide an interesting indication on the behavior of the drag-rise curve as the tip Mach Number increases above unity. They do not, of course, provide adequate numerical information for the complete determination of the wave-drag build-up, because of the severe rate of change of pressure distribution with Mach Number in this range.

However, the four pressure patterns given, indicating as they do the importance of transonic resonance, suggest that the drag-rise curve also will be importantly affected by resonance, and hence by Reynolds Number! When a fundamental mode is nearly resonant at a supersonic tip Mach Number just below its exactly resonant condition ($\lambda_{nk} = 0$), it will contribute very little to the drag (by definition of resonance). But immediately above resonance it will change from a predominantly subsonic to a predominantly supersonic character and will still be greatly amplified. It will then immediately contribute strongly to the drag.

These considerations and the results already obtained lead to the conjecture that two typical drag-rise curves at different Reynolds Numbers might be of the forms shown in Fig. 9. Successive bumps in these curves correspond to successive modes becoming resonant. Further numerical study of this problem would be of considerable interest, and such a study should provide information that could be checked experimentally. Indeed, if the conjectured "fine structure" of the drag-rise curve does in fact exist, experimental study of its magnitude and significance would appear to be important.

In Fig. 9, the drag-rise curves computed according to two-dimensional strip theory are plotted for comparison purposes. Although the section drag at the sonic cylinder tends to infinity at the sonic cylinder if Ackeret theory is applied there, the resulting singularity is integrable and the *total* drag computed in this way is finite.

THE MACH NUMBER OF RESONANCE

The foregoing numerical results illustrate the importance of transonic resonance, as regards its effect both on the pressure distribution and on the wave drag associated with thickness. Indeed, they lead one to the conclusion that for axial compressors the really significant Mach Number in the transonic range is not $M_T = 1.0$ but rather the resultant Mach Number for which the fundamental mode $m = 1$, $k = 1$ becomes resonant. (The resultant Mach Number for which other low modes, such as 2–1, 3–1, 1–2, 2–2, etc., are resonant are also important, of course. Their values can easily be obtained from the formulas given below and from Fig. 3 of reference 2.)

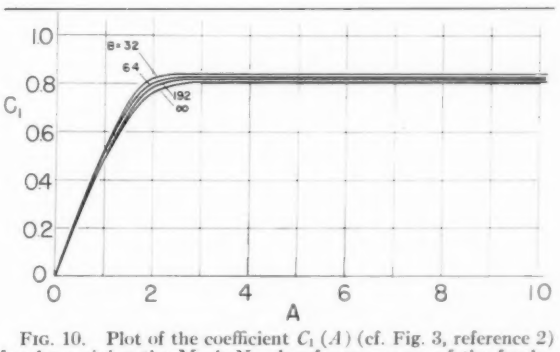

FIG. 10. Plot of the coefficient $C_1(A)$ (cf. Fig. 3, reference 2) for determining the Mach Number for resonance of the fundamental mode. The parameter $A = B^{2/3}(1 - h)$. See Eqs. (24) and (25). For $m \neq 1$, replace B by mB and A by $Am^{2/3}$.

In general, the resonance condition is given by Eq. (4) with $n = mB$. Using the formulas for the eigenvalues K_{nk} in terms of the coefficients C_k, and the fact that $\sigma_S = \beta/M_{ax}$, we obtain for resonance,

$$(\{M_T^{(m-k)}\}^2 - 1)/\beta^2 = 2C_k(A m^{2/3})/m^{2/3}B^{2/3} \quad (23)$$

where $M_T^{(m-k)}$ is the resultant tip Mach Number for resonance of the mode m–k.

In particular, we have for resonance of the fundamental mode

$$M_T^{(1-1)} = \sqrt{1 + [2C_1(A)\beta^2/B^{2/3}]} \quad (24)$$

Values of $C_1(A)$ are plotted in Fig. 10 for $A \equiv B^{2/3}(1 - h)$ ranging from 0 to 10.* It will be seen that these results form an almost universal curve for $B > 32$. Using this figure and Eq. (24), the values of $M_T^{(1-1)}$ can readily be found for any given configuration.

At $M_T^{(1-1)}$ the wave drag of an axial compressor should, according to the theory, increase significantly, and $M_T^{(1-1)}$ is therefore an important design parameter. For tip Mach Numbers below $M_T^{(3-1)}$ or $M_T^{(4-1)}$ the wave drag should be very small; hence these tip Mach Numbers, lying between 1.0 and $M_{T1}^{(1-1)}$, are also of interest. They may readily be obtained from the relations

$$M_T^{(m-1)} = \sqrt{1 + [2C_1(A m^{2/3})\beta^2/m^{2/3}B^{2/3}]} \quad (25)$$

and Fig. 10.

Another important fact that can be deduced from Fig. 10 is that for $A \geq 2.5$, resonance of the fundamental mode $m = 1$, $k = 1$ will not, as in Fig. 4, force a supersonic-type pressure pattern over the whole blade. This is because, as $C_1(A)$ approaches its asymptotic value for large A, the phase angles δ_{mB-1} in the definition[2] of the functions R_{mB} approach zero strongly (cf. Figs. 3 and 4 of reference 2) and then each function $R_{mB}[K_{mB-1}(r/r_T)]$ is very nearly zero near the hub. Thus, for hub ratios smaller than that used in the present set of examples, resonance of the fundamental mode may not be so disruptive of the pressure distribution near the blade roots.

Conclusions

A linear theory has been developed that can be successfully applied to axial compressor blade rows operating transonically. Although the theory is equally applicable to lifting as well as nonlifting blade rows, detailed study of only the nonlifting, or thickness, problem has been carried out to date. Numerical examples have been worked out, and these examples verify the success of the linear theory in the transonic regime. Even so, they also indicate the possibility that for some configurations certain nonlinear effects might be important when resonance of the fundamental mode occurs.

The numerical results illustrate the importance of transonic resonance and lead to introduction of the resultant Mach Number for resonance as an important design parameter. They also emphasize the failure of any strip theory or "blade-element" approximation for axial compressor blade rows operating in the transonic regime, thus leading to the conclusion that neither cascade theory nor cascade experiment can safely be applied to transonic blade rows.

* The value of $M_T^{(1-1)}$ in the present example ($A = 1.6$) is 1.0292.

References

[1] McCune, James E., *The Three-Dimensional Flow Field of an Axial Compressor Blade Row—Subsonic, Transonic and Supersonic*, Ph.D. Thesis, Cornell University, 1958. (See also AFOSR TN 58-72, ASTIA number AD 148 116 and 117.)

[2] McCune, James E., *A Three-Dimensional Theory of Axial Compressor Blade Rows—Application in Subsonic and Supersonic Flows*, Journal of the Aeronautical Sciences, Vol. 25, No. 9, pp. 544–560, 1958.

[3] Watson, G. N., *A Treatise on the Theory of Bessel Functions*, Second Edition Revised; Dover Publications, New York, 1945.

[4] Olver, F. W. J., Philosophical Transactions of the Royal Society, Series A, No. 247, pp. 307–368, 1955.

[5] Davidson, Robert E., *Linearized Potential Theory of Propeller Induction in a Compressible Flow*, NACA TN 2983, 1953.

[6] Strutt, John William (Lord Rayleigh), *The Theory of Sound*, Volume II, Second Edition Revised; Dover Publications, New York, 1945.

[7] Lighthill, M. J., *Viscosity Effects in Sound Waves of Finite Amplitude*, Surveys in Mechanics, the G. I. Taylor 70th Anniversary Volume, Edited by G. K. Batchelor & R. M. Davies; Cambridge University Press, 1956.

[8] Maslen, S. H., and Moore, F. K., *On Strong Transverse Waves Without Shocks in a Circular Cylinder*, Journal of the Aeronautical Sciences, Vol. 23, No. 6, page 583, June, 1956.

[9] Rott, Nicholas, *On Wave Radiation in Compressible Flow through an Axial Compressor*, Published in Abstract, American Physical Society, The Physical Review, 84, page 613, 1951.

[10] Ordway, Donald E., *An Aerodynamic Theory of a Supersonic Propeller*, Ph.D. Thesis, Cornell University, 1956. Also AFOSR TN 56-287, ASTIA number AD 89498.

Thermal Stress in Curved Beams

BRUNO A. BOLEY* AND EUVAL S. BARREKETTE**

Columbia University

SUMMARY

Thermoelastic stresses are investigated in curved beams of constant properties and constant cross section under temperatures varying in the radial direction only. Good agreement is found between stresses as calculated from elasticity theory and from strength-of-materials theory which assumes that plane sections remain plane. A comparison with the corresponding straight-beam formula is also included.

INTRODUCTION

THE STRESS ANALYSIS of curved beams is based, in strength-of-materials theory, on the assumption that plane sections remain plane; when the depth-to-radius ratio is small, it is permissible to further simplify the analysis by disregarding entirely the effect of curvature—that is, by employing the elementary formulas of straight-beam theory. A comparison between the results of these approximate analyses with the corresponding ones of elasticity theory may be found, for example, in reference 1, for a rectangular beam with a circular median line under a pure bending moment; it shows that the strength-of-materials approach is quite accurate for most beams, and it indicates the limits of applicability of the straight-beam equations. It is the purpose of the present work to perform the analogous comparison for curved beams under the action of nonuniform heating. The principal results are presented and discussed in the next section of this paper; the derivations of the pertinent equations are given in Sections 2 and 3. Additional details may be found in reference 2.

(1) PRESENTATION AND DISCUSSION OF RESULTS

Consider a curved beam of arbitrary constant cross section and with constant properties, the centerline of which is an arc of a circle lying in one of the centroidal principal planes (Fig. 1), under a temperature T varying only in the radial direction. An approximate formula for the stress σ_θ in such a beam may be derived on the basis of the strength-of-materials assumption that plane sections remain plane, and is (Section 2):

$$\sigma_\theta/\alpha E = -T + (1/A)\int T dA + (1/A)\left[\int T\eta\, dA - \int\left(\int_{\eta_0}^{\eta} T d\eta\right) dA\right][\beta(\eta_0 - \eta)/\eta_0(1+\beta\eta)] + [\beta/(1+\beta\eta)]\int_{\eta_0}^{\eta} T\, d\eta - [\beta\eta(1+\beta\eta_0)/\eta_0(1+\beta\eta)]\,(1/A)\int\left[\left(\int_{\eta_0}^{\eta} T d\eta\right)\Big/(1+\beta\eta)\right] dA \quad (1)$$

where α is the coefficient of thermal expansion, E Young's modulus, A the cross-sectional area. All unspecified limits of integration must be chosen so as to cover this entire area, and

$$\beta = h/R,\ \eta = z/h,\ \eta_0 = (1/\beta)\,[(r_0/R) - 1] \quad (1a)$$

The dimension r_0 is a function of the cross-sectional geometry and is defined by the equation

$$\int [y\, dA/(r_0 + y)] \equiv A - r_0 \int [dA/(r_0 + y)] = 0 \quad (1b)$$

and therefore specifies the location of the neutral axis for a beam in pure bending at constant temperature (explicit expressions for r_0 for several cross sections are given in reference 3); all other geometrical quantities are defined in Fig. 1.

The formula for straight beams, analogous to Eq. (1), is[4]

$$\sigma_\theta/E\alpha = -T + (1/A)\int T\, dA + (h^2\eta/I)\int T\eta\, dA \quad (2)$$

where the moment of inertia I is

$$I = h^2 \int \eta^2\, dA \quad (3)$$

Eq. (2) should provide a reasonable approximation to Eq. (1) for beams of small depth-to-radius ratio. In fact, the first term of the series expansion of the right-hand side of Eq. (1) in powers of β is identical with the right-hand side of Eq. (2). The expansion in question is given in the second row of Table 1. Further remarks concerning the accuracy of Eq. (2) for curved beams are given later.

In order to estimate the accuracy of the stresses calculated from Eq. (1), they are compared with those obtained from an equation based on elasticity theory for the special case of a beam with a rectangular cross section of inner radius a and outer radius b. For such a cross section the geometrical parameters for Eq. (1) are

$$r_0 = (b-a)/\ln(b/a);\quad \eta_0 = [1/\ln(b/a)] - [(b+a)/2(b-a)] \quad (4)$$

and the elasticity solution for the stress σ_θ is (see Section 3):

Received December 26, 1957.

* Professor of Civil Engineering, Institute of Flight Structures.
** Research Assistant, Institute of Flight Structures.

$$\sigma_\theta = -(A_1/r^2) + (A_2/a^2)\,[2\ln(r/a) + 3] + (2A_3/a^2) - E\alpha\left[T - (1/r^2)\int_a^r T\,r\,dr\right] \tag{5}$$

where

$$\begin{aligned}
A_1 &= (E\alpha/N) \times \left(\left\{2(b/a)^2\ln(b/a)\,[2\ln(b/a) - 1] + (b/a)^2 - 1\right\}\int_a^b T\,r\,dr - 4(b/a)^2\ln(b/a)\int_a^b T r\ln(r/a)\,dr\right)\\
A_2 &= (E\alpha/N)\left\{[2(b/a)^2\ln(b/a) - (b/a)^2 + 1]\int_a^b T r\,dr - 2[(b/a)^2 - 1]\int_a^b T r\ln(r/a)\,dr\right\}\\
A_3 &= (E\alpha/N)\left\{-2(b/a)^2\,[\ln(b/a)]^2\int_a^b T r\,dr + [2(b/a)^2\ln(b/a) + (b/a)^2 - 1]\int_a^b T r\ln(r/a)dr\right\}\\
N &= 4(b/a)^2\,[\ln(b/a)]^2 - [(b/a)^2 - 1]^2
\end{aligned} \tag{5a}$$

The right-hand side of Eq. (5) may also be expanded in powers of β, as shown in the fourth row of Table 1. The first term of this expansion is identical with the right-hand side of Eq. (2), for the special case of a rectangular section.

The third and fourth rows of Table 1 represent the expansions in powers of β corresponding respectively to Eq. (1) (for the special case of a rectangular section) and to Eq. (5). It may be noted that the first and second terms of these expansions are identical; it is therefore reasonable to expect that the two formulas will yield very similar numerical results, especially for beams with a small value of β.* To make a quantitative comparison, numerical results were obtained from Eqs. (1), (2), and (5) for three special temperature distributions—namely, a constant ($T = T_0$), a linear variation ($T = T_1 z/a$), and a quadratic variation ($T = T_2 z^2/a^2$). For a constant temperature, all three equations yield the same result—namely, $\sigma_\theta = 0$—and all may therefore be considered to be equally valid. Since these equations are linear in T, this result implies that the addition of a constant term to any temperature distribution will not alter the resulting stresses.

For a linear temperature variation, the result $\sigma_\theta = 0$ again follows from Eq. (2), but not from Eqs. (1) and (5); here the straight-beam formula is clearly not adequate. Eq. (1) is, however, quite accurate, as may be seen from Fig. 2. The approximate maximum stress (at $r = a$) differs from the exact one by about -2.4, -0.8, and -0.06 per cent of the latter for $b/a = 3$, 2, and 1.2, respectively. The location of the maximum tensile (for $T_1 > 0$) stress, as calculated from the two theories, is given in Table 3. An example, corresponding to Eq. (5), of the stress distribution across the selection is presented in Fig. 3.

The analogous comparison for a quadratic temperature distribution is shown in Fig. 4. Again Eq. (1) is quite accurate; the approximate maximum stress differs from the exact one by about -4.9, -0.7, and -0.44 per cent of the latter, respectively for $b/a = 3$, 2, and 1.2 (i.e., for $\beta = 1$, 0.667, and 0.182, respectively). The location of the maximum tensile (for $T_2 > 0$) stress, as calculated from the two theories, is given in Table 4. In this case the straight-beam formula does not give zero stress, but a comparison between its results and those of the other theories is difficult to make because only with Eq. (2) does the addition of a linear term in the temperature not alter the stresses. If the linear term is small compared to the quadratic one, the straight-beam formula is reasonably accurate. For example, in the present case ($T = T_2 z^2/a^2$) the maximum stress given by the straight-beam formula differs from the exact one by about $+13.7$, $+8.7$, and $+1.5$ per cent of the latter, for $b/a = 3$, 2, and 1.2, respectively. Note that the straight-beam theory gives equal stresses at $z = \pm h/2$, while the other theories do not.

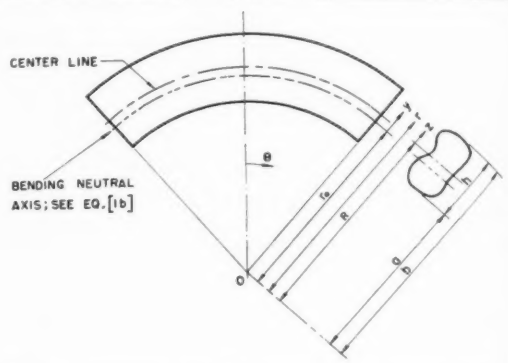

FIG. 1. Geometry and sign convention for curved beam.

It appears from the above discussion that Eq. (1) is likely to be satisfactory for most practical cases. It is worth noting that even in the case of a rectangular beam Eq. (1) is much simpler to use, from the standpoint of numerical calculation, than Eq. (5); for example, for the quadratic temperature distribution, Eq. (1) reduces to

$$\sigma_\theta/E\alpha T_2 = (h^2/3a^2)\,[1/(1+\beta\eta)]\left\{-2\eta^3\beta - 3\eta^2 + \eta[(\beta/6) - (1/12\eta_0) - (1/\beta)] + (1/4)\right\} \tag{6}$$

* The expansions in powers of β, analogous to those of Table 1, for a beam in pure bending at a constant temperature, are presented in Table 2. The elasticity theory and the strength-of-materials formulas from which these expansions were derived are given in references 1 and 3, respectively. It may be noted that the first term of each expansion gives the appropriate straight-beam stress, and that the first and second terms of the last two rows are identical. The results of the thermal case are thus entirely analogous to those of the nonthermal one.

TABLE I

$$\frac{\sigma_\phi}{E\alpha} = \sum_{i=0}^{\infty} a_i \beta^i$$

THEORY	SECTION	a_0	a_1	a_2	a_3
STRAIGHT BEAM EQ. [2]	ARBITRARY	$-T + \frac{1}{A}\int T\,dA + \frac{\eta h^2}{I}\int T\eta\,dA$			
STRENGTH OF MATERIALS EQ. [1]	ARBITRARY	$-T + \frac{1}{A}\int T\,dA + \frac{\eta h^2}{I}\int T\eta\,dA$	$\left(\frac{1}{A} - \frac{\eta^2 h^2}{I} + \frac{\eta h^4}{I^2}\int \eta^2\,dA\right)\int T\eta\,dA$ $-\frac{1}{A}\int\left(\int_{\eta_0}^{\eta} T\,d\eta\right)dA$ $-\frac{\eta h^2}{I}\int \eta\left(\int_{\eta_0}^{\eta} T\,d\eta\right)dA + \int_{\eta_0}^{\eta} T\,d\eta$	$\left[\frac{\eta^2 h^2}{I} - \frac{\eta^2 h^4}{I^2}\int \eta^3\,dA + \frac{\eta h^6}{I^3}\left(\int \eta^2 dA\right)^2 - \frac{\eta h^4}{I^2}\int \eta^4\,dA\right]\int T\eta\,dA$ $+\left(\frac{\eta^2 h^2}{I} - \frac{\eta h^4}{I^2}\int \eta^2 dA\right)\int \eta\left(\int_{\eta_0}^{\eta} T\,d\eta\right)dA$ $+\frac{\eta h^2}{I}\int \eta^2\left(\int_{\eta_0}^{\eta} T\,d\eta\right)dA - \int_{\eta_0}^{\eta} T\,d\eta$	$\left[-\frac{\eta^4 h^2}{I} + \frac{\eta^3 h^4}{I^2}\int \eta^2 dA - \frac{\eta^2 h^6}{I^3}\left(\int \eta^2 dA\right)^2 + \frac{\eta h^8}{I^4}\left(\int \eta^2 dA\right)^3 - \frac{2\eta h^6}{I^3}\int \eta^2 dA\int \eta^4 dA + \frac{\eta^2 h^4}{I^2}\int \eta^4 dA + \frac{\eta h^6}{I^3}\int \eta^6 dA\right]\int T\eta\,dA$ $+\left[\frac{\eta^3 h^2}{I} + \frac{\eta^2 h^4}{I^2}\int \eta^2 dA - \frac{\eta h^6}{I^3}\left(\int \eta^2 dA\right)^2 + \frac{\eta h^6}{I^3}\int \eta^4 dA\right]\int \eta\left(\int_{\eta_0}^{\eta} T\,d\eta\right)dA$ $+\left(-\frac{\eta^2 h^2}{I} + \frac{\eta h^4}{I^2}\int \eta^2 dA\right)\int \eta^2\left(\int_{\eta_0}^{\eta} T\,d\eta\right)dA$ $-\frac{\eta h^2}{I}\int \eta^3\left(\int_{\eta_0}^{\eta} T\,d\eta\right)dA + \eta^2\int_{\eta_0}^{\eta} T\,d\eta$
	RECTANGULAR	$-T + \int T\,d\eta + 12\eta\int T\eta\,d\eta$	$\left(-\frac{3}{2}\eta - \frac{1}{2}\right)\int T\,d\eta + (-12\eta^2+2)\int T\eta\,d\eta$ $+6\eta\int T\eta^2 d\eta + \int_{-\frac{1}{2}}^{\eta} T\,d\eta$	$\left(\frac{3}{2}\eta^2 + \frac{1}{2}\eta\right)\int T\,d\eta + (12\eta^2 - \frac{9}{5}\eta)\int T\eta\,d\eta$ $-6\eta^2\int T\eta^2 d\eta - 4\eta\int T\eta^3 d\eta - \eta\int_{-\frac{1}{2}}^{\eta} T\,d\eta$	$\left(-\frac{3}{2}\eta^3 - \frac{1}{2}\eta^2 + \frac{3}{80}\eta\right)\int T\,d\eta + (-12\eta^4 + \frac{3}{5}\eta^2)\int T\eta\,d\eta$ $+(6\eta^3 - \frac{9}{10}\eta)\int T\eta^2 d\eta + 4\eta^2\int T\eta^3 d\eta$ $+3\eta\int T\eta^4 d\eta + \eta^2\int_{-\frac{1}{2}}^{\eta} T\,d\eta$
ELASTICITY EQ. [5]	RECTANGULAR	$-T + \int T\,d\eta + 12\eta\int T\eta\,d\eta$	$\left(-\frac{3}{2}\eta - \frac{1}{2}\right)\int T\,d\eta + (-12\eta^2+2)\int T\eta\,d\eta$ $+6\eta\int T\eta^2 d\eta + \int_{-\frac{1}{2}}^{\eta} T\,d\eta$	$(2\eta^2+\eta+\frac{1}{12})\int T\,d\eta + (4\eta^3 - \frac{18}{5}\eta - \frac{1}{2})\int T\eta\,d\eta$ $+\left(-6\eta^2 + \frac{1}{2}\right)\int T\eta^2 d\eta - 2\eta\int T\eta^3 d\eta$ $-2\eta\int_{-\frac{1}{2}}^{\eta} T\,d\eta + \int_{-\frac{1}{2}}^{\eta} T\eta\,d\eta$	$\left(-\frac{31}{12}\eta^2 - \frac{3}{2}\eta^2 - \frac{7}{40}\eta\right)\int T\,d\eta + \left(-\frac{33}{2}\eta^4 + \frac{107}{20}\eta^2 + \eta - \frac{1}{168}\right)\int T\eta\,d\eta$ $+(7\eta^3 - \frac{21}{20}\eta)\int T\eta^2 d\eta + (2\eta^2 - \frac{1}{6})\int T\eta^3 d\eta$ $+\eta\int T\eta^4 d\eta + 3\eta^2\int_{-\frac{1}{2}}^{\eta} T\,d\eta - 2\eta\int_{-\frac{1}{2}}^{\eta} T\eta\,d\eta$

Series expansions for thermal stresses in curved beams.

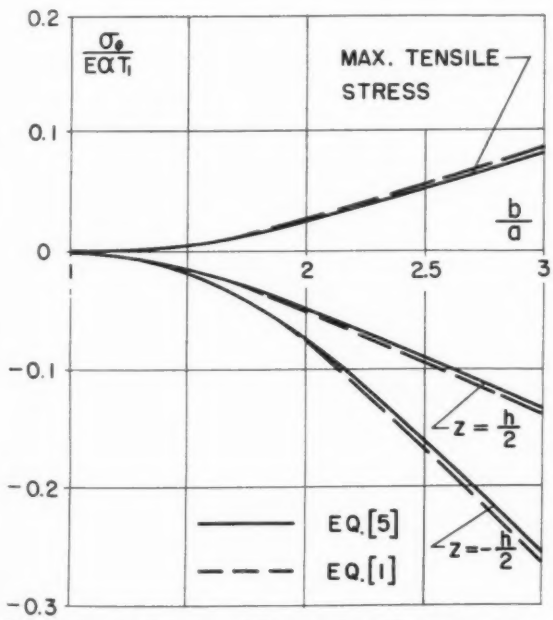

FIG. 2. Stresses in a curved beam under a linear temperature distribution, $T = T_1(z/a)$, $T_1 > 0$.

TABLE II

$$\frac{\sigma_\phi}{(Mh/I)} = \sum_{i=0}^{\infty} a_i \beta^i$$

THEORY	SECTION	a_0	a_1	a_2	a_3
STRAIGHT BEAM	ARBITRARY	η			
STRENGTH OF MATERIALS	ARBITRARY	η	$\frac{1}{A^2}\eta + \frac{\eta h^2}{I}\int \eta^2 dA$	$\eta^2\frac{\eta h^2}{I}\int \eta^2 dA + \frac{\eta h^4}{I^2}\int \eta^4 dA - \frac{\eta h^2}{I^2}\int \eta^2 dA$	$-\eta^3\frac{\eta^2 h^2}{I}\int \eta^2 dA - \frac{\eta^2 h^4}{I^2}\int \eta^2 dA)^2 + \frac{2\eta h^6}{I^3}\int \eta^2 dA\int \eta^4 dA + \frac{\eta^2 h^4}{I^2}\int \eta^4 dA + \frac{\eta h^6}{I^3}\int \eta^6 dA$
	RECTANGULAR	η	$-\eta^2 + \frac{1}{12}$	$\eta^2 - \frac{3}{20}\eta$	$-\eta^3 + \frac{3}{20}\eta^2$
ELASTICITY	RECTANGULAR	η	$-\eta^2 + \frac{1}{12}$	$\frac{7}{6}\eta^2 - \frac{7}{40}\eta$	$-\frac{11}{8}\eta^3 + \frac{97}{240}\eta^2 - \frac{7}{1152}$

Series expansions for unheated curved beams in pure bending.

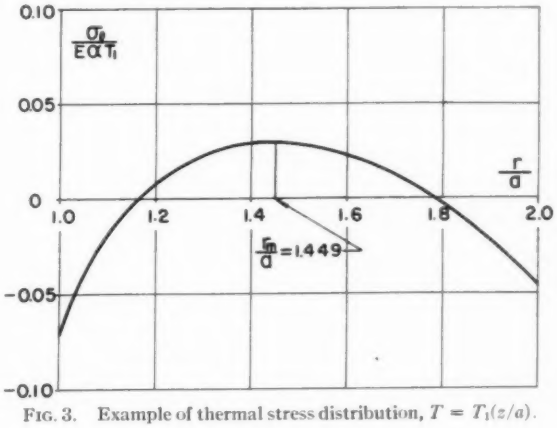

FIG. 3. Example of thermal stress distribution, $T = T_1(z/a)$.

while Eq. [5] remains essentially of the same form as previously given.

(2) Derivation of Eq. (1)

A view of a deformed element of the beam of Fig. 1 is shown in Fig. 5. The new length, after heating, of a fiber originally of length $[(r_0 + y)d\theta]$ is

$$\left[\left(r_0' + y + \int_0^y \alpha T dy\right)(d\theta + \Delta d\theta)\right]$$

Table 3
Location of Maximum Tensile Stress for $T = T_1(z/a)$, $T_1 > 0$

b/a	(r_m/a) for Eq. (1)	(r_m/a) for Eq. (5)
3	1.839	1.842
2	1.448	1.449
1.2	1.097	1.096

Table 4
Location of Maximum Tensile Stress for $T = T_2(z/a)^2$, $T_2 > 0$

b/a	(r_m/a) for Eq. (1)	(r_m/a) for Eq. (5)
3	1.946	1.960
2	1.483	1.484
1.2	1.099	1.098

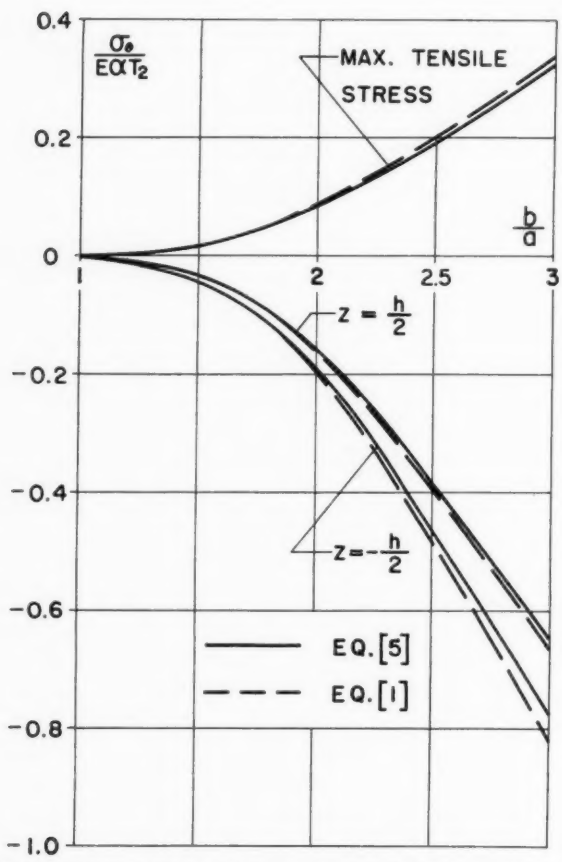

Fig. 4. Stresses in a curved beam under a quadratic temperature distribution, $T = T_2(z/a)^2$, $T_2 > 0$.

provided that plane sections remain plane. The strain is thus

$$\epsilon_\theta = [1/(r_0 + y)]\left\{r_0' - r_0 + \int_0^y \alpha T dy + (\Delta d\theta/d\theta)\left(r_0' + y + \int_0^y \alpha T dy\right)\right\} \quad (7)$$

Noting, however, that

$$\int_0^y \alpha T dy \ll y \quad (7a)$$

and introducing Hooke's law, one obtains:

$$\epsilon_\theta = [1/(r_0 + y)]\left\{r_0' - r_0 + \int_0^y \alpha T dy + (\Delta d\theta/d\theta)(r_0' + y)\right\} = (\sigma_\theta/E) + \alpha T \quad (8)$$

The two unknowns r_0' and $(\Delta d\theta/d\theta)$ are to be found from the equilibrium conditions

$$\int \sigma_\theta dA = \int \sigma_\theta y dA = 0 \quad (9)$$

The expression for the stress is then

$$\sigma_\theta = -E\alpha T + [E\alpha/(r_0 + y)] \times \left((r_0/A)\left\{\int T dA - \int\left[\left(\int_0^y T dy\right)\Big/(r_0 + y)\right]dA\right\} + \left(y\Big/\int y dA\right)\left\{\int T y dA - \int\left[\left(y\int_0^y T dy\right)\Big/(r_0 + y)\right]dA\right\} + \int_0^y T dy\right) \quad (10)$$

Eq. (1) results immediately from this formula with the introduction of the notation of Eqs. (1a) and with

$$y = h(\eta - \eta_0), \quad \int \eta dA = 0 \quad (10a)$$

(3) Derivation of Eqs. (5)

The governing equation of the present two-dimensional plane stress problem in terms of the Airy stress function ϕ is:

$$\nabla^4\phi = -\alpha E \nabla^2 T \quad (11)$$

(*Continued on page 643*)

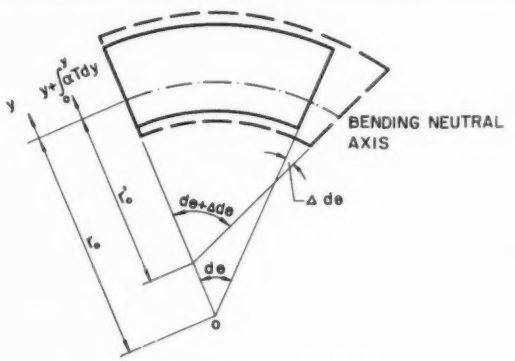

Fig. 5. Deformed element of curved beam.

The Boundary-Layer Equation for Axially Symmetric Flow Past a Body of Revolution—Motion of a Sphere

DAVID MEKSYN*

SUMMARY

The equations of the boundary layer for an axially symmetric flow past a solid of revolution are reduced to a form identical with that derived by the author for plane flow. This method is applied to the case of a flow past a sphere, and the frictional force and the separation point are evaluated.

The equation is integrated asymptotically by the method developed for plane flow, where the partial differential equation is reduced to an ordinary equation. A new straightforward method of step-by-step integration of this equation is used.

INTRODUCTION

THE EQUATIONS of the boundary layer for plane flow were transformed by the author[1] to an equation in which the boundary conditions are independent of the velocity at the edge of the boundary layer. The equation contains a gage invariant function which is of decisive importance in connection with the phenomenon of separation; it is also easier to integrate than the usual boundary-layer equations.

A short derivation of this equation was recently given by Goertler.[2]

In the present paper an identical equation is derived for axially symmetric flow past a body of revolution, by making use of Mangler's[3] procedure which transforms the usual boundary-layer equations for axially symmetric flow to those of a plane flow.

The equation is applied to find the friction and the separation point for a flow past a sphere, measured by Fage.[4]

(1) THE BOUNDARY-LAYER EQUATION

Consider an axially symmetric flow past a solid of revolution. The coordinates x, y are taken along and normal to the meridian curve δ, respectively, u, v are the corresponding velocities, and r is the radius of revolution (distance from the axis).

The boundary-layer equations of motion and continuity are

$$\left.\begin{aligned} u(\partial u/\partial x) + v(\partial u/\partial y) &= U_0{}^2U_1(dU_1/Ux) + \nu(\partial^2 u/\partial y^2) \\ (\partial/\partial x)(ru) + (\partial/\partial y)(rv) &= 0 \end{aligned}\right\} \tag{1.1}$$

where U_0 is the velocity at infinity (directed along the axis of rotation) and U_0U_1 is the velocity at the edge of the boundary layer.

Changing the variables, let

$$\left.\begin{aligned} \alpha = \int_0^x [r^2(x)U_1/l^2]dx, \quad \beta &= U_1(r/l)y \\ u = U_1u', \quad v &= U_1v' \end{aligned}\right\} \tag{1.2}$$

where l is an appropriate length.

Mangler's transformation[3] is obtained from Eqs. (1.2) by putting $U_1 = 1$.

For an arbitrary function $f(x, y)$, we have

$$\left.\begin{aligned} (\partial f/\partial x)_y = (r^2/l^2)U_1(\partial f/\partial\alpha)_\beta + \\ (\partial f/\partial\beta)_\alpha(\partial/\partial x)[(U_1r/l)y] = (r^2/l^2)U_1 \times \\ (\partial f/\partial\alpha) + (\partial f/\partial\beta)[\beta(\partial/\partial x)(U_1r/l)/(U_1r/l)] \\ (\partial f/\partial y)_x = (rU_1/l)(\partial f/\partial_\beta)_\alpha \end{aligned}\right\} \tag{1.3}$$

whence the equation of continuity is transformed to

$$\left.\begin{aligned} (\partial\bar{u}/\partial\alpha) + (\partial\bar{v}/\partial\beta) &= 0 \\ \text{where} & \\ \bar{u} = u', \quad \bar{v} &= (l/r)\{[(U_1r)_x/U_1r]u'y + v'\} \end{aligned}\right\} \tag{1.4}$$

and the subscript x in Eqs. (1.4) denotes differentiation with respect to x, when y is constant.

Transforming similarly the equation of motion, we find

$$\bar{u}(\partial\bar{u}/\partial\alpha) + \bar{v}(\partial\bar{u}/\partial\beta) = (U_0{}^2 - \bar{u}^2)(d\ln U_1{}^2/d\alpha) + \nu(\partial^2\bar{u}/\partial\beta^2) \tag{1.5}$$

Introducing a stream function $\psi(\alpha, \beta)$, such that

$$\bar{u} = \partial\psi/\partial\beta, \quad \bar{v} = -\partial\psi/\partial\alpha \tag{1.6}$$

and new variables

$$\sigma = (U_0/2\nu\alpha)^{1/2}\beta, \quad \psi = (2\nu U_0\alpha)^{1/2}f(\sigma, \alpha) \tag{1.7}$$

we find

$$\left.\begin{aligned} \partial\psi/\partial\beta &= U_0(\partial f/\partial\sigma) = \bar{u} \\ \partial\psi/\partial\alpha = (2\nu U_0\alpha)^{1/2}&[(f/2\alpha) + (\partial f/\partial\alpha) - \\ &(\sigma/2\alpha)(\partial f/\partial\sigma)] \end{aligned}\right\} \tag{1.8}$$

The equation of motion becomes[5]

$$\left.\begin{aligned} (\partial^3 f/\partial\sigma^3) + f(\partial^2 f/\partial\sigma^2) = \lambda[1 - (\partial f/\partial\sigma)^2] + \\ 2\alpha\{(\partial f/\partial\sigma)(\partial^2 f/\partial\sigma\partial\alpha) - (\partial f/\partial\alpha)/(\partial^2 f/\partial\sigma^2)\} \\ \text{where} \qquad \lambda = -\alpha(d\ln U_1{}^2/d\alpha) \end{aligned}\right\} \tag{1.9}$$

The boundary conditions are

Received January 2, 1957.

* % Mathematics Department, Royal College of Science, London.

The author wishes to thank Prof. J. G. Semple for permission to use the computing facilities of the Mathematics Department, King's College, London.

$$f = \partial f/\partial\sigma = 0, \quad \text{at} \quad \sigma = 0$$
$$\partial f/\partial\sigma = 1, \quad \text{at} \quad \sigma = \infty \tag{1.10}$$

For the separation point, the additional condition is

$$\partial^2 f/\partial\sigma^2 = 0, \quad \text{at} \quad \sigma = 0 \tag{1.11}$$

(2) Frictional Force

The frictional stress F is equal to

$$F = \mu(\partial u/\partial y)_{y=0} \tag{2.1}$$

Now,

$$\partial u/\partial y = (U_0 U_1^2 r/l)(U_0/2\nu\alpha)^{1/2}(\partial^2 f/\partial\sigma^2)$$

whence, after a few transformations,

$$C_F = \frac{\mu(\partial u/\partial y)}{(1/2)\rho U_0^2} = \frac{2U_1^2 r}{l}\left(\frac{\nu}{2\alpha U_0}\right)^{1/2}\left(\frac{\partial^2 f}{\partial\sigma^2}\right)_{\sigma=0} \tag{2.2}$$

Sphere

In the case of a sphere we put $l = r_0$, where r_0 is the radius of the solid boundary and r is the distance from the axis; whence, after a few transformations,

$$C_F = (2U_1^2 \sin\theta/\alpha^{1/2})\ (a/R^{1/2}) \tag{2.3}$$

where

$$a = (\partial^2 f/\partial\sigma^2)_{\sigma=0}, \quad R = 2r_0 U_0/\nu, \quad \alpha = \int_0^\theta \sin^2\theta U_1 d\theta$$

In the application which follows,

$$R = 157{,}000, \quad C_F = \frac{5.048 \times 10^{-3} a U_1^2 \sin\theta}{\alpha^{1/2}} \tag{2.4}$$

(3) The Method of Integration

The method of integration of Eq. (1.9) has been explained elsewhere;[5] however, to facilitate the reading of this paper, we give a very short account of it here.

To integrate Eq. (1.9), assume that

$$f(\sigma, \alpha) = \sum_{n=2}^{\infty} (a_n \sigma^n/n!) \tag{3.1}$$

where $f(\sigma, \alpha)$ satisfies the boundary conditions (1.10) at $\sigma = 0$ for an ordinary point. Substituting Eq. (3.1) in Eq. (1.9) we find the coefficients a_n in terms of $a_2 = a$, and its derivatives with respect to α.

Substituting then Eq. (3.1), instead of $f(\sigma, \alpha)$, in the left-hand side of Eq. (1.9), and in the right-hand side, we integrate it as a nonhomogeneous linear equation in $\partial^2 f/\partial\sigma^2$, and obtain

$$\left.\begin{aligned} \partial^2 f/\partial\sigma^2 &= \varphi(\sigma, \alpha)\exp\{-F(\sigma, \alpha)\} \\ \text{where} \qquad F(\sigma, \alpha) &= \int_0^\sigma f(\sigma, \alpha)d\sigma \end{aligned}\right\} \tag{3.2}$$

$\varphi(\sigma, \alpha)$ being a slowly varying function.

To find $\varphi(\sigma, \alpha)$, put

$$\varphi(\sigma, \alpha) = \sum_{n=0}^{\infty} (b_n \sigma^n/n!) \tag{3.3}$$

Combining Eqs. (3.1), (3.2), and (3.3) and comparing on both sides the terms in σ, we find the b_n's in terms of a and its derivatives with respect to α.

The unknown function a is found from the boundary condition (1.10),

$$\partial f/\partial\sigma = \int_0^\infty \varphi(\sigma, \alpha)\exp\{-F(\sigma, \alpha)\}d\sigma = 1 \tag{3.4}$$

To evaluate the integral, we put

$$F(\sigma, \alpha) = \tau \tag{3.5}$$

and invert Eq. (3.5) by expressing σ in terms of τ; whence

$$f'(\infty, \alpha) = 1 = \int_0^\infty e^{-\tau}\ \varphi(\sigma, \alpha)\frac{d\sigma}{d\tau}d\tau \tag{3.6}$$*

where

$$\varphi(\sigma, \alpha)\frac{d\sigma}{d\tau} = \tau^{-2/3}\sum_{m=0}^{\infty} d_m \tau^{m/3}$$

Integrating in gamma functions, we find finally the differential equation for a—namely,

$$\sum_{m=0}^{\infty} d_m \Gamma[(m+1)/3] = 1 \tag{3.7}$$

where Γ is the gamma function.

The expression (3.7) is divergent; it is summed by Euler's transformation. Only six terms are used in the calculations, and they are given here for the sake of convenience.[5]

$$\left.\begin{aligned} d_0 &= (1/3)(6a^2)^{1/3}, \quad d_1 = (5\lambda/18)(6/a)^{2/3}, \quad d_2 = -(3\lambda^2/8a^2) \\ d_3 &= (6/a)^{1/3}\{[(a - 28\lambda a + 28\alpha a')/45] + (91\lambda^3/648a^3)\} \\ d_4 &= (6/a)^{2/3}\{[(62\lambda - 75\lambda^2)/504] + (9\alpha\lambda'/28) - (\alpha\lambda a'/3a) - (935\lambda^4/15552a^4)\} \\ d_5 &= (3/a^2)\{[(-17 + 6\lambda)\lambda^2/280] - (3\alpha\lambda\lambda'/14) + (3\lambda^2\alpha a'/10a) + (7\lambda^5/128a^4)\} \end{aligned}\right\} \tag{3.8}$$

where primes denote differentiation with respect to α.

(4) Euler's Transformation

The aim of Euler's transformation is to eliminate a singularity which does not belong to the function itself but is introduced by the method of expansion. The singularity can be eliminated by using a suitable expansion.

Consider as an example

$$S(x) = [x/(1 + 4x)] = x - 4x^2 + 16x^3 - \ldots \tag{4.1}$$

for $x = 1$. The function $S(x)$ has no singularity on the positive axis; the expansion has, however, a singularity at $x = 1/4$, and it is divergent at $x = 1$. We could obviously partly eliminate this singularity by a differ-

* $F(\sigma)$ starts with σ^3, whence σ starts with $l^{1/3}$.

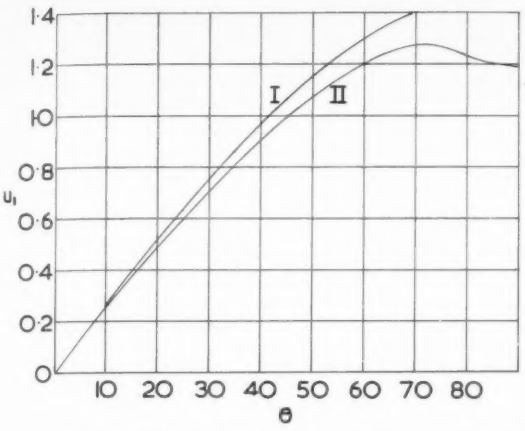

FIG. 1. U_1 against θ, I = inviscid flow; II = measured flow (Fage).

ent kind of expansion—for instance, by expanding in terms of

$$y = x/(1 + x)$$

This is Euler's transformation.

The calculations for the case $x = 1$ can be conveniently arranged in the following table:

$$\begin{array}{c} 1 - 4 + 16 - 64 \\ -3 + 12 - 48 \\ 9 - 36 \\ -27 \end{array}$$

where each term, starting from the second row, is an algebraic sum of two adjacent terms on the line above; whence

$$S(1) = \frac{1}{2} - \frac{3}{2^2} + \frac{9}{2^3} - \frac{24}{2^4} + \cdots$$

this expression is still divergent. Repeating the transformation, we obtain $S(1) = 1/5$.

In the case of an asymptotic expansion (semiconvergent), Euler applied the transformation in a different way.

We consider a certain number of terms (in our case, six), apply the transformation, and retain only the convergent terms. The transformation is then repeated on the remaining terms, and so on—this method will be used in our case.

Since we make use of a limited number of terms only, all terms, including zeros, have to be retained. We can start the transformation from the first, second, etc., terms; the best result is obtained (with an equal number of transformations) with a smallest last term and a best convergence. In any case, results corresponding to different combinations should differ only slightly.

(5) Preliminary Results

The above equations will now be applied to the case of flow past a sphere, measured by Fage.[4] The main dimensions are as follows: $d = 6$ in., the diameter of the sphere; $U_2 = 50$ ft./sec., the velocity of the air; and $R = dU_0/\nu = 157{,}000$, the Reynolds Number. Fage[4] measured the pressure and the friction. The minimum pressure is at $\theta \fallingdotseq 72.5°$, and the separation point is at $\theta = 83°$ from the forward stagnation point.

The functions U_1' and U_1'' change rapidly between the maximum of U_1 and the separation point; and the values of U_1'' can only be considered as approximate.

In Figs. 1 and 2 are plotted the velocity U_1 at the edge of the boundary layer and the curve of λ against θ. The difference in the shape of λ for a theoretical (inviscid) flow and a measured one should be noted.

For a theoretical flow λ increases monotonically—it has a maximum for a real flow—and the separation point is a short distance downstream of the maximum.

(6) Integration of the Equation—Friction

The method of integration of the nonlinear ordinary equation (3.7) is step by step. In reference 5, the corresponding values of a and a' were found by trial, but since this is rather a tedious procedure, we are giving here a short straightforward method of step-by-step integration.

Let the value of a be given at some point $\alpha = \alpha_0$; we have to find a', whence a is found for the next close value of α. The procedure is as follows.

(a) We substitute the value of a in Eq. (3.7), leaving a' indefinite; (b) the series being divergent, we apply Euler's transformation and, from the expression obtained, find a'; and (c) substituting the value of a' in the series from which it was obtained, we determine whether it is convergent—if only part of it is convergent we apply the transformation to the divergent terms to find a new value of a'—and so on.

An example of these calculations is given below. Consider

$$\theta = 65°, \quad \lambda = -0.250, \quad d\lambda/d\alpha = 1.32, \quad \alpha = 0.378, \quad a = 0.753$$

whence from Eq. (3.7) we find

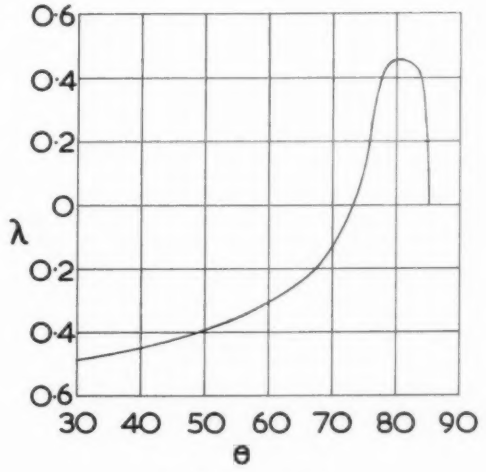

FIG. 2. λ against θ.

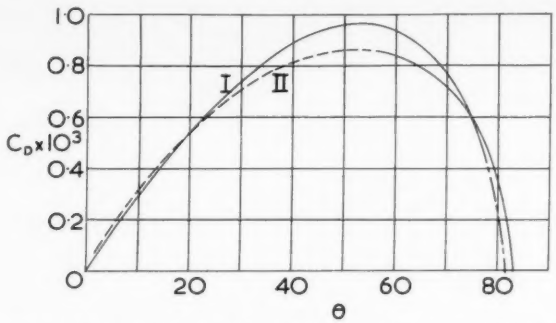

FIG. 3. C_D against θ: I, evaluated (Meksyn); II, - - - evaluated (Tomotika), —— measured (Fage).

$$f'(\infty, \alpha) = 1 = 1.3430 - 0.3751 - 0.0413 + (0.2296 + 0.4198a') + (0.4311 + 0.1507a') + (0.1188 + 0.0498a')$$

Applying Euler's transfo mation we obta n

$$1 = 0.6715 + 0.2420 + 0.0689 + (0.0202 + 0.0262a') + (0.0295 + 0.0572a') + (0.0566 + 0.0781a') = 1.0887 + 0.1615a' \quad (6.1)$$

whence $a' = -0.549$, and the last three terms become

$$0.0058 - 0.0019 + 0.0137$$

This is a moderately good result. One could apply the transformation to the last three terms; this, however, reduces considerably the magnitude of the terms of the equation, which makes it less reliable and does not improve the convergence. Then for $\theta = 70°$ and $\alpha = 0.472$, we find that

$$a = 0.753 - 0.094 \times 0.549 = 0.700$$

The general procedure is as follows. At the front part of the sphere up to $\lambda \sim -0.4$ ($\lambda = -0.5$ at $\theta = 0$) we can disregard the terms in Eq. (1.9) in curly brackets, and take the values of a from Hartree[6] of the abridged equation;[7] this has been done for θ up to $\theta = 50°$.

For $\theta = 55°$ we assume $a = 0.840$, which is slightly larger than the value $a = 0.825$ from Hartree's solution, since the curve of a against λ for the complete equation lies above the corresponding curve for Falkner and Skan's[7] equation. One has to bear in mind that the terms in Eq. (3.7) which determine a' [see Eq. (6.1)] are small at the front part of the body, and, thus, are liable to considerable errors. It is therefore more practical to take, at the start, tentative values of a, until the terms in the equation are sufficiently large.

The calculations were continued up to $\theta = 75°$ in intervals of five degrees; at $\theta = 76.5°$ the convergence became less satisfactory, as it is the general case near the separation. The calculations were not extended beyond this angle.

In Fig. 3 are plotted the coefficient of friction C_D [see Eq. (2.4)] against θ together with Tomotika's calculations[8] up to $\theta = 55°$ by the momentum method (for somewhat different pressure distribution), and Fage's[4] measured values from this angle to separation.

The separation point is evaluated by the method explained in Section (7); the curve from $\theta = 76.5°$ is drawn tentatively.

(7) Separation

The separation point is found by a different set of equations than (3.7) and (3.8), since $f(\sigma, \alpha)$ starts with the term σ^3.

The procedure was explained elsewhere;[5] here we give only the final expressions, for the sake of convenience. The position of the separation point is found from the equation

$$f'(\infty, \alpha) = \sum_{n=0}^{\infty} d_n \Gamma[(n+1)/4] = 1 \quad (7.1)$$

where

$$d_1 = (1/4)(24\lambda)^{1/2}$$
$$d_5 = (24/\lambda)^{1/2}\{[(4 - 15\lambda)\lambda + 10\,\alpha\lambda']/56\} \quad (7.2)$$

The remaining coefficients from d_0 to d_6 inclusive are equal to zero; d_7 can be taken as equal to zero.

The separation point is a short distance downstream of the maximum of λ; we try, accordingly, few points until we obtain $f'(\infty, \alpha) = 1$.

As an example of the calculations, consider the point

$$\theta = 83°, \quad \lambda = 0.450, \quad d\lambda/d\alpha = -7.00, \quad \alpha = 0.74$$

Substituting in Eq. (7.1) we find

$$f'(\infty, \alpha) \equiv 0 + 1.4558 + 0 + 0 + 0 - 6.1227 + 0 + 0 \equiv 0.3639 + 0.3639 + (0.2738 + 0.1820 - 0.0181 - 0.2187 - 0.4024)$$

Applying Euler's transformation to the terms in parentheses, we find

$$0.1369 + 0.1139 + 0.0820 + 0.0409 - 0.0071 \quad (7.3)$$

whence $f'(\infty) = 1.0944$.

The transformation was repeated starting from 0.2738 since this leads to a better convergence and a smaller last term than any other combination with the same number of terms. The last term in the Eq. (7.3) should be considered as equal to the algebraic sum of the two final terms; this is the procedure adopted by Euler, when two terms of very different magnitude follow each other.

The corresponding result for $\theta = 83.5°$ is $f'(\infty) = 1.0124$, where the final expression is

$$f'(\infty) = 0.3432 + 0.3432 + 0.1287 + 0.1072 + 0.0739 + 0.0287 - 0.0125 = 1.0124$$

The separation point is therefore at $\theta = 83.5°+$.

It may be noted that this method of finding the separation point cannot be used with the theoretical pressure distribution since λ in such cases increases monotonically.

(8) Discussion

The curve of friction obtained in the present calculations differs somewhat from Tomotika's results; this

(*Continued on page 664*)

Utilization of Experimental Results in Flutter Analysis†

ERIK MOLLÖ-CHRISTENSEN*

California Institute of Technology

SUMMARY

The general problem of utilization of test data in flutter analysis is discussed. Methods for evaluating changes in flutter characteristics due to changes in structural and aerodynamic parameters are given. The precision of information obtained from tests is considered and the resulting accuracy of the flutter prediction discussed.

SYMBOLS

x, ξ	= streamwise coordinate
y, η	= spanwise coordinate
$z(x, y)$	= wing deflection or complex amplitude of wing deflection
$F_{\mu\alpha}$	= complex amplitude of impressed force
$(1/2)\rho l^{-2}$	= dynamic pressure
M	= Mach Number
ω	= frequency
k	= $\omega b/U$ reduced frequency
b	= typical length dimension of wing
A	= domain in (x, y) plane occupied by wing plan form
$w(x, y)$	= complex amplitude of downwash at wing surface
$\mathfrak{D}(k, M)$	= downwash operator: $w(x, y) = \mathfrak{D}(k, M)\, z(x, y)$
$C(x, y; \xi, \eta)$	= flexibility influence function
$[\ ]$	= denotes a matrix
$\lvert\ \rvert$	= denotes a determinant
$m(x, y)$	= mass distribution of wing
$\varphi_\mu(x, y)$	= μth natural mode amplitude distribution
$\omega_{(\mu)}$	= μth natural frequency
$P(x, y; \xi, \eta; k, M)$	= aerodynamic influence function: the lift coefficient per unit area at (x, y) due to a unit downwash at (ξ, η) at reduced frequency k and Mach Number M
ζ_μ	= generalized amplitude of the μth mode: $\zeta_\mu = (1/M_\mu)\iint_A z(x, y)\varphi_\mu(x, y)dxdy$
M_μ	= generalized mass of μth mode
D	= flutter determinant
α	= subscript denoting test number
$[\diagdown H \diagdown]$	= diagonal matrix of integration weights
Q_μ	= generalized impressed force
$q_{\mu\nu}(k, M)$	= generalized aerodynamic coefficient

Received March 21, 1958.

† This work was done partly at the Massachusetts Institute of Technology under sponsorship of Boeing Airplane Company and partly at the National Advisory Committee for Aeronautics, Langley Field, during the summer of 1957, and was finished at the California Institute of Technology under a fellowship from the John Simon Guggenheim Memorial Foundation.

* Formerly, Senior Research Fellow. Now, Assistant Professor of Aeronautical Engineering, M.I.T.

The author wishes to acknowledge the helpful discussions he had with I. E. Garrick and C. E. Watkins of the NACA, M. J. Turner and J. Walsh of Boeing, and C. Y. Fung of the California Institute of Technology.

INTRODUCTION

THE TREATMENT of the flutter problem as a part of design practice usually involves both flutter analysis and flutter tests. The latter are necessary because of the doubtful validity of the flutter analysis, especially at transonic and supersonic Mach Numbers. The discrepancy between results of analysis and the results are often difficult to explain, especially when the test observations are limited to flutter speed, Mach Number and frequency.

It would be very desirable to establish a rational approach to the problem of the discrepancy between theory and experiment as it occurs in practice, and in the process develop methods for extracting more useful information from flutter tests. Molineaux has suggested a method for finding the aerodynamic forces on an oscillating wing from flutter tests,[1] and Martuccelli and the author have also outlined methods for this.[2]

This paper discusses the general problem of obtaining and utilizing experimental data in flutter analysis. Since the practicable number of tests is limited, one first has to find the most important parameters of the flutter problem, and then use tests to determine those important parameters which are known from theory or previous tests with the least precision.

The first step will be to write down the equations of motion.

(1) EQUATIONS OF MOTION OF A FLEXIBLE WING IN AN AIR STREAM

(1.1) Assumptions

Assume the structure of the wing to be linear. Also, for convenience, assume the wing to be thin, so that the wing deflections are principally normal to a plane (x, y) aligned with the remote airstream. It is then possible to use a flexibility influence function $C(x, y; \xi, \eta)$, which is the deflection at a point (x, y) caused by a unit concentrated load at a point (ξ, η). If one so wishes, one may consider the influence function to be modified according to reference 3, p. 109, so that rigid-body motions of the airplane are included.

As far as the aerodynamic forces are concerned, assume the airplane to be in steady flight, which includes a steady maneuver, and consider the oscillations about the steady conditions sufficiently small to allow the equations of motion of the unsteady air motion to be linearized. These equations will be perturbation

equations upon the generally nonuniform steady flow, and will usually not have constant coefficients. Transonic Mach Numbers are thus included, although the solution of the equations is not generally available, and one must, in order to obtain a flutter problem which can be solved, take recourse to brutal approximations.

Neglecting such mathematical difficulties, there must exist an integrodifferential operator which gives the local lift at a point (ξ, η) for a deflection amplitude distribution $z(r, s)$ for each Mach Number, M, and frequency of vibration ω. If $L(\xi, \eta)$ is the local lift, it is expressible in the form

$$L(\xi, \eta) = (1/2)\rho U^2 \iint_A P(\xi, \eta; r, s; k, M) \times \mathfrak{D}(k, M) z(r, s) dr\, ds \quad (1.1)$$

where A is the wing area, and $k = \omega b/U$ the reduced frequency. For two-dimensional supersonic flow over a flat plate, for example, the operator in Eq. (1.1) is[4]

$$L(\xi) = (1/2)\rho U^2(-4/\sqrt{M^2 - 1})\,(1/b^2) \times [(\partial/\partial\xi') + ik] \int_0^{\xi'} \exp[-ikM^2(\xi' - r') \div (M^2 - 1)] J_0[kM(\xi' - r')/(M^2 - 1)] \times [(\partial/\partial r') + ik]\, z(r')dr' \quad (1.2)$$

where b is the semi-chord, and ξ' and r' are obtained from ξ and r by division by b. $L(\xi)$ denotes the lift per unit span in this case.

(1.2) *Equations of Motion*

For a wing with a mass-distribution $m(x, y)$, oscillating harmonically in an airstream under the influence of impressed forces of complex amplitude $F(x, y)$, the equation of motion can be written

$$z(x, y) = \iint_A C(x, y; \xi, \eta)\, [\omega^2 m(\xi, \eta) z(\xi, \eta) + F(\xi, \eta) + (1/2)\rho U^2 \iint_A P(\xi, \eta; r, s; k, M) \times \mathfrak{D}(k, M) z(r, s) dr\, ds] d\xi\, d\eta \quad (1.3)$$

For the solution of this equation in all but a few simple or simplified cases,[5, 6] one must take recourse to numerical approximations. We shall consider two methods of approximation of the deflection amplitude distribution, $z(x, y)$—namely, (a) approximation by natural modes, and (b) approximation by discrete ordinates. This will in principle cover the forms of the equations resulting from any method of approximation.

(1.3) *Approximation by Natural Modes*

Let $\omega_{(\mu)}$ and $\varphi_\mu(x, y)$; $\mu = 1, 2, \ldots$ be, respectively, the sets of frequencies and amplitude distributions for free vibrations of the wing in a vacuum. Approximate $z(x, y)$ by a sum of the first N natural modes:

$$z(x, y) = \sum_{\mu=1}^{N} \zeta_\mu \varphi_\mu(x, y) \quad (1.4)$$

ζ_μ can be considered as a generalized coordinate of the wing motion. Substitution into Eq. (1.3) yields[3]

$$(\omega^2 - \omega_{(\mu)}{}^2) M_\mu \zeta_\mu = (1/2)\rho U^2 \sum_{\nu=1}^{N} \zeta_\nu q'_{\mu\nu}(k, M) + Q_\mu \quad (1.5)$$

Where M_μ is the generalized mass of the μth mode,

$$M_\mu = \iint_A m(\xi, \eta)\, [\varphi_\mu(\xi, \eta)]^2\, d\xi d\eta \quad (1.6)$$

Q_μ is the impressed generalized force,

$$Q_\mu = \iint_A F(x, y) \varphi_\mu(x, y) dx dy \quad (1.7)$$

and $q'_{\mu\nu}(k, M)$ are the components of the generalized aerodynamic coefficients, given by

$$q'_{\mu\nu}(k, M) = \iint_A \varphi_\mu(x, y) \left\{ \iint_A \times P(x, y; \xi, \eta)\, \mathfrak{D}(k, M)\, \varphi_\nu(\xi, \eta) d\xi\, d\eta \right\} dx\, dy \quad (1.8)$$

Flutter is found as the condition for Eq. (1.5) to have a nontrivial solution in the absence of impressed forces. This requires the principal determinant of Eq. (1.5) to vanish:

$$|\,[(\omega^2 - \omega_{(\mu)}{}^2) M_\mu \delta_{\mu\nu} + (1/2)\rho U^2 q'_{\mu\nu}(k, M)]\,| \quad (1.9)$$

where

$$\delta_{\mu\nu} = \begin{cases} 1 & \text{when } \mu = \nu \\ 0 & \text{when } \mu \pm \nu \end{cases}$$

The determinant is complex, and Eq. (1.9) can be solved to yield a pair of real characteristic values—for example, flutter frequency ω and air density ρ for a given Mach Number and atmospheric density and pressure profile, which relates U to ρ and M.

(1.4) *Approximation by Discrete Ordinates*

The integrals occurring in Eq. (1.3) can be approximated by a sum over discrete values of the integrand. The integral giving the aerodynamic coefficients in Eq. (1.3) is observed to involve a differentiation $\mathfrak{D}(k, M)\, z(x, y)$. Although a derivative can be evaluated from discrete ordinates, the result is usually inaccurate. Partial integration with respect to the streamwise coordinate may, if allowable, resolve this difficulty. Alternatively, since the boundary conditions of the wing deflection are known, one may express $z(x, y)$ as a linear combination of slopes at discrete points (x_μ, y_μ) as follows:

$$z(x, y) \simeq \sum_{\mu=1}^{N} \lambda_\mu(x, y)\, (\partial z/\partial x)_{\substack{x=x_\mu \\ y=y_\mu}} + \sigma_\mu(x, y)\, (\partial z/\partial y)_{\substack{x=x_\mu \\ y=y_\mu}} + f_1(x) + f_2(y) \quad (1.10)$$

The functions $\lambda_\mu(x, y)$ and $\sigma_\mu(x, y)$ can be found for discrete values of x and y from experiment, for example. Introducing Eq. (1.10) into Eq. (1.3), one obtains a formulation of the problem in terms of slopes of the wing surface. One may even go one step further and introduce second derivatives, which can be interpreted

as curvatures and twist, and, which can, incidentally, be measured using strain gages.[2] Using this, one may be able to obtain a good approximation to the elastic part of the problem and a reasonably sharp formulation of the boundary conditions of the aerodynamic problem using an approximation over a limited number of points on the wing.

Whether the coordinates chosen are deflections, slopes, or curvatures and twists at a set of discrete points, the integral in Eq. (1.3) will appear as a sum, and Eq. (1.3) takes on the form

$$z_\nu \simeq \sum_{\mu=1}^{N} H_\mu C_{\mu\nu}\{(m_\mu\omega^2 z_\nu + F_\mu) + (1/2)\rho U^2 \sum_{\gamma=1}^{N} q_{\mu\gamma}(k, M) z_\gamma\} \quad (1.11)$$

where H_μ is the integration weight for the μth coordinate and $q_{\mu\gamma}(k, M)$ are the modified aerodynamic coefficients. z_ν; $\nu = 1, 2, \ldots, N$ may stand for a deflection, slope, or curvature or twist, suitably arranged in sequence. The condition for flutter is again given by the vanishing of the principal determinant of Eq. (1.11), which is the determinant of the matrix

$$(-[1] + \omega^2[C]\,[\backprime m \backprime]\,[\backprime H \backprime] + (1/2)\rho U^2[C]\,[\backprime H \backprime]\,[q]) \quad (1.12)$$

(2) Sensitivity of the Flutter Point to Changes in the Parameters of the Problem

The flutter determinant is a function of all the parameters of the problem. Call the determinant D. The flutter equation is

$$D \equiv D(k, \rho, M, U, m_1, \ldots, m_N, q_{11}, \ldots, q_{NN}, C_{11}, \ldots, C_{NN}) = 0 \quad (2.1)$$

D is complex, while k, ρ, and M are real. In addition, the relation between density, velocity, and Mach Number is given by the structure of the atmosphere or the characteristics of the wind tunnel,

$$U = U(M, \rho) \quad (2.2)$$

The definition of reduced frequency k is

$$k = \omega b/U \quad (2.3)$$

Buxton and Minhinnick have considered the rate of change of flutter speed with parameter changes,[7] so have Baker[5] and Martuccelli and the author.[2] Following reference 2, one may observe that a change in a parameter P will change both the real and the imaginary parts of the flutter determinant. To bring the value of the flutter determinant back to zero, it will be necessary to change both velocity and reduced frequency, M and ρ being given by Eqs. (2.2) and (2.3).

Thus, one has, as the conditions for maintaining flutter.

$$\left.\begin{aligned} \mathrm{Re}(\Delta D) &= \Delta U\,\mathrm{Re}(\partial D/\partial U)_k + \Delta k\,\mathrm{Re}(\partial D/\partial k)_U + \mathrm{Re}[(\partial D/\partial P)\Delta P] = 0 \\ \mathrm{Im}(\Delta D) &= \Delta U\,\mathrm{Re}(\partial D/\partial U)_k + \Delta k\,\mathrm{Im}(\partial D/\partial k)_U + \mathrm{Im}[(\partial D/\partial P)\Delta P] = 0 \end{aligned}\right\} \quad (2.4)$$

Solving these equations for ΔU, one obtains

$$\left.\begin{aligned} \Delta U &= \frac{-\mathrm{Re}[(\partial D/\partial P)\Delta P]\mathrm{Im}(\partial D/\partial k)U - \mathrm{Im}[(\partial D/\partial P)\Delta P]\mathrm{Re}(\partial D/\partial k)_U}{\mathrm{Re}(\partial D/\partial U)_k \mathrm{Im}(\partial D/\partial k)_U - \mathrm{Re}(\partial D/\partial k)_U\,\mathrm{Im}(\partial D/\partial U)_k} \\ \text{or} \\ \Delta U &= -\mathrm{Im}\{\overline{[(\partial D/\partial P)\Delta P]}\,(\partial D/\partial k)_U\}/\mathrm{Im}\{\overline{(\partial D/\partial U)_k}\,(\partial D/\partial k)_U\} \end{aligned}\right\} \quad (2.5)$$

where the bar denotes the complex conjugate. It will be advantageous to perform these operations at constant Mach Number in an isothermal atmosphere, where U, M, ω, and k are very simply related. Let p and T be the pressure and temperature, respectively. The velocity of sound, a, is constant during the change, and one has

$$(1/2)\rho U^2 = \gamma/2pM; \quad U = Ma$$
$$\rho = p/RT; \quad \omega = kMa/b$$

and the indicated derivatives are

$$(\partial D/\partial U)_k = (\partial D/\partial M)_k\,(1/a) + \{\partial D/\partial[(1/2)\rho U^2]\}\,(p_1 M/RT) + (\partial D/\partial\omega)\,(k/b)$$

which is the change caused by a change in altitude, and

$$(\partial D/\partial k)_U = (\partial D/\partial k)_M + 2[\partial D/\partial(\omega^2)]\,(M^2a^2k/b^2)$$

which is the change caused by a change in frequency.

Since the derivative of a determinant with respect to one of its elements is simply the cofactor of the element, these derivatives should not prove too difficult to evaluate in practice. For the solution of a flutter problem on a high-speed computer, the elements of the flutter determinant will be stored in the memory, and there are standard methods for evaluating determinants, which only have to be modified by a program designed to skip selected terms. An alternative is, of course, to use numerical difference methods, involving repeated evaluation of the flutter determinant.

The changes in flutter conditions which have been considered do only involve terms of the first order. Higher order terms may be considered, although this will increase complexity tremendously.[8] Also, the method outlined above assumes that the flutter determinant is a continuous function of the problem parameters. Although this holds true in most cases, it is perhaps not necessarily so, for example, at Mach Numbers where a shock wave may jump from one place on the wing to another depending on boundary-layer characteristics or local separation.

In spite of this uncertainty, the method of analysis should have some practical value—specifically, it can be used to evaluate the effect of changes in wing properties on flutter characteristics. It can also be used to find the precision of a flutter prediction, when the accuracy of the structural and aerodynamic information used can be estimated. Another application would be to enable one to identify a "sensitive" flutter point, where a small change in a wing parameter causes a large change in flutter speed. While the flutter prediction in this case is entirely unreliable, one has the comfort of knowing that it will not take much redesign to change the flutter speed. If, on the other hand, the flutter speed proves very insensitive to parameter changes, the flutter analysis will be very reliable, but it will take a major effort to budge a flutter point if it occurs within the flight envelope of the aircraft. This state of affairs has been known in a less quantitative manner for some time, and can be used as an argument against radical innovations in a proven design.

We shall here indicate how the method discussed in this section can be utilized in connection with flutter tests. Before proceeding, we shall, however, outline a rough method of estimating changes in flutter speed due to parameter changes. This method will not work where one has a sensitive flutter point.

(2.1) *Rough Estimates of Flutter Point Changes Caused by Parameter Variations*

The method is based on iterative solution of the flutter problem. The change in flutter speed is estimated by an additional step in the iteration, using the changed parameter. The method will thus only work when the iteration is strongly convergent.

Eq. (1.3) can be solved by direction iteration[10] using the iteration formula

$$z^{(n)}(x, y) = \omega^{(n)^2} \iint_A C(x, y; \xi, \eta) m(\xi, \eta) z^{(n-1)}(\xi, \eta) d\xi d\eta + \left(\frac{1}{2}\rho U^2\right)^{(n)} \times \iint_A C(x, y; \xi, \eta) \iint_A P(\xi, \eta; r, s; M^{(n-1)}, k^{(n-1)}) \mathfrak{D}(M^{(n-1)}, k^{(n-1)}) z^{(n-1)}(r, s) dr\, ds\, d\xi\, d\eta =$$
$$\omega^{(n)^2}[A^{(n)}(x, y) + iB^{(n)}(x, y)] + \left(\frac{1}{2}\rho U^2\right)^{(n)} [C^{(n)}(x, y) + iD^{(n)}(x, y)] \quad \text{(say)} \qquad (2.6)$$

with the normalization

$$z^{(n)}(x_0, y_0) = 1 \qquad (2.7)$$

n refers to iteration number. From the normalization Eq. (2.7), one obtains:

$$[(1/2)\rho U^2]^{(n)} = B^{(n)}(x_0, y_0) \Big/ \begin{vmatrix} A^{(n)}(x_0, y_0) & B^{(n)}(x_0, y_0) \\ C^{(n)}(x_0, y_0) & D^{(n)}(x_0, y_0) \end{vmatrix} \qquad (2.8)$$

$$\omega^{(n)^2} = -\left[D^{(n)}(x_0, y_0)/B^{(n)}(x_0, y_0)\right] [(1/2)\rho U^2]^{(n)} \qquad (2.9)$$

When this iteration process has been carried to convergence within a previously specified limit, which is accomplished in N_1 steps, say, one has determined flutter dynamic pressure and frequency.

If one now wishes to find the effect of a small parameter change, one may use $z^{(N_1)}(x, y)$, $M^{(N_1)}$, and $k^{(N_1)}$ to carry out one more iteration, using a slightly changed value for the parameter in question, evaluating $A^{(N_1+1)}(x, y)$, $B^{(N_1+1)}(x, y)$, etc. and substituting into Eq. (2.8). This will yield the new flutter dynamic pressure and frequency approximately, provided the convergence during the previous iteration was satisfactory.

(3) Equation for a Set of Tests

Because we shall consider the results of experiments as tools for determining the properties of the wing and the values of the aerodynamic coefficients, we shall have to use data from many tests to determine all the coefficients in the flight vibration problem. It will, therefore, be useful to write the equation for a set of tests as a single equation. To become accustomed to the thought, let us first consider the equation for a set of simple static tests.

Consider the wing loaded with discrete loads $W_{\mu 1}$ at the points (x_μ, y_μ); $\mu = 1, 2, \ldots, N$ and observe the deflections $z_{\mu 1}$ at the same points. Repeat the experiment N times, and denote the loadings in the αth experiment by $W_{\mu\alpha}$ and the corresponding deflections by $z_{\mu\alpha}$.

The equation of the first test is

$$\begin{bmatrix} z_{11} \\ z_{21} \\ \cdot \\ \cdot \\ \cdot \\ z_{N1} \end{bmatrix} = \begin{bmatrix} C_{11} & C_{12} & \ldots & C_{1N} \\ C_{21} & C_{22} & \ldots & C_{2N} \\ & \cdot & \cdot & \\ & \cdot & \cdot & \\ & \cdot & \cdot & \\ C_{N1} & C_{N2} & \ldots & C_{NN} \end{bmatrix} \begin{bmatrix} W_{11} \\ W_{21} \\ \cdot \\ \cdot \\ \cdot \\ W_{N1} \end{bmatrix} \qquad (3.1)$$

The equation for the N tests can be written

$$\begin{bmatrix} z_{11} & \ldots & z_{1\alpha} & \ldots & z_{1N} \\ & \cdot & \cdot & \cdot & \\ z_{\mu 1} & \ldots & z_{\mu\alpha} & \ldots & z_{\mu N} \\ & \cdot & \cdot & \cdot & \\ z_{N1} & \ldots & z_{N\alpha} & \ldots & z_{NN} \end{bmatrix} = \begin{bmatrix} C_{11} & \ldots & C_{1N} \\ & \cdot & \\ & \cdot & \\ C_N & \ldots & C_{NN} \end{bmatrix} \begin{bmatrix} W_{11} & \ldots & W_{1\alpha} & \ldots & W_{1N} \\ & \cdot & \cdot & \cdot & \\ W_{\mu 1} & \ldots & W_{\mu\alpha} & \ldots & W_{\mu N} \\ & \cdot & \cdot & \cdot & \\ W_{N1} & \ldots & W_{N\alpha} & \ldots & W_{NN} \end{bmatrix} \qquad (3.2)$$

or, simply,

$$[z] = [C]\,[W] \qquad (3.3)$$

The matrix of flexibility influence coefficients $[C]$

can be found by post-multiplication of Eq. (3.2) by $[W]^{-1}$,

$$[C] = [z]\,[W]^{-1} \tag{3.4}$$

Routine tests currently performed in industry avoid this last step by arranging the test such that the loading matrix $[W]$ is a diagonal matrix. Whether this yields optimum accuracy in $[C]$ for a given accuracy of measurement of $[z]$ and $[W]$ will be discussed later.

For other types of experiments, one may write down the equation for a set of N experiments in similar ways.

(3.1) *Equation for a Set of Ground Vibration Sets*

For a set of ground vibration tests, the equations of motion can be written

$$[z_{\mu\alpha}] = [C]\,[\,m\,]\,[\,H\,]\,[z_{\mu\alpha}]\,[\,\omega_\alpha{}^2\,] + i[C]\,[d]\,[\,H\,]\,[z_{\mu\alpha}]\,[\,\omega_\alpha\,] + [C]\,[\,H\,]\,[F_{\mu\alpha}] \tag{3.5}$$

using discrete ordinates, where $[d]$ is a matrix of damping coefficients, and α refers to the test number. Similarly, in terms of generalized coordinates, from Eq. (1.5), one may write:

$$[\,M\,]\,[\zeta_{\mu\alpha}]\,[\,\omega_\alpha{}^2\,] + i[d']\,[\zeta_{\mu\alpha}]\,[\,\omega_\alpha\,] - [\,M\,]\,[\,\omega_{(\mu)}{}^2\,]\,[\zeta_{\mu\alpha}] = [Q_{\mu\alpha}] \tag{3.6}$$

where $Q_{\mu\alpha}$ is the μth generalized impressed force in the αth test, and $\omega_{(\mu)}$ is the natural frequency of the μth mode, while ω_α (no parentheses around subscript) is the frequency in the αth test. $[d']$ is a matrix of generalized damping coefficients.

(3.2) *Equation for a Set of Flight Vibration Tests*

For sets of flight vibration tests the equations become more complicated unless one restricts the tests somehow. For example, one may consider tests carried out at constant Mach Number and reduced frequency, to obtain, using discrete ordinates,

$$[z_{\mu\alpha}] = [C]\,[\,m\,]\,[\,H\,]\,[z_{\mu\alpha}]\,[\,\omega_\alpha{}^2\,] + [C]\,[q(k, M)]\,[\,H\,]\,[z_{\mu\alpha}]\left[\,\left(\frac{1}{2}\rho U^2\right)_\alpha\,\right] + [C]\,[F_{\mu\alpha}] \tag{3.7}$$

where structural damping has been neglected.

Formulating the flight vibration problem in terms of generalized coordinates [Eq. (1.5)] one obtains

$$[\,M\,]\,[\zeta_{\mu\alpha}]\,[\,\omega_\alpha{}^2\,] - [\,M\,]\,[\,\omega_{(\mu)}{}^2\,][\zeta_{\mu\alpha}] = [Q_{\mu\alpha}] + [q'(k, M)]\,[\zeta_{\mu\alpha}]\left[\,\left(\frac{1}{2}\rho U^2\right)_\alpha\,\right] \tag{3.8}$$

(3.3) *Use of the Equations for Sets of Tests*

The equations for a set of tests can be used to extract meaningful information from experiments beyond the usual observation that the test results do not agree with theory. Static tests have, of course, been used to obtain the flexibility influence coefficients for some time. One may, however, reason that the mass-distribution of a wing is known very accurately, so that perhaps a ground vibration test would yield a more accurate matrix of influence coefficient than will a static test, since accelerometers can be used, rather than some reference plane which unavoidably will deflect. Other reasons for such a preference will be given later.

One can also see how a set of model flutter tests or a flight vibration test can be used for the determination of the aerodynamic matrix $[q_{\mu\nu}(k, M)]$. One may conduct flight flutter tests and model flutter tests for such purposes, rather than interpreting test results using extrapolations based on generalizations from special cases. It will first be necessary to consider methods for estimating the precision of test results. Choose a static test as a first example.

(4) Precision of a Static Test

Consider a set of static tests for the purpose of determining the matrix of stiffness influence coefficients $[C]$. Assume that the loadings $W_{\mu\alpha}$ are known exactly, and that the measured deflections $z_{\mu\alpha}$ have the mean square errors $\sigma_z{}^2$. It is, of course, open to question whether assuming that the errors are independent of the magnitude of the measured deflections is realistic, but the analysis will be simpler with this assumption.

From Eq. (3.4) one obtains

$$[C] = [z]\,[W]^{-1} \tag{4.1}$$

or, written out,

$$C_{ij} = \sum_{\nu=1}^{N} z_{i\nu}\,W_{\nu j}{}^{-1} = \sum_{\nu=1}^{N} z_{i\nu}\,(\overline{W_{j\nu}}/|W|) \tag{4.2}$$

where $\overline{W_{j\nu}}$ is the cofactor of $W_{\nu j}$ and $|W|$ is the determinant of the loading matrix $[W]$.

The mean square deviation $\sigma_{C_{ij}}$ of C_{ij} is given by[11]

$$\sigma_{C_{ij}}{}^2 = \sum_{\nu=1}^{N} (\overline{W_{j\nu}}/|W|)^2\,\sigma_z{}^2 = (\sigma_z{}^2/|W|^2)\sum_{\nu=1}^{N} \overline{W_{j\nu}}{}^2 \tag{4.3}$$

One observes that, in order to minimize the error, one should make $|W|$ large and $\sum_{\nu=1}^{N} \overline{W_{j\nu}}{}^2$ small for all j, or, stated differently, $[W]^{-1}$ should be small. The loadings are limited to the elastic range, therefore one must seek other means to minimize the errors in $[C]$. The customary way is to make the loading matrix a diagonal matrix. Setting all the loads equal to unity, one obtains

$$\sigma_{C_{ij}}{}^2 = \sigma_z{}^2 \tag{4.4}$$

as one should expect.

If one chooses to express the equations of motion of the wing in terms or local slopes or curvatures and twists, the dispersion of errors in the appropriate influence matrix will be given by equations similar to Eq. (4.4).

(4.1) *Errors in Mass-Distribution and Damping as Obtained From Ground Vibration Tests*

The purpose of ground vibration tests is usually to determine the natural modes of the aircraft in free

flight. Why this should be the purpose of the tests is not quite clear. It is impossible to suspend the aircraft such as to simulate free flight conditions, and the free vibration modes during the test are, therefore, different from the vibration modes in free flight. Also, one does not need to know the vibration modes in free flight to perform a flutter analysis. If a ground vibration test shall be useful beyond giving an indication as to which extent analysis is unreliable, it is necessary to consider it as a means for finding wing properties. If one is confident that one knows the mass distribution, one can compute the stiffness from the test results.

On the other hand, if one is not confident about the numerical approximation involved in formulating the flutter problem in a finite number of terms, one may determine the constants in the equation of motion from tests, rather than analysis, and thus eliminate, within experimental accuracy, the remainder terms in the approximation as far as their effect on a set of specified vibration modes is concerned. In such tests, it will be necessary to measure all the forces on the wing or the airplane, including forces exerted by the supports.

Consider the equation of a set of ground vibration tests, Eq. (3.5). Measure $z_{\mu\alpha}$, ω_α and the complex amplitude of the impressed forces $F_{\mu\alpha}$, which includes forces exerted by the support. Assume that the matrix of flexibility influence coefficients [C] is known.

Excite the structure as it is in one of its natural modes for each test by seeking a frequency where the amplitude is large and the phase angle between exciting force and motion is 90°.

The deflection amplitudes will then be in phase, and we shall consider them real. From Eq. (3.5) one then obtains

$$[\diagdown m \diagup] = [C]^{-1}\,[z_{\mu\alpha}]\,[\diagdown \omega_\alpha{}^2 \diagup] \times [z_{\mu\alpha}]^{-1}\,[\diagdown H \diagup]^{-1} \quad (4.5)$$

for the real part of Eq. (3.5) and, for the imaginary part,

$$[d] = -\,[\diagdown H \diagup]\,[F_{\mu\alpha}]\,[\diagdown \omega_\alpha \diagup]^{-1} \times [z_{\mu\alpha}]^{-1}\,[\diagdown H \diagup]^{-1} \quad (4.6)$$

The mass matrix $[m]$ should, strictly speaking, be diagonal, and the magnitude of the off-diagonal terms as found from Eq. (4.5) gives an indication of the size of the mass-couplings which have been neglected.

The precision of the mass matrix $[m]$ can be seen to depend upon the precision of $[C]^{-1}$ and of $[z_{\mu\alpha}]^{-1}$. The errors in $[C]^{-1}$ are usually large, since the determinant of $[C]$ is small for all practical wings. However, the matrices $[m]$ and $[C]$ only occur in the combination $[C]\,[m]$ in the equations of motion, so it is more realistic to examine the errors in this matrix. From Eq. (4.5),

$$[C]\,[\diagdown m \diagup] = [z_{\mu\alpha}]\,[\diagdown \omega_\alpha{}^2 \diagup]\,[z_{\mu\alpha}]^{-1}\,[\diagdown H \diagup]^{-1} \quad (4.7)$$

To find the first-order error, assuming the frequencies to be exactly determined by the experiment, one differentiates Eq. (4.7) to obtain

$$d\,([C]\,[\diagdown m \diagup]) = (d[z_{\mu\alpha}])\,[\diagdown \omega_\alpha{}^2 \diagup]^{-1} \times [z_{\mu\alpha}]^{-1}\,[\diagdown H \diagup]^{-1} + [z_{\mu\alpha}]\,[\diagdown \omega_\alpha{}^2 \diagup]^{-1} \times d([z_{\mu\alpha}]^{-1})\,[\diagdown H \diagup]^{-1} \quad (4.8)$$

One observes that if $[z_{\mu\alpha}]^{-1}$ is very large, the errors will be large. Indeed, if two of the columns of $[z_{\mu\alpha}]$ are very similar, $[z_{\mu\alpha}]^{-1}$ may be extremely large. Thus, if the structure has two modes of vibration closely similar, only one of them should be included in Eq. (4.7). If this is done, excessive errors will be avoided, since we have specified a test procedure which then yields an orthogonal matrix $[z_{\mu\alpha}]$, which cannot be singular.

The same remarks apply to the determination of $[d]$; also, it may be remarked that the accuracy in $[d]$ depends directly upon the precision with which the impressed forces are measured.

An alternative use of the data from a set of ground vibration tests is to determine the matrix of influence coefficients when the mass distribution is known.

(4.2) *Determination of the Structural Properties of the Wing From Ground Vibration Tests*

Perform the same set of ground vibration tests as specified in Section (3.1) above. When the mass distribution $[\diagdown m \diagup]$ is known, the real part of Eq. (3.5) can be solved for $[C]$, to yield

$$[C] = [z_{\mu\alpha}][\diagdown \omega_\alpha{}^2 \diagup]^{-1}\,[z_{\mu\alpha}]^{-1}\,[\diagdown H \diagup]^{-1}\,[\diagdown m \diagup]^{-1} \quad (4.9)$$

Again, the errors in $[C]$ behave as discussed in the previous section, but for the fact that they are multiplied by $[\diagdown m \diagup]^{-1}$. $[\diagdown m \diagup]$ being a diagonal or almost diagonal matrix, this will not lead to difficulties.

Solving Eq. (4.9) for $[d]$ one obtains Eq. (4.6), as before, $[C]$ now being given by Eq. (4.9).

The reader is again reminded that $[z_{\mu\alpha}]$ may be a slope or strain as well as a linear deflection with $[C]$, $[m]$ and $[d]$ being interpreted as the appropriate generalized wing properties.

(5) Use of Flight Vibration Tests and Flutter Model Tests for Determination of Aerodynamic Forces

The viewpoint adopted above can without modification be used for analysis of flight vibration tests or model flutter tests. For a set of N such tests, all performed at the same Mach Number and reduced frequency, Eq. (3.7) holds. It can be solved for $[q_{\mu\nu}(k, M)]$ to yield

$$[q_{\mu\nu}(k, M)] = [C]^{-1}\,([z_{\mu\alpha}] - [C]\,[F_{\mu\alpha}] - [C]\,[\diagdown m \diagup] \times [\diagdown H \diagup]\,[z_{\mu\alpha}]\,[\diagdown \omega_\alpha{}^2 \diagup])\left[\diagdown \left(\frac{1}{2}\rho U^2\right)_\alpha \diagup\right]^{-1} \times [z_{\mu\alpha}]^{-1}\,[\diagdown H \diagup]^{-1} \quad (5.1)$$

where $[z_{\mu\alpha}]$, $[\diagdown \omega_\alpha{}^2 \diagup]$, $\left[\diagdown \left(\frac{1}{2}\rho U^2\right)_\alpha \diagup\right]$, and $[F_{\mu\alpha}]$ are measured. For a flutter test, $F_{\mu\alpha} = 0$, otherwise the equation remains the same. In terms of natural mode amplitudes, Eq. (1.9) can be solved similarly for the generalized aerodynamic coefficient $q'_{\mu\nu}(k, M)$ to yield

$$[q'_{\mu\nu}(k, M)] = \{[\diagdown M \diagup][\zeta_{\mu\alpha}][\diagdown \omega_\alpha^2 \diagup] - [\diagdown \omega_{(\mu)}^2 \diagup][\zeta_{\mu\alpha}]) - [Q_{\mu\alpha}]\}\left[\diagdown\left(\frac{1}{2}\rho U^2\right)_\alpha \diagup\right]^{-1}[\zeta_{\mu\alpha}]^{-1} \quad (5.2)$$

We proceed to discuss possible approximations for the aerodynamic coefficients, after which we shall return to the question of precision of aerodynamic coefficients and of flutter prediction.

(5.1) *Approximations to Aerodynamic Coefficients*

It will be inconvenient, if possible at all, to perform the entire set of flight vibration tests or flutter model tests at constant reduced frequency and Mach Number. It is therefore desirable to introduce approximations for the coefficients dependent upon reduced frequency and Mach Number. Realizing that, for high-speed aircraft with thin wings, the reduced flutter frequency is much smaller than unity, one may use an expansion in powers of k. Additionally, one may use some suitable approximation for the variation of the aerodynamic coefficients with Mach Number. For supersonic speeds, it is possible to use powers of $(M^2 - 1)^{1/2}$, while for transonic flow, powers of $(M - 1)$ will be more suitable. For supersonic flow, the following approximation is suggested:

$$q_{\mu\nu}(k, M) = (1/\sqrt{M^2 - 1})\{a_{\mu\nu} + b_{\mu\nu}k + (d_{\mu\nu} + e_{\mu\nu}k)(1/M^2) + \ldots\} \quad (5.3)$$

while, for transonic flow,

$$q_{\mu\nu}(k, M) = (\bar{a}_{\mu\nu} + \bar{b}_{\mu\nu}k)(M - 1) + (\bar{c}_{\mu\nu} + \bar{d}_{\mu\nu}k)(M^2 - 1)^2 + \ldots \quad (5.4)$$

where the $a_{\mu\nu}$, $b_{\mu\nu}$, etc., are constants. Better approximations may, of course, suggest themselves. For the coefficients for some of the higher order terms in the expansions, theory may be entirely adequate, while, for the evaluation of terms which do not contain k, steady tests on deformed wings can be used. The remainder of the coefficients can then be found from flight vibration or flutter model tests. The relative importance of the aerodynamic coefficients can be found using the expressions given in Section (2), and the unimportant coefficients can be guessed at, using available linearized aerodynamic theory.

After all the aerodynamic coefficients have been obtained by experiment, guess, or theory, the flutter problem can be solved, being careful of not exceeding the limits of validity of the approximations used for $q_{\mu\nu}(k, M)$.

(5.2) *Accuracy of the Aerodynamic Coefficients*

Differentiating Eq. (5.1), one obtains the first-order change in the $q_{\mu\nu}(k, M)$ due to first-order changes in the terms on the right:

$$d[q_{\mu\nu}(k, M)] = [dq_{\mu\nu}(k, M)] = d[C]^{-1}([z_{\mu\alpha}] - [C][F_{\mu\alpha}] - [C][\diagdown m \diagup][\diagdown H \diagup][z_{\mu\alpha}][\diagdown \omega_\alpha^2 \diagup]) \times \left[\diagdown\left(\frac{1}{2}\rho U^2\right)_\alpha \diagup\right][z_{\mu\alpha}]^{-1}[\diagdown H \diagup]^{-1}[C]^{-1}([dz_{\mu\alpha}] - [dC][F_{\mu\alpha}] - [C][dF_{\mu\alpha}] - [C][\diagdown m \diagup][\diagdown H \diagup][dz_{\mu\alpha}][\diagdown \omega_\alpha^2 \diagup] - [dC][\diagdown m \diagup][\diagdown H \diagup][z_{\mu\alpha}][\diagdown \omega_\alpha^2 \diagup] - [C][\diagdown drn \diagup][\diagdown H \diagup][z_{\mu\alpha}][\diagdown \omega_\alpha^2 \diagup])\left[\diagdown\left(\frac{1}{2}\rho U^2\right)_\alpha \diagup\right]^{-1}[z_{\mu\alpha}]^{-1}[\diagdown H \diagup]^{-1} + [C]^{-1}([z_{\mu\alpha}] - [C][F_{\mu\alpha}] - [C][\diagdown m \diagup][\diagdown H \diagup][z_{\mu\alpha}][\diagdown w_\alpha^2 \diagup])\left[\diagdown\left(\frac{1}{2}\rho U^2\right)_\alpha \diagup\right]^{-1} d[z_{\mu\alpha}]^{-1}[\diagdown H \diagup]^{-1} \quad (5.5)$$

where it has been assumed that $\left[\diagdown\left(\frac{1}{2}\rho U^2\right)_\alpha \diagup\right]$, $[\diagdown \omega_\alpha^2 \diagup]$, and $[\diagdown H \diagup]$ are known exactly. To ensure that $d[z_{\mu\alpha}{}^4]^{-1}$ is small, the tests must be arranged such that $[z_{\mu\alpha}]$ is far from being singular—i.e., that the determinant of $[z_{\mu\alpha}]$ is large—which can be done by exciting the natural flight modes. An example of what otherwise might happen is given in the Appendix. Also, it is obvious that the errors in $[z_{\mu\alpha}]$ and $[\diagdown m \diagup]$ should be made small. The error in $[q_{\mu\nu}(k, M)]$ will be small when the dynamic pressures are high, which leads to the trivial conclusion that the most reliable flight flutter test is performed at flutter. The most bothersome term in Eq. (5.5) is, however, the first term on the right-hand side involving $d[C]^{-1}$. As will be shown in the Appendix, this term is large for most structures, unless the problem is formulated in terms of strains instead of deflections.

There is still hope, however, since the aerodynamic coefficients only appear in the flutter equation in combination with the flexibility influence coefficients $[C]$. The term whose precision is important is, therefore, not $[q_{\mu\nu}(k, M)]$ but $[C][q_{\mu\nu}(k, M)]$. The first-order error of this term is

$$d\{[C][q_{\mu\nu}(k, M)]\} = ([dz_{\mu\alpha}] - [dC][F_{\mu\alpha}] - [C][dF_{\mu\alpha}] - [dC][\diagdown m \diagup][\diagdown H \diagup][z_{\mu\alpha}][\diagdown \omega_\alpha^2 \diagup] - [C][\diagdown dm \diagup][\diagdown H \diagup][z_{\mu\alpha}][\diagdown \omega_\alpha^2 \diagup] - [C][\diagdown m \diagup][\diagdown H \diagup][dz_{\mu\alpha}][\diagdown \omega_\alpha^2 \diagup])\left[\diagdown\left(\frac{1}{2}\rho U^2\right)_\alpha \diagup\right]^{-1}[z_{\mu\alpha}]^{-1}[\diagdown H \diagup]^{-1} + ([z_{\mu\alpha}] - [C][F_{\mu\alpha}] - [C][\diagdown m \diagup][\diagdown H \diagup][z_{\mu\alpha}][\diagdown \omega_\alpha^2 \diagup])\left[\diagdown\left(\frac{1}{2}\rho U^2\right)_\alpha \diagup\right] d[z_{\mu\alpha}]^{-1}[\diagdown H \diagup]^{-1} \quad (5.6)$$

The important term in this relation is $d[z_{\mu\alpha}]^{-1}$, which, as has been mentioned before, can be minimized by testing at flight vibration modes, which will yield an almost orthogonal matrix $[z_{\mu\alpha}]$.

At times, one may want to use the aerodynamic coefficients obtained from tests on one wing to carry out flutter analysis on another wing of the same plan form, but with different structural properties. Denoting

the matrix of flexibility influence coefficients of the latter wing by $[C']$, the expression that occurs in the flutter equation is

$$[C'][q_{\mu\nu}(k, M)] = [C'][C]^{-1}([z_{\mu\alpha}] - [C][F_{\mu\alpha}] - [C][\diagdown m \diagup][\diagdown H \diagup][z_{\nu\alpha}][\diagdown \omega_\alpha{}^2 \diagup]) \times \left[\diagdown \left(\frac{1}{2}\rho U^2\right)_\alpha \diagup\right]^{-1} [z_{\mu\alpha}]^{-1}[\diagdown H \diagup]^{-1} \quad (5.7)$$

If $[C']$ and $[C]$ are not very different, $[C'][C]$ will not differ much from the unit matrix, and the error will not be excessive. If, however, the wings are very different, the error in $[C'][q_{\mu\nu}]$ may become very large. For such cases, it will definitely be necessary to formulate the problem in terms of strains instead of deflections, since the strain influence matrices are usually further from being singular than are the deflection influence matrices.

(6) Aerodynamic Coefficients Obtained From Pressure Measurement

As an alternative to obtaining the aerodynamic coefficients inferentially from deflection and or strain measurements, one may consider measuring pressure differences directly on oscillating wings. When doing so, the wing deflections must also be measured, otherwise the boundary conditions under which the measured pressures occur would not be known. Also, the lift distribution is usually a more complicated function than the wing deflections and the wing strains, especially in transonic flow. One must, therefore, use a large number of pressure pickups to obtain an adequate description of the pressure distributions. Also, in the author's experience with such measurements, shock waves seem to have a perverse affinity for the spaces between the pressure transducers.

The wing strains, on the other hand, are given by weighted repeated integrals of the lift distribution, as are the deflections, and therefore much more smoothly distributed.

Lift distribution measurements on oscillating flexible wings will therefore require much more effort than the aerodynamic admittance measurements described above, and should only be considered when one is mainly interested in throwing light on unsteady aerodynamics, and not for routine practical measurements. Further developments of traversing probe methods may modify this conclusion.[12]

(7) Conclusion

Although most flight flutter testing will continue to be based on the generalization of trends found for particular cases, it may be possible to use the viewpoint of this paper as a guide to explain the cases where accustomed methods fail.

While no radical changes in test methods have been proposed, it is suggested that the purpose of the tests be viewed in another light, especially as far as ground vibration tests and flutter model tests are concerned, in the sense that tests and analysis be considered together, and not as separate approaches to the flutter problem. The use, if any, of the methods outlined in this paper is best left to practising engineers.

Evaluation of the methods which have been outlined can only be obtained by experiment, and such experiments are being planned, contingent upon the availability of funds.

Appendix—Illustration of the Effect of Errors in a Matrix Upon Errors in Its Inverse

As an example, consider the matrix of influence coefficients of a uniform cantilever beam under transverse loading, using three loading points—namely, at $l/3$, $2l/3$, and l—l being the length of the beam.

The matrix of deflection influence coefficients is, but for a constant,

$$\begin{bmatrix} C_{11} & C_{12} & C_{13} \\ C_{21} & C_{22} & C_{23} \\ C_{31} & C_{32} & C_{33} \end{bmatrix} = \begin{bmatrix} 2 & 5 & 8 \\ 5 & 16 & 28 \\ 8 & 28 & 54 \end{bmatrix}$$

its inverse, $[K] = [C]^{-1}$ is

$$\begin{bmatrix} K_{11} & K_{12} & K_{13} \\ K_{21} & K_{22} & K_{23} \\ K_{31} & K_{32} & K_{33} \end{bmatrix} = \begin{bmatrix} 3.077 & -1.768 & 0.462 \\ -1.768 & 1.692 & -0.615 \\ 0.462 & -0.615 & 0.269 \end{bmatrix}$$

where K_{ij} is given by[13]

$$K_{ij} = \overline{C'_{ij}}/|C| \quad \text{(A-1)}$$

where $\overline{C'_{ij}}$ is the cofactor of C_{ij} in the transposed matrix $[C_{ij}]'$. Differentiating Eq. (A-1) with respect to

Table 1
Table of $(C_{\mu\nu}/K_{ij})$ $(\partial K_{ij}/\partial C_{\mu\nu})$

		$\nu = 1$			$\nu = 2$			$\nu = 3$		
	$i \downarrow$	$j = 1$	$j = 2$	$j = 3$	$j = 1$	$j = 2$	$j = 3$	$j = 1$	$j = 2$	$j = 3$
$\mu = 1$	1	6.154	−6.154	−6.154	8.846	−8.846	8.846	−3.692	−3.697	3.692
	2	−6.154	−10.413	−2.654	2.977	18.496	6.346	1.177	−6.266	−3.692
	3	−6.154	−2.654	−1.582	−2.828	8.846	5.275	6.974	−1.192	−3.692
$\mu = 2$	1	8.846	2.977	−2.820	−45.815	−56.615	−45.949	7.431	12.361	17.231
	2	−8.846	18.496	8.846	−56.615	−27.077	−56.615	17.231	36.028	−17.231
	3	8.846	6.346	−5.275	−45.949	−56.615	−52.044	5.564	13.731	17.231
$\mu = 3$	1	−3.692	1.177	6.974	7.431	17.231	5.564	−3.739	−8.669	−14.538
	2	−3.692	−6.266	−1.192	12.361	36.028	13.731	−8.669	−27.944	−15.538
	3	3.692	−3.692	−3.692	17.231	−17.231	17.231	−14.538	−14.538	14.538

$C_{\mu\nu}$, one obtains

$$\frac{C_{\mu\nu}}{K_{ij}}\frac{\partial K_{ij}}{\partial C_{\mu\nu}} = \frac{C_{\mu\nu}}{K_{ij}}\left(\frac{(1-\delta_{i\mu}\,\delta_{j\nu})\overline{C'_{ij\mu\nu}}}{|C|} - \frac{\overline{C'_{ij}}\,\overline{C_{\mu\nu}}}{|C|^2}\right) \quad \text{(A-2)}$$

where $\overline{C'_{ij\mu\nu}}$ denotes the cofactor of the (μ, ν) term in the cofactor of C_{ij} in the transpose of $[C]$.

Eq. (A-2) gives the first-order relative change in $[K_{ij}]$, $(\Delta K_{ij})/K_{ij}$ due to a relative change in $C_{\mu\nu}$ of $(\Delta C_{\mu\nu})/C_{\mu\nu}$. Table 1 shows these first-order changes.

The numbers in Table 1 can be thought of at the matrix of percentage errors in $[K]$ for a 1 per cent error in one of the terms in [C]. The reason why the errors are so large is that the determinant of $[C]$ is small, the columns being almost simple multiples. Physically speaking, the deflection curves under concentrated loads are not really very different. The situation is a little better for most airplane wings, since their stiffness tapers off toward the tips.

The inverse of the numbers in Table 1 are the first-order relative sensitivity of the terms in $[C]$ to relative changes in $[K]$. These sensitivities are small. One must conclude that a given matrix of flexibility influence coefficients does not specify the actual structure very precisely, while $[K]$ seems to do so.

When trying to evaluate $[C]$ theoretically, one may obtain the most precise values by evaluating $[K]$ and then inverting it.

References

[1] Molineaux, W. G., *The Determination of Aerodynamic Coefficients from Flutter Test Data*, unpublished Ministry of Supply Report, United Kingdom, 1956.

[2] Mollö-Christensen, E., and Martucelli, J. R., *A Study of the Feasibility of Experimental Determination of Aerodynamic Forces for use in Flutter Calculation*, M.I.T. Aeroelastic and Structures Research Lab., Technical Reports 66-1, 66-2, 66-3, June, 1957.

[3] Bisplinghoff, R. L., Ashley, H., and Halfman, R. L., *Aeroelasticity*, Addison Wesley, Cambridge, 1955.

[4] Garrick, I. E., and Rubinow, S. I., *Flutter and Oscillating Air-Force Calculations for an Airfoil in Two-Dimensional Supersonic Flow*, NACA Report 846, 1946.

[5] Ashley, H., and Zartarian, G., *Piston Theory—A New Aerodynamic Tool for the Aeroelastician*, Journal of the Aeronautical Sciences, Vol. 23, No. 12, pp. 1109–1118, December, 1956.

[6] Goland, M., *The Flutter of a Uniform Cantilever Wing*, Journal of Applied Mechanics, Vol. 12, No. 4, December, 1945.

[7] Buxton, G. H. L., and Minhinnick, I. T., *Expressions for the Rates of Change of Critical Flutter Speeds and Frequencies with Inertial, Aerodynamic and Elastic Coefficients*, British ARC R&M 2444, September, 1945.

[8] Baker, R. C., *Effect of Errors and Changes in System Parameters on the Flutter Point*, S.M. Thesis, M.I.T., 1956.

[9] Crout, P. D., *A Short Method of Evaluating Determinants and Solving Systems of Linear Equations with Real or Complex Coefficients*, Trans. A.I.E.E., Vol. 60, pp. 1235–1240, 1941.

[10] Wielandt, H., *Solution of a General Linear Eigenvalue Problem*, Aerodyn. Versuchsanstalt, Göttingen, AVA B 44/J/19.

[11] Cramer, H., *Mathematical Methods of Statistics*, p. 213, Princeton University Press, 1954.

[12] Lewis, S. D., and Mollö-Christensen, E., *Measurement of Pressure Distributions on Oscillating Wings in Supersonic Flow. Part One, Experimental Methods*, M.I.T. Aeroelastic and Structures Research Lab. Report 57-1, December, 1955.

[13] Frazer, R. A., Duncan, W. J., and Collar, A. R., *Elementary Matrices*, Cambridge University Press, Cambridge, England, 1950.

[14] Van de Vooren, A. I., and Hofsommer, D. J., *Ternary Wing Bending-Aileron-Tab Flutter*, NLL (Netherlands) Report F 86, May, 1951.

Thermal Stress in Curved Beams (*Continued from page 630*)

Here one may take

$$\nabla^2 = (1/r)\,(d/dr)\,[r\,(d/dr)] \quad \text{(11a)}$$

Integration of Eq. (11) gives:

$$\phi = A_1 \ln(r/a) + A_2(r/a)^2 \ln(r/a) + A_3(r/a)^2 - E\alpha \int_a^r \left[(1/r)\int_a^r Tr\,dr\right] dr \quad (12)$$

provided that a constant term which produces no stress is omitted. The boundary conditions

$$\tau_{r\theta} = -(\partial/\partial r)\,[(1/r)\,(\partial\phi/\partial\theta)] = 0 \quad \text{at } r = a, b \quad (13)$$

are automatically satisfied by this expression for ϕ. The constants A_1, A_2, and A_3 are to be found from the conditions that

$$\left.\begin{aligned} \sigma_r &\equiv (1/r)\,(d\phi/dr) = 0 \quad \text{at } r = a, b \\ \int_a^b \sigma_\theta\, r\, dr &\equiv \int_a^b r(d^2\phi/dr^2)\, dr = 0 \end{aligned}\right\} \quad (14)$$

It should be noted that the equilibrium condition $\int_a^b \sigma_\theta\, dr = 0$ is automatically satisfied if $\sigma_r = 0$ at $r = a, b$. The expressions of Eqs. (5) for σ_θ and for the constants in question are readily obtained from the above conditions. An alternate derivation of Eqs. (5) may be obtained by superposition of the solution for a heated hollow cylinder and for a beam in pure bending, both of which may be found in reference 1; this fact was used as a check of the present work.

References

[1] Timoshenko, S., and Goodier, J. N., *Theory of Elasticity* 2nd Ed.; McGraw-Hill Book Company, Inc., New York, 1951.

[2] Barrekette, E. S., *Thermal Stresses in Curved Beams*, M.S. Thesis No. 698, Institute of Flight Structures, Department of Civil Engineering and Engineering Mechanics, Columbia University, New York, October, 1956.

[3] Timoshenko, S., *Strength of Materials*, Vol. II, 2nd Ed.; D. Van Nostrand Company, Inc., New York, 1941.

[4] Boley, B. A., *The Determination of Temperature, Stresses and Deflections in Two-Dimensional Thermoelastic Problems*, Journal of the Aeronautical Sciences, Vol. 23, No. 1, pp. 67–75, January, 1956.

An Experimental Study of the Turbulent Boundary Layer Behind the Initial Shock Wave in a Shock Tube†

WALTER A. MARTIN*
University of Toronto

SUMMARY

A study was made of the shock tube boundary layer between the initial shock wave and the contact region for shock pressure ratios P_{21} of 2.75 and 8.0 with a corresponding Reynolds Number range of 0–50 × 10^6 and 0–100 × 10^6, respectively. The Reynolds Number is based on the distance behind the shock wave and fluid properties evaluated at the wall. Shadowgraph, schlieren, and interferogram photographs and thin-film thermometer measurements indicated that the region was almost completely occupied by turbulent boundary layer. Experimental density profiles and boundary-layer thickness measurements are presented together with calculated temperature and velocity profiles, displacement and momentum thicknesses, and local skin friction. Results are compared with the theory of Mirels in NACA TN 3712. In view of the assumptions of the theory the agreement is quite good. The velocity profiles at higher Reynolds Number for $P_{21} = 2.75$ follow a 1/5 power law closer than the 1/7 power law of TN 3712. For $P_{21} = 8$ all the experimental profiles are a 1/5 power. As a means of comparison the theory was redeveloped on the basis of the 1/5 power law for velocity.

SYMBOLS

Fig. 1 serves to define the flow regions in the shock tube. The notation Air/Air and He/Air denotes a gas combination across the diaphragm, the left-hand symbol representing the gas in the chamber and the right-hand symbol the gas in the channel.

- a = velocity of sound
- c_{fw} = local skin-friction coefficient
- $\vec{C}$ = contact surface moving to the right
- C_p = specific heat at constant pressure
- C_{ps} = wall material specific heat
- k_s = wall material conductivity
- K = Gladstone-Dale constant = (index of refraction − 1)/ρ
- L = test-section span
- L_R = reduced test-section span due to boundary layer on test-section windows = $L(1 - 2\delta_z)$
- N = integer in exponent $1/N$ for the velocity profile of the turbulent boundary layer
- p = pressure
- R = gas constant
- $\overleftarrow{R}$ = backward facing rarefaction wave (particles enter from left)
- R_e = Reynolds Number
- r = recovery factor defined by Eq. (8)
- S = nondimensional fringe shift
- $\overrightarrow{S}$ = forward facing shock wave (particles enter from right)
- T = temperature
- t = time
- u, v = velocities parallel to x, y axes
- $\bar{u}, \bar{v}$ = velocities parallel to $\bar{x}$, $\bar{y}$ axes
- u_w = velocity of wall in x, y coordinates
- w = velocity of initial shock wave in $\bar{x}$, $\bar{y}$ coordinates
- X = distance from measuring station to diaphragm station
- x_s = distance from initial shock wave to measuring station
- x, y = coordinates with respect to shock wave
- $\bar{x}, \bar{y}$ = coordinates with respect to wall
- z = coordinate normal to window with origin at the ray exit window
- δ = velocity-boundary-layer thickness
- δ_y = velocity-boundary-layer thickness on floor of shock tube
- δ_z = velocity-boundary-layer thickness on test section windows
- δ^* = boundary-layer displacement thickness defined by Eq. (10)
- σ = Prandtl Number
- θ = boundary-layer momentum thickness defined by Eq. (11)
- λ = wavelength of light in angstrom units
- ν = kinematic viscosity
- ρ = density
- ρ_s = wall material density
- τ = local shear stress

Subscripts

- 1 = undisturbed region ahead of the initial shock wave
- 2, e = flow region behind the initial shock wave outside of the boundary layer
- m = quantity evaluated at a mean temperature
- w = quantity evaluated at the wall surface

Dimensionless Quantities

- P_{21} = pressure ratio across the initial shock wave, p_2/p_1
- T_{21} = temperature ratio across initial shock wave, T_2/T_1

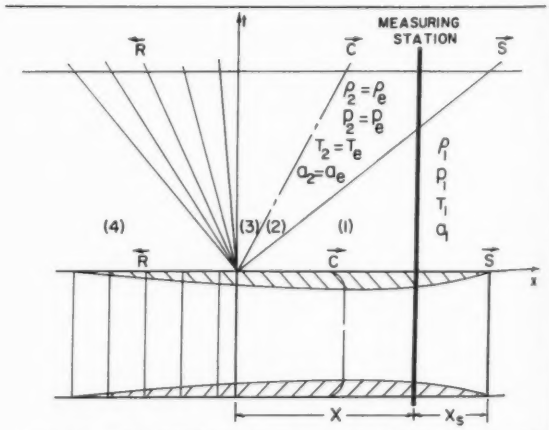

FIG. 1. The boundary layer in the shock tube. Note: subscript e is taken from reference 6 and subscripts 1 and 2 are taken from reference 8.

Received January 22, 1958.

† Financial support for this work was provided by the Defence Research Board of Canada.

* Formerly, Research Assistant, Institute of Aerophysics. Now, Senior Aerodynamics Engineer, Convair, A Division of General Dynamics Corporation, San Diego, Calif.

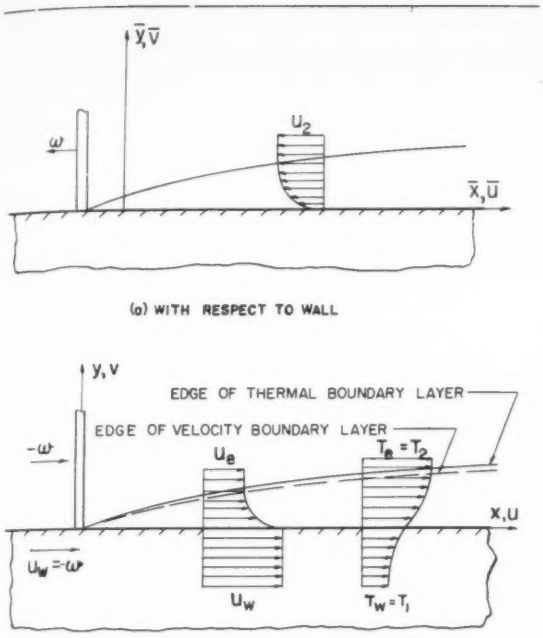

FIG. 2. The coordinate systems used to study the shock tube boundary layer.

INTRODUCTION

IN RECENT YEARS a great deal of interest has been shown in the shock tube boundary-layer problem. Much of this interest stems from the study of shock attenuation in the shock tube. The laminar-boundary-layer case was investigated theoretically in reference 1 in conjunction with a shock-attenuation study. In reference 2 an attenuation theory was developed and comparison with experiment indicated that the boundary layer was most likely to be of the turbulent type. Experiments carried out in reference 3 also agreed very closely with the theory of reference 2, however, both of these studies were concerned primarily with the attenuation problem. The laminar boundary layer was investigated theoretically in reference 4, while reference 5 presented a similar theory plus experimental verification. In reference 6 a turbulent-boundary-layer solution was added to the theory of reference 4.

The present work is an experimental study of the turbulent boundary layer created on the floor of a shock tube by the passage of the initial shock wave down the tube; the results are compared with the theory of reference 6. This study was carried out in the UTIA 2 × 7 in. shock tube using a 9 in. field Mach-Zehnder interferometer to obtain boundary-layer density profiles. Profiles were measured in the turbulent boundary layer developed on the shock tube floor at various times after the shock passed a station located on the test section windows. The test region was bounded by the shock wave and the contact surface—i.e., region 2 in Fig. 1. The boundary layer was studied behind shock waves of strength (P_{21}) 2.75 and 8.0. From the density profiles the temperature and velocity profiles were calculated, and, using these profiles, it was possible to obtain displacement and momentum thicknesses. Boundary-layer thickness was measured from the interferograms. Wall temperature increase was measured using a thin-film resistance thermometer. A more detailed description of these experiments is given in reference 7 and the pertinent shock tube theory will be found in reference 8.

THE BOUNDARY LAYER IN THE SHOCK TUBE

The shock tube boundary layer is somewhat different from the steady flow boundary layer found in the wind tunnel. However, in order to study this nonstationary boundary layer, a coordinate system has been adopted which essentially reduces the problem to one of steady flow, except that the wall has a finite velocity equal and opposite to the initial shock wave velocity. This method was adopted in references 1, 4, 5, and 6 and, since the present experiments were compared with the theory of reference 6, some of the notation of that report will be used to describe this boundary layer.

Fig. 1 serves to define the regions in the shock tube and illustrate the shock tube boundary layer. Fig. 2 presents the two coordinate systems used, one fixed with respect to the tube wall and the other attached to the shock wave. The two systems can be related as follows:

$$\left.\begin{aligned} \bar{x} &= x - u_w t, \quad \bar{y} = y \\ \bar{u} &= u - u_w, \quad \bar{v} = v \end{aligned}\right\} \tag{1}$$

The wall moves with a velocity $u_w = -w$ in the x, y coordinate system.

The velocity profiles in the x, y coordinate system corresponds to the usual profile found in two-dimensional steady flow. However, in this case, the choice of the coordinate system enables the boundary layer in the shock tube to be studied using proved steady-flow methods. Thus, in Fig. 2(b), the velocity profile obtained is complimentary to the profile of Fig. 2(a).

The density and temperature profiles of the nonstationary boundary layer are also opposite to those usually found for the wind tunnel case. In region 2 outside the boundary layer the physical properties are p_2, ρ_2 and T_2 (see Fig. 1). It was assumed in reference 6 that the wall temperature remained constant at the room temperature, T_1 (see also references 5 and 9), which is also the temperature of the gas at rest ahead of the shock. The temperature increases from $T_w = T_1$ at the wall ($y = 0$) to a value of $T_2 > 1$ at the edge of the boundary layer ($y = \delta$). Therefore, in the shock tube, the free-stream temperature is greater than the wall temperature, while in the wind tunnel the situation is usually reversed and the wall temperature exceeds the free-stream value.

For the shock strengths of interest here, the gas may be assumed perfect with an equation of state $p = \rho RT$ where R = constant, due to constant specific heats C_p and C_v. The assumption is also made that the

pressure in region 2 (p_2) is constant across the boundary layer. The density then varies inversely as the temperature, and at the wall

$$\rho_w/\rho_2 = T_2/T_w = T_{21} \qquad (2)$$

Referring to the coordinate system of Fig. 2(b), the density ratio ρ_w/ρ_2 is directly related to the ratio of the wall velocity and the velocity outside the boundary layer, u_w/u_e. This velocity ratio is used as a basic parameter in the theory of reference 6. The shock strengths of the present experiments correspond to values of u_w/u_e equal to 2.00 ($P_{21} = 2.75$) and 3.50 ($P_{21} = 8.00$).

Experimental Method

Outline of Experiments

The shock tube used for these experiments is described in reference 10. However, when the 9-in. field interferometer was built,[11] a new test section[12] was designed so that the interferometer could be used with this shock tube. It was the floor of this new test section that was used for the study of the turbulent boundary layer.

Three series of experiments were carried out with $P_{21} = 2.75$. At $X = 77$ in. (see Fig. 1), a He/Air combination was used which lowered the diaphragm pressure ratio but also reduced the test time. By using an Air/Air combination and increasing X to 141 in. the test time was tripled. However, the diaphragm pressure ratio required was very close to the limits of the equipment. In both cases a channel pressure of 300 mm. Hg gave adequate fringe shift. The third series of experiments was at $X = 141$ in. using a He/Air combination. This meant a lower diaphragm pressure ratio, but in turn a shorter test time. Each of the above experiments was repeated as a check on repeatability.

For a P_{21} of 8.00 it was necessary to use a He/Air combination to obtain this shock strength. The channel pressure was 120 mm. Hg and the test section was located 141 in. from the diaphragm; the experiments were repeated twice. The pressure ratio of 8 was about the maximum attainable using a helium driver gas and sufficiently high channel density to provide adequate fringe shift with the 2-in. tube width. At both shock strengths the densities were high enough to give early transition from a laminar to a turbulent boundary layer.

Records were obtained over the range of test time available by taking a series of spark photographs as the shock wave progressed downstream from the measuring station, producing a series of interferograms of the boundary layer in region 2. The diaphragm pressure ratio was adjusted so that the shock wave arrived at the measuring station with the required shock pressure ratio. One interferogram was obtained for each shock tube firing, the series being obtained by increasing the time delay controlling the spark. The runs were duplicated as closely as possible, so that the records were obtained under near identical flow conditions, as determined by the wave speed measured with the light screens. Variations in wave speed were less than one per cent.

Boundary-Layer Interferometry

Various authors[13–16] have discussed the techniques of boundary-layer interferometry. In practice several effects may introduce errors into interferometric results. The important effects for boundary-layer studies include misalignment of the test beam and the model, refraction of the test beam by the steep boundary-layer gradients, and the presence of a boundary layer on the test section windows. The last is often referred to as a corner effect where the floor and window boundary layers meet.

A similar method to that used in reference 13 was adopted here for aligning the test beam with the floor. In the present experiments a special jig was constructed with two plates at right angles to each other and perpendicular and parallel to the test section floor. In this manner, alignment was possible in both the vertical and horizontal planes by viewing the diffraction pattern about each plate and adjusting the interferometer until the pattern was symmetric. This jig also served as a focusing device and a means of measuring the magnification factor in the focal plane ($z = L/3$).

Because of the refraction and diffraction effects, the image of the floor of the test section on the photographic plate did not represent the true floor location with respect to the free-stream fringes. In order to locate the floor accurately, an inked reference line was placed on the test section windows, nearest the camera and several inches above the floor, well above the floor boundary layer. Before each set of experiments were performed a no-flow calibration photograph was taken with the jig inserted in the test section. From this photograph a measurement of the distance from the ink line to the floor was made, and the magnification factor determined from a measurement of the image of the jig. Having established the ink-line-to-floor measurement on the negative, this distance was measured off from the line on each flow photograph of the set in order to locate the floor. Further details of this technique will be found in reference 7.

Evaluation of some preliminary results indicated that any correction due to the refraction effects had a negligible influence in determining a density profile. However, it was also found that a correction was needed for the boundary layer on the test section windows. The density profile was evaluated by means of a relationship developed in reference 16 which included the corner effects. This relationship for the present experiments is given below.

$$\rho/\rho_2 = 1 + (\lambda S/K\rho_2 L_R) - (2/L_R)(1 - T_{21}) \times \left\{[1 + N(y/\delta_y)^{(N+1)/N}]\,[\delta y/(N+1)] - y\right\} \qquad (3)$$

The wall and window boundary-layer thicknesses were assumed to be identical ($\delta_z = \delta_y$).

Both horizontal and vertical fringe interferograms were taken during the preliminary studies. After examining these two methods the technique of using closely spaced horizontal fringes, parallel to the test section floor, was adopted. One of the advantages of this method is that measurement in the y direction only is required for evaluation. These measurements were done on a comparator equipped with 10 power optics which could be read to 0.00005 in. The density profiles were computed, using Eq. (3), on the University of Toronto digital computer FERUT.

Wall Temperature, Transition, and Density Gradient

In order to establish whether the theory of reference 6 was applicable to these experiments, an experimental check was made on the assumptions of negligible streamwise pressure gradient and wall temperature increase. The pressure gradient was estimated from interferometer studies, while the wall temperature rise was estimated from thin-film resistance thermometer records.

It can be shown[17] that such a thin film with its negligibly small heat capacity measures the surface temperature of the backing with negligible time lag. The thermometer was a gold film approximately a tenth micron thick, 1/8 in. wide by 3/4 in. long evaporated onto a backing of araldite plastic.* With the present films, the response time of the film to a shock wave was essentially the transit time of the shock wave across the 1/8-in. width. From the measured change in backing surface temperature, the temperature change of the steel wall could be computed.

The thin-film thermometer was located 12 in. downstream of the measuring station at the test section. The resultant signal was displayed on an oscilloscope and photographed; measurements were made from the record to determine the wall temperature rise. The transition from a laminar to a turbulent boundary layer was also indicated on these records. Shadow and schlieren photographs were taken as a means of checking on the transition point.

The technique for determining free-stream density gradient entailed measurement of the fringe shift due to the density increase across the shock at a series of stations between the shock and contact front. Knowing the density gradient, the corresponding pressure gradient could be estimated by assuming an adiabatic relationship between density and pressure.

The fringe shift across the shock was measured in the first photograph of each set. However, some other reference was needed for the succeeding photographs. The reference used was the ink line drawn on the test section window. Before firing the shock tube, and with the channel held at the operating pressure, the zero-order fringe was aligned along the ink line using an AH3 steady source. Once this was done the chamber was pressurized, the plate holders inserted in the camera, the spark source replaced, and the tube fired.

* The evaporation of the films was done by the Physics Department of the University of Toronto.

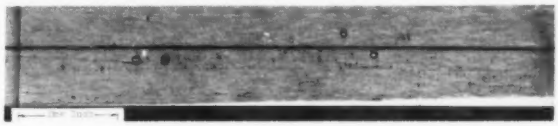

PLATE 1. Schlieren photograph of the boundary-layer development behind the initial shock wave. The shock wave is at the extreme left ($P_{21} = 8.00$, $p_1 = 120$ mm. Hg, He/Air).

The time delay was adjusted so that a photograph was taken at a later time corresponding to another value of x_s and the above procedure repeated. In this way the ink line represented the zero order fringe position before firing the shock tube. This reference could be used to measure the fringe shift for a number of stations behind the shock wave, and from this shift the density and pressure gradient could be determined.

EXPERIMENTAL RESULTS

Transition and Wall Temperature

(a) *Transition*—Measurements taken from the schlieren and shadowgraph records indicated that only a very small portion of the floor boundary layer behind the shock wave was laminar. For $P_{21} = 2.75$ with $p_1 = 300$ mm. Hg, transition started about 1.3 in. behind the shock but the boundary layer did not appear to become fully turbulent until after 4 to 6 in. With $P_{21} = 8$ and $p_1 = 120$ mm. Hg, transition started about 0.75 in. behind the shock and at 3 in. a fully turbulent boundary layer had developed. Plate 1 is a schlieren photograph illustrating the growth of the boundary layer behind the shock.

The thin-film thermometer records obtained on the 7-in. side wall could also be used to estimate a transition point. Immediately behind the shock the heat transfer due to the laminar boundary layer varies as $1/\sqrt{t}$, which provides a step increase in wall temperature.[18] Upon transition to a turbulent boundary layer, the change in heat-transfer rate produces a marked change in slope on the thin film thermometer records. The lengths of side wall laminar boundary layers estimated in this way were 3 in. for $P_{21} = 2.75$, and 1 in. at $P_{21} = 8$.

The transition may be characterized by the Reynolds Number based on wall values

$$R_{e_{T_w}} = (u_e x_T/\nu_w)\,[1 - (u_w/u_e)]^2 \qquad (4)$$

where x_T is the distance behind the shock at which transition occurs, or by the same Reynolds Number based on free-stream values.

$$R_{e_{T_e}} = (u_e x_T/\nu_e)\,[1 - (u_w/u_e)]^2 \qquad (5)$$

TABLE 1

Method	P_{21}	p_1(mm. Hg)	$R_{e_{T_w}}$	$R_{e_{T_e}}$
Optical (Tube Floor 2″ wide)	2.75	300	0.33×10^6	0.18×10^6
	8	120	0.75×10^6	0.14×10^6
Thin-Film Thermometer (7″ side wall)	2.75	300	0.75×10^6	0.39×10^6
	8	120	1×10^6	0.19×10^6

The present transition results, in terms of R_{eT_w} and R_{eT_e}, are summarized in Table 1.

A systematic study of transition was considered outside the scope of the present work; however, the data obtained indicated that transition was completed about 4 in. behind the shock wave for the two shock strengths used. This was the location chosen for the first measuring station in both cases.

(b) *Wall Temperature Rise*—In addition to information on transition, the film thermometer records permitted an estimate of maximum wall temperature rise, ΔT_w. It can be shown[9] that the wall surface temperature rise is proportional to $\sqrt{1/\beta_s}$ where $\beta_s = \rho_s k_s C_{p_s}$. Thus, the temperature rise ΔT_w, experienced by the steel shock tube walls in the present case, may be expressed as

$$\Delta T_w = \Delta T_F \sqrt{\beta_a/\beta_s} \tag{6}$$

where subscripts a and s refer to araldite and steel, respectively.

Measurements made at this laboratory gave a value of $\sqrt{\beta_a} = 1.96$ B.t.u. ft.$^{-2}$ (°F.$^{-1}$) (hour)$^{-1/2}$. The corresponding value of $\sqrt{\beta_s} = 40.9$ in the same units. Therefore, Eq. (6) becomes

$$\Delta T_w/\Delta T_F = 0.05 \tag{7}$$

The thin-film thermometer experiments may be summarized as follows:

P_{21}	ΔT_F	ΔT_w
2.75	2.08°C.	0.10°C.
8.00	11.2°C.	0.56°C.

This table shows that the wall remained at essentially constant temperature during these experiments.

Streamwise Density Gradient

Any ordered change in S from streamwise density gradient was masked by scatter. The maximum percentage variation in pressure (assuming adiabatic pressure-density relation) corresponding to the maximum scatter in measured fringe shift is given in the summary below.

P_{21}	Gas Combination	Maximum % Var. in ρ	Maximum % Var. in p
2.75	He/Air	5	7
8.00	He/Air	7	10

This table shows that the scatter could mask a maximum increase in pressure of 7 per cent for $P_{21} = 2.75$ and 10 per cent for $P_{21} = 8$. In view of the results of various attenuation studies and experiments, some pressure gradient was to be expected. Pressure increases with increasing distance behind the shock have been reported by various authors—e.g., reference 2. The theory of reference 6 is for a shock advancing over a wall of infinite extent, whereas the flow in the present case is confined by the walls of the tube which causes a slight pressure gradient to be created. It is felt, however, that the possible pressure gradient existing was small enough that the experimental results can be compared with the theory of reference 6.

Density, Temperature, and Velocity Profiles

Assuming constant pressure through the boundary layer, the ratio T/T_e is equal to the density ratio ρ_e/ρ. Therefore, the measured density profiles are presented as temperature profiles in Figs. 3, 4, and 5. The conditions of each experiment are given on the respective Figures, each Figure representing the results of at least two sets of experiments. Due to the large temperature gradients existing at the wall it was not possible to measure the wall value interferometrically. However, as shown by the thin-film thermometer results, the wall temperature remains essentially constant at room temperature, which enabled the ratio T_w/T_e to be fixed.

Figs. 6 and 7 are velocity profiles computed from the temperature profiles of Figs. 3 and 5, respectively. These profiles were calculated from the temperature results using the Crocco equation[19] in the following form:[6]

$$\left.\begin{aligned} T/T_e &= (T_w/T_e)\,[1 + b(\bar{u}/\bar{u}_e) - c(\bar{u}/\bar{u}_e)^2] \\ &= (T_w/T_e)\,[1 + b(\delta^*/\delta)^{1/N}\,(y/\delta^*)^{1/N} - \\ &\qquad c(\delta^*/\delta)^{2/N}\,(y/\delta^*)^{2/N}] \end{aligned}\right\} \tag{8}$$

where

$$b = (T_r/T_w) - 1, \quad c = [(T_r/T_e) - 1]T_{21}$$
$$T_r/T_e = 1 + [(u_w/u_e) - 1]^2[u_e^2 r(0)/2T_e c_{p_m}]$$
$$r(0) \cong \sqrt[3]{\sigma_m}$$

Although the Crocco relation was developed for a Prandtl Number of unity, the coefficients b and c are presented in terms of a recovery temperature in keeping with the theory of reference 6, which assumes the Crocco equation should hold for values of the Prandtl Number not too far from one.

Calculating the experimental velocity profiles for Prandtl Numbers other than one produced very little change in the results. Similarly, the theoretical temperature curves were virtually unchanged when calculated for Prandtl Numbers of 0.69 ($P_{21} = 2.75$) and 0.665 ($P_{21} = 8$). These values were taken from reference 24.

The velocity profile may be expressed as a function of the similarity parameter $\zeta_T = y/\delta$ or $\zeta_T = (y/\delta^*)(\delta^*/\delta)$, giving

$$\left|(u - u_w)/(u_e - u_w)\right| = \zeta_T^{1/N} = \bar{u}/\bar{u}_e \qquad \text{for } 0 \le \zeta_T \le 1 \tag{9}$$

This relationship will be equal to unity for $\zeta_T \ge 1$.

In view of the lack of any existing experimental evidence for the turbulent boundary layer behind a moving shock wave, Mirels adopted the 1/7 power velocity profile from steady flow. This velocity relationship is plotted as a broken line on Figs. 6 and 7. The corresponding theoretical temperature profile is also plotted as a broken line on Figs. 3, 4, and 5.

The experimental results of Figs. 3, 4, and 5 all tend to fall along a single curve over the range of measurements taken; however, none of these results closely follow the 1/7 power profiles proposed in reference 6.

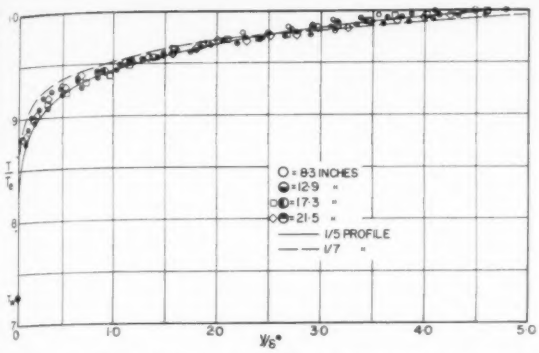

FIG. 3. Theoretical and experimental temperature profiles, T/T_e plotted against the ratio y/δ^*, He/Air, $u_w/u_e = 2.00$, $P_{21} = 2.75$, $X = 77$ in.

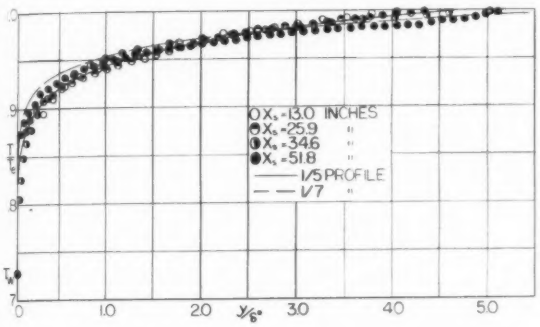

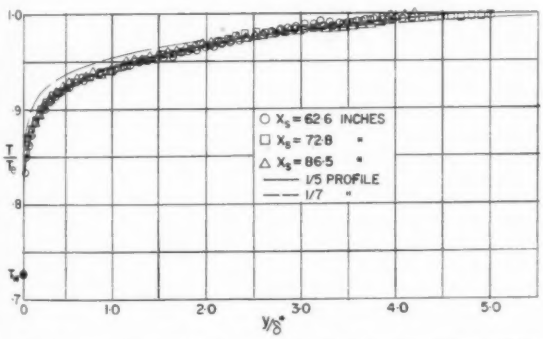

FIG. 4. Theoretical and experimental temperature profiles, T/T_e plotted against the ratio y/δ^*, Air/Air, $u_w/u_e = 2.00$, $P_{21} = 2.75$, $X = 141$ in.

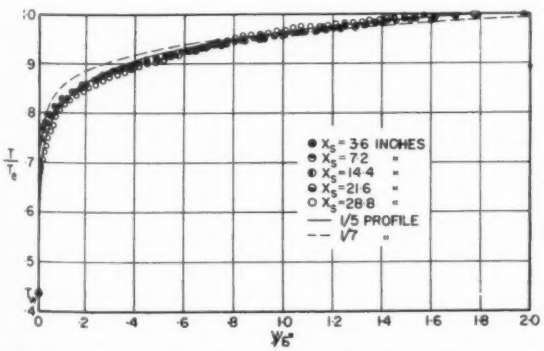

FIG. 5. Theoretical and experimental temperature profiles, T/T_e plotted against the ratio y/δ^*, He/Air, $u_w/u_e = 3.50$, $P_{21} = 8.00$, $X = 141$ in.

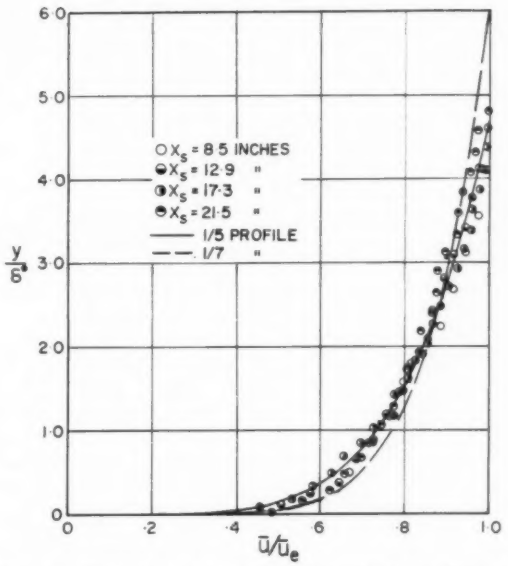

FIG. 6. Theoretical and experimental velocity profiles, u/u_e plotted against the ratio y/δ^*, He/Air, $u_w/u_e = 2.00$, $P_{21} = 2.75$, $X = 77$ in.

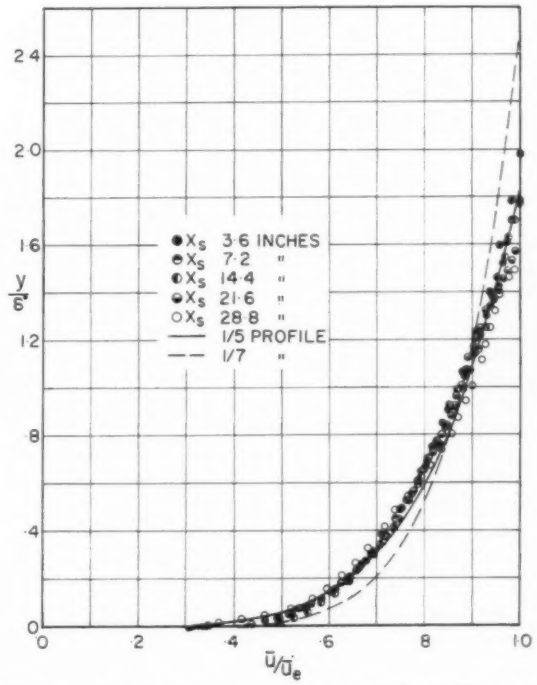

FIG. 7. Theoretical and experimental velocity profiles, u/u_e plotted against the ratio y/δ^*, He/Air, $u_w/u_e = 3.50$, $P_{21} = 8.00$, $X = 141$ in.

The deviation from the 1/7 power is most noticeable on Figs. 4(b) ($P_{21} = 2.75$) and 5 ($P_{21} = 8$). On both of these curves there is very little scatter and the data tends toward a higher power profile. Noting this, an attempt was made to determine the experimental profile. A 1/5 power curve was found to fit the measured points more closely and is plotted as a solid line on Figs. 3 through 7. Figs. 3 and 4(a) are similar in pattern, the experimental points falling between the theoretical curves, although the results of Fig. 4(a) do tend slightly toward the 1/5 power curve. In Figs. 4(b) and 5, however, there is very good agreement with the 1/5 power profile with less scatter than the previous results. Calculated velocity profiles are presented for each shock strength, and their behavior is nearly identical to the measured temperature profiles.

There may be some doubt as to the validity of the experimental velocity profiles. These profiles are deduced from density measurements on the assumption of constant pressure against the boundary layer using the Crocco equation [Eq. (8)]. This relation has not been proved valid for nonstationary flow. However, this relationship has seen widespread use for both laminar and turbulent boundary layers in steady flow. In reference 20 it was used in the same manner as used here—namely, to relate density, as measured interferometrically, to velocity for a turbulent boundary layer. In reference 21 experimental verification of the Crocco relation was carried out by means of flight measurements of the boundary layer on a body of revolution. Therefore, there seems to be some justification for its use here.

Theoretical Consideration for N = 5 and 7

As the experimental velocity and temperature profiles seemed to follow a 1/5 power law, it was decided to carry out the method of reference 6 for $N = 5$. The displacement and momentum thicknesses may be defined as follows:

$$\delta^* = \int_0^\infty [1 - (\rho u/\rho_e u_e)]dy \tag{10}$$

$$\theta = \int_0^\infty (\rho u/\rho_e u_e)\,[1 - (u/u_e)]dy \tag{11}$$

By substituting Eqs. (8) and (9) into Eqs. (10) and (11), the following boundary-layer shape parameters are obtained:

$$\delta^*/\delta = 1 - N(T_e/T_w) \times \{(u_w/u_e)I_{N-1} + [1 - (u_w/u_e)]I_N\} \tag{12}$$

$$\theta/\delta = N(T_e/T_w)\,[1 - (u_w/u_e)] \times \{(u_w/u_e)I_{N-1} + [1 - 2(u_w/u_e)]I_N - [1 - (u_w/u_e)]I_{N+1}\} \tag{13}$$

where I_{N-1}, I_N, and I_{N+1} are functions of b and c [see Eq. (8)] and are defined by the integral

$$I_a = \int_0^1 [Z^a dz/(1 + bZ - cZ^2)] \tag{14}$$

where $a = N - 1$, N, and $N + 1$.

Eqs. (8)–(14) were taken directly from reference 6 except that the general power $1/N$ was used instead of the value of 1/7. In the remainder of this section only the equations applying to $N = 5$ will be presented. The corresponding equations for $N = 7$ will be found in reference 6.

The integral form of the momentum equation is

$$\frac{\tau_w}{\rho_e u_e^2} = \frac{d}{dx}\int_0^\infty \frac{\rho u}{\rho_e u_e}\left(1 - \frac{u}{u_e}\right)dy = \frac{d\theta}{dx} \tag{15}$$

Assuming that the wall temperature is constant, θ/δ can be considered independent of x and Eq. (15) may be written

$$\tau_w/\rho_e u_e^2 = (\theta/\delta)\,(d\delta/dx) \tag{16}$$

In order to integrate Eq. (16), a relationship between τ_w and δ is required. The theory developed in reference 6 uses the Blasius relationship for compressible turbulent flow over a semi-infinite flat plate, evaluating the fluid properties at a mean temperature, T_m, as suggested by Eckert.[22]

The 1/7 power law, as given by Blasius, for the velocity distribution in a smooth pipe is[23]

$$\varphi(\eta) = 8.74(\eta)^{1/7} \tag{17}$$

In an attempt to follow the approach of reference 6 a curve was fitted to the famous results of Nikuradse for smooth pipes, given in Fig. 20.4 of reference 23. Therefore, as the power, 1/5, was already established, it was necessary to determine the constant, C. A value for C of 6.2 gave a reasonable fit to the Nikuradse results similar to that for $C = 8.74$. This value resulted in the following expression for the skin friction:

$$\tau_w/\rho u^2 = 0.0488\,(\nu/uy)^{1/3} \tag{18}$$

For a shock tube, this equation becomes

$$\tau_w/\rho_e u_e^2 = 0.0488\,\varphi[1 - (u_w/u_e)] \times \left|1 - (u_w/u_e)\right|^{2/3}(\nu_e/u_e\delta)^{1/3} \tag{19}$$

Substituting Eq. (19) into Eq. (16) gives

$$\delta = 0.130\left\{\varphi[1 - (u_w/u_e)]/(\theta/\delta)\right\}^{3/4} \times \left|1 - (u_w/u_e)\right|^{1/2}(\nu_e/u_e x)^{1/4}x \tag{20}$$

where $\varphi = (T_e/T_m)^{2/3}\,(\mu_m/\mu_e)^{1/3}$

Combining Eqs. (19) and (20) with Eq. (4a), where x_T is replaced by the more general value x, results in the local skin friction

$$c_{_w}R_e^{1/4} = 0.195\left\{\left[\frac{T_w}{T_e}\,\frac{\theta}{\delta}\,\frac{1}{1 - (u_w/u_e)}\right]\frac{\nu_m}{\nu_w} \times \left(\frac{\rho_m}{\rho_w}\right)^3\right\}^{1/4}\frac{1 - (u_w/u_e)}{\left|1 - (u_w/u_e)\right|} \tag{21}$$

Theoretical curves of δ, δ^*, θ, and c_{f_w} are shown on Figs. 8, 9, and 10 for both the 1/5 and 1/7 power law profiles.

Boundary-Layer Thickness, Displacement, and Momentum Thickness

Figs. 8 and 9 present plots of δ, δ^*, and θ versus x_s and Re_{x_s} [based on wall values, Eq. (4a)]. The boundary-

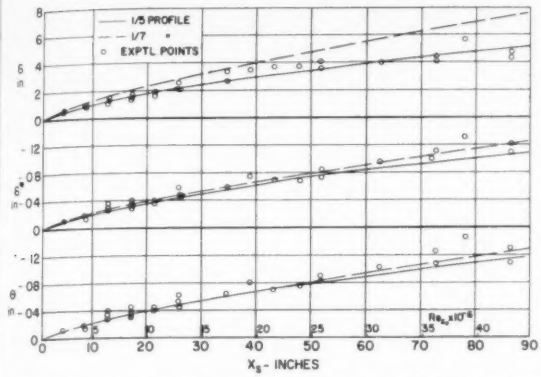

FIG. 8. Theoretical and experimental variation of the boundary thickness δ, displacement thickness δ^*, and momentum thickness θ, with the distance behind the shock wave x_s and the Reynolds Number $R_{e_{x_s}}$. $P_{21} = 2.75$, $p_1 = 300$ mm. Hg, $u_w/u_e = 2.00$. Note: the Reynolds Number in Figs. 8, 9, and 10 are evaluated for the fluid properties at the shock tube wall.

layer thickness, δ, came out of the program for determining density profiles, this thickness being arbitrarily defined as the value of δ corresponding to a density ratio of 0.996. Experimental values of δ^* and θ were determined from the density and velocity profiles by numerical integration of Eqs. (10) and (11) using FERUT.

The theoretical and experimental values of δ^* and θ agree reasonably well for $P_{21} = 2.75$. By the definition of δ^* and θ these values are both negative and in these coordinates θ is larger in magnitude than δ^*. The theoretical curve for $N = 7$ matches the experimental data somewhat better than for $N = 5$.

For $P_{21} = 8.00$, the two theoretical curves differ but slightly and, particularly for θ, both fall below the experimental results. The reason for this is not known. The large scatter around $x_s = 28$ in. for δ^* and θ is probably due to the conditions that exist in the shock tube at this value of x_s. This station is very close to the contact surface or cold front. The region behind the contact surface is not uniform and it is possible that disturbances are transmitted forward through the boundary layer to perturb the flow in region 2.

Too much significance cannot be attached to the comparison of theory with experiment for boundary-layer thickness in Figs. 8 and 9, as the experimental thickness has been arbitrarily taken as the value of y for $\rho_2/\rho = 0.996$. The theory for $N = 7$ overestimates, and that for $N = 5$ somewhat underestimates, this experimental thickness.

Skin Friction

Fig. 10 presents the results for local skin friction plotted against Reynolds Number. This Reynolds Number is identical to that defined by Eq. (4a). The experimental points were obtained by measuring the slope of a mean curve through the experimental θ versus x_s results in Figs. 8 and 9 and then using the following equation for c_{f_w}:

$$c_{f_w} = (d\theta/dx)\ [\rho_e u_e^2/(1/2)\rho_w(u_w - u_e)^2] \qquad (22)$$

The values of c_{f_w} are negative in the present coordinate system.

The agreement between theory and experiment is fairly good for $P_{21} = 2.75$ [Fig. 10(a)], the experimental skin-friction values falling between the two theoretical curves. However, for $P_{21} = 8$ the experimental points lie well above the two theoretical curves. This is to be expected in view of the corresponding results for momentum thickness shown in Fig. 10(b), which indicates a greater slope than the theoretical curves. The last group of points at $x_s = 28$ in. were not used in determining the slope for the skin-friction calculation. The Reynolds Number was not corrected for the small laminar portion of the boundary layer in Figs. 8, 9, and 10. However, the correction will be small in rela-

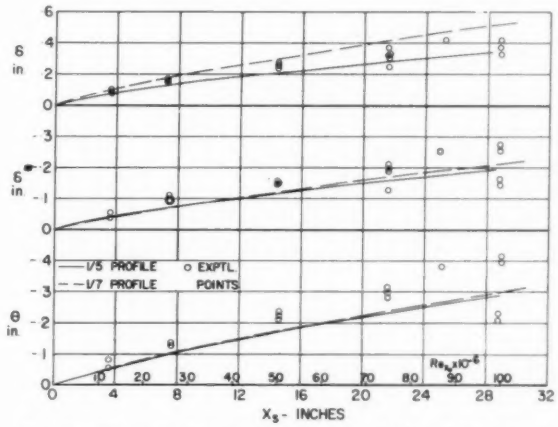

FIG. 9. Theoretical and experimental variation of the boundary-layer thickness δ, displacement thickness δ^*, and momentum thickness θ, with the distance behind the shock wave X_s and the Reynolds Number $R_{e_{x_s}}$. $P_{21} = 8.00$, $p_1 = 120$ mm. Hg, $u_w/u_e = 3.50$.

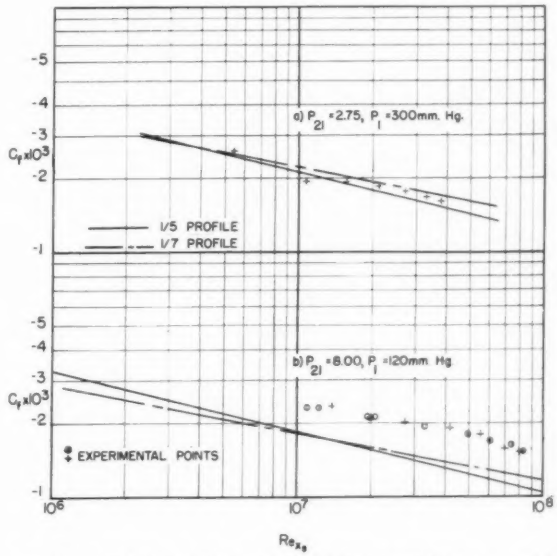

FIG. 10. Variation of the local skin-friction coefficient c_{f_w} with Reynolds Number $R_{e_{x_s}}$.

tion to the very large Reynolds Number obtained as defined by Eq. (4a).

Conclusions

The assumptions of reference 6 were as follows: (1) zero pressure gradient, (2) velocity profile to follow a 1/7 power law, (3) Crocco relation related density or temperature to velocity, (4) wall temperature remained constant at room temperature, and (5) Blasius relation for the shear stress was extended to the moving wall case.

In the present experiments, a small streamwise pressure gradient probably existed with pressure increasing with distance behind the shock wave. An attempt was made to measure the streamwise gradient by interferometry, but any ordered change was masked by scatter. Measurement of the steel wall temperature rise by means of a thin-film resistance thermometer showed it to be negligibly small.

In general, the theory of reference 6 compares favorably with the experimental results obtained, considering the assumptions of the theory and those inherent in deducing velocity from the experimental density profiles. In particular, good agreement is obtained for the weaker shock case with $P_{21} = 2.75$. For the stronger shock case with $P_{21} = 8.00$, experimental displacement and momentum thicknesses and skin friction are found to be greater in absolute value than predicted by the theory.

At the higher Reynolds Numbers, and particularly for $P_{21} = 8.00$, the experimental temperature and velocity profiles followed a 1/5 power law more closely than a 1/7 power law. The method of reference 6 was, therefore, applied for a 1/5 power law to calculate displacement and momentum thicknesses and skin friction. The calculated results for the 1/5 power law differ very little from those for the 1/7 power velocity profile and show little, if any, improvement in agreement with the experimental results.

References

[1] Hollyer, R. J., Jr., *A Study of Attention in the Shock Tube*, Proj. M720-4 (Contract N6-ONR-232 TO IV, Office of Naval Research), University of Michigan, Eng. Res. Inst., July, 1953.

[2] Trimpi, R. L., and Cohen, N. B., *A Theory for Predicting the Flow of Real Gases in Shock Tubes with Experimental Verification*, NACA TN 3375, 1955.

[3] Boyer, D. W., *Effects of Kinematic Viscosity and Wave Speed on Shock Wave Attenuation*, UTIA Technical Note, No. 8, 1956.

[4] Mirels, H., *Laminar Boundary Layer Behind Shock Advancing Into Stationary Fluid*, NACA TN 3401, 1955.

[5] Bershader, D., and Allport, J., *On the Laminary Boundary Layer Induced by a Traveling Shock Wave*, Princeton University, Dept. of Physics, Tech. Report II-22, 1956.

[6] Mirels, H., *Boundary Layer Behind Shock or Thin Expansion Wave Moving into Stationary Fluid*, NACA TN 3712, 1956.

[7] Martin, W. A., *An Experimental Study of the Boundary Layer Behind a Moving Plane Shock Wave*, UTIA Report No. 47, May, 1957.

[8] Glass, I. I., Martin, W. A., and Patterson, G. N., *A Theoretical and Experimental Study of the Shock Tube*, UTIA Report No. 2, 1953.

[9] Rott, N., and Hartunian, R., *On The Heat Transfer to the Walls of a Shock Tube*, Graduate School of Aeronautical Engineering, Cornell University (Contract AF 33 (038)-21406), 1955.

[10] Bitondo, D., and Lobb, R. K., *The Design and Construction of a Shock Tube*, UTIA Report No. 3, 1950.

[11] Hall, J. G., *The Design and Performance of a 9-Inch Plate Mach-Zehnder Interferometer*, UTIA Report No. 27, 1954.

[12] Hall, J. G., *The Transition Through a Contact Region*, UTIA Report No. 26, 1954.

[13] Wachtell, G. P., *Refraction Error in Interferometry of Boundary Layer in Supersonic Flow Along a Flat Plate*, Ph.D. Thesis, Princeton University, 1951.

[14] DeFrate, L. A., *Application of the Interferometer to the Study of Boundary Layer*, Sc.D. Thesis, Massachusetts Institute of Technology, 1950.

[15] Howes, W. L., and Buchele, D. R., *Generalization of Gas Flow-Interferometry Theory and Interferogram Evaluation Equations for One-Dimensional Density Field*, NACA TN 3340, 1955.

[16] Howes, W. L., and Buchele, D. R., *Practical Considerations in Specific Applications of Gas-Flow Interferometry*, NACA TN 3507, 1955.

[17] Rabinowicz, J., Jessey, M. E., and Bartsch, C. A., *Resistance Thermometer for Heat Transfer Measurement in a Shock Tube*, GALCIT Hypersonic Research Project Mem. No. 33, Army Ordinance Contract No. DA-04495-Ord.-19, July, 1956.

[18] Bromberg, R., *Use of the Shock Tube Wall Boundary Layer in Heat Transfer Studies*, Jet Propulsion, Vol. 26, No. 9, pp. 737-740, September, 1956.

[19] Crocco, L., *Transmission of Heat from a Flat Plate to a Fluid at a High Velocity*, NACA TN 690, 1932.

[20] Ladenburg, R., and Bershader, D., *Optical Studies of a Boundary Layer Phenomena on a Flat Plate at Mach Number 2.35*, Princeton University Report, NRO61-020, 1952.

[21] Swanson, A. G., Buglia, J. J., and Chauvin, L. T., *Flight Measurements of Boundary-Layer Temperature Profiles on a Body of Revolution (NACA RM-10) at Mach Numbers from 1.2 to 3.5*, NACA TN 4061, 1957.

[22] Eckert, E. R. G., *Engineering Relations for Heat Transfer and Friction in High-Velocity Laminar and Turbulent Boundary-Layer Flow over Surfaces with Constant Pressure and Temperature*, ASME Transactions, Vol. 78, No. 6, 1956.

[23] Schlichting, H., *Boundary Layer Theory*, McGraw-Hill Book Co., Inc., New York, 1955.

[24] Keenan, J. H., and Kaye, J., *Gas Tables*, John Wiley and Sons, Inc., New York, 1948.

Readers' Forum

BRIEF REPORTS of investigations in the aeronautical sciences and discussions of papers published in the JOURNAL are presented in this special department. Entries must be restricted to a maximum of 1,300 words or the equivalent of one JOURNAL page including formulas and illustrations. Publication is completed as soon as possible after receipt of the material. The Editorial Committee does not hold itself responsible for the opinions expressed by the correspondents.

Contents

Upper Atmosphere Atomic-Oxygen Power Plant ..... STERGE T. DEMETRIADES 653

Static Friction in Dynamic Systems ..... CARL F. BRANSON 654

Vaporization Into a Hypersonic Laminar Boundary Layer ..... SINCLAIRE M. SCALA 655

On Simplified Fuselage-Structure Stress Distributions ..... W. R. JENSEN 656

Further Remarks on the Torsional Rigidity of Thermally Stressed Wings ..... R. L. BISPLINGHOFF 657

Polynomial Expressions for the Specific Heat and Prandtl Number of Air ..... DONALD W. BOEKEMEIER 658

On a Complementary Energy Principle in Linear Thermoelasticity ..... G. HERRMANN 660

Further Numerical Data on Blunt Bodies ..... H. MELVIN LIEBERSTEIN 660

Errata—"On Unsteady Interaction Between a Weak Thermal Layer and a Strong Plane Oblique Shock" ..... C. T. CHANG 661

Similar Solution of a Laminar Boundary Layer With Rotational Free Stream ..... FRANKLIN D. HAINS 662

Some Experiments on Effects of Yaw on Boundary-Layer Development in Supersonic Cone Flow ..... D. G. DECOURSIN AND W. S. BRADFIELD 662

Upper Atmosphere Atomic-Oxygen Power Plant

Sterge T. Demetriades
Technical Consultant, Aerojet-General Corporation, Azusa, Calif.

May 15, 1958

CONSIDERABLE INTEREST has been generated about the family of "excraft" (exospheric aircraft) that is being studied at the Astronautics Laboratory of Aerojet-General Corporation under sponsorship of the Directorate of Advanced Studies of the Air Force Office of Scientific Research. Recombination of the atomic oxygen available in the upper atmosphere* has been considered as the source of energy for excraft propulsion.

The author and coworkers[1, 2] have presented theoretical estimates of the recombination kinetics of atomic oxygen. These results can be summarized by a homogeneous (volume) recombination rate given by

$$[d(O_2)/dt]_{HM} = k_1(O)^2(u)\left\{1 - [(O_2)/K_{c1}(O)^2]\right\} + 2k_2K_{c3}[(O_3)^2/(O_2)], \text{ moles/sec.-cc.} \quad (1)$$

where (O), (O_2), (O_3), and (u) are the concentrations of oxygen atoms, oxygen molecules, and ozone molecules, and the total concentration respectively in moles/cc.; k_1 is the three-body recombination rate constant; k_2 is the rate constant for ozone decomposition by the mechanism $O_3 + O \rightarrow 2O_2$; K_{c1} is the equilibrium constant $(O_2)/(O)^2$; and K_{c3} is the equilibrium constant $(O_2)\ (O)/(O_3)$. These constants are given by

* I prefer the term exosphere for the lower upper atmosphere and the term phygosphere (Greek phygē = escape) for the extreme upper atmosphere where the mean free path is larger than the scale height.

Contributors Please Note

Readers' Forum items must be confined to the equivalent of one page in the *Journal*. Contributions that exceed this limit will be returned to the authors for condensation and rewrite. To avoid inconvenience and delay, please adhere to the following specifications:

(1) Five, double-spaced, typewritten, manuscript pages ($8\frac{1}{2}$ by 11 in.), including wide margins, formulas, and headings equal one printed page.

(2) For every illustration, deduct at least one-half or as much as one manuscript page, depending on the size of the illustration.

$$k_1 = 3 \times 10^{16(\pm 1)} (300/T)^{1.5}, \quad \text{cc.}^2/\text{mole}^2\text{-sec.}, \ 300°\text{K.} < T < 4{,}000°\text{K.} \quad (2)$$

$$k_2 = 1.07 \times 10^{13} (T/500) 10^{-(1{,}050/T)}, \quad \text{cc./mole-sec.}$$
$$K_{c1} = (O_2)/(O)^2 = 10^{[(25{,}700/T) - 1.390]} \quad (3)$$

and

$$K_{c3} = (O_2)(O)/(O_2) = 10^{[-(5{,}620/T) + 6.93 - \log_{10} RT]} \quad (4)$$

where $R = 82.06$ atm.-cc./°K.-mole; and $T = °\text{K}$. The uncertainty of $(+1)$ on the exponent of Eq. (2) arises mostly from the different efficiences of various possible third bodies. The effect of nitrogen and nitrogen oxides on the recombination rate of atomic oxygen is still uncertain.

The Demetriades-Farber estimates of heterogeneous (catalytic) recombination on surfaces can be summarized by

$$[d(O_2)/dt]_{HT} = 1.5 \times 10^5 (O)^2 \sqrt{T} + 9 \times 10^2 (O) f \sqrt{T}, \quad \text{moles/sec.-cm.}^2 \quad (5)$$

The efficiency f ranges from 0.001 for glass or aluminum to about 1.0 for the noble metals and some oxides.

TABLE 1
Summary of Upper Atmosphere Atomic Oxygen Recombination Power-Plant Spectrum

Velocity	Suborbital	Orbital
Mach Number at 100 km	0, 2, 4, 6, 8, 10, 12, 14, 16, 18, 20, 22, 24, 26, 28, 30, 32	
Type of Power Plant	Catalytic; Catalytic with ram compression; Pure compression; Thrust at 100 km less than 40 dynes/cm² of inlet; Subsonic compression; Supersonic compression	
Disadvantages and requirements	Lift too low (L<0.01 gm/cm²)* (L<0.08 gm/cm²)*; Compression required supersonic throughout power plant—Difficult inlet and diffuser design; Skin friction too high with present estimates; Wave or pressure drag losses could be severe; Length of pure compression power plant becomes excessive with present estimates; Severe radiation losses from catalytic walls	

*Lift per cm² of lift-producing surface

The recombination power-plant studies conducted at the Astronautics Laboratory and now in process of publication are summarized in Table 1. Considerable uncertainty exists about the effect of surface recombination on the skin friction, wave drag at 100 km., diffuser design (compression ratios of 1,000–5,000 are required), lift, availability of extremely light structures, etc. I doubt, however, if these parameters can be improved by the required order of magnitude soon.

In the atomic oxygen layer one might be able to extract lift from a foil at zero angle of attack coated with a catalyst (of low accommodation coefficient) on one side and a noncatalyst (of high accommodation coefficient) on the other, and thrust from a "wavy" foil coated with this catalyst on the forward-facing surfaces of its waves and a noncatalyst with high accommodation coefficient on the backward-facing surfaces.

References

[1] Demetriades, S. T., Farber, M., Kretschmer, C. B., *Investigation of Atomic-Oxygen Recombination Rates*, Aerojet-General Report 0103-01-2, August 14, 1957.

[2] Demetriades, S. T., and Farber, M., *A Theoretical Study of the Recombination Kinetics of Atomic Oxygen*, Aerojet-General TN-21, ASTIA No. AD148-057, November 8, 1957.

Static Friction in Dynamic Systems

Carl F. Branson
Senior Aerodynamics Engineer, Lockheed Aircraft Corporation, Georgia Division, Marietta, Ga.

May 19, 1958

THE USUAL CONCEPT of static or coulomb friction is a constant force with its sign opposite to the velocity. The explanation of some self-excited vibrations as given in reference 1 requires the force to decrease with the velocity, retaining the opposite sign, however. Such definitions are sufficient for predicting the effect on single-degree-of-freedom systems, except for the time history.

In determining the damping and response of a system with two or more degrees of freedom, the behavior of the friction when the velocity is zero becomes important. Consider the friction acting in one degree of freedom only of a two-degree-of-freedom system. The friction, when the velocity is zero, is exactly equal in magnitude and opposite in direction to the accelerating forces until the maximum friction is exceeded. Once the maximum friction is exceeded, an acceleration takes place and the velocity becomes other than zero. The usual definition of friction then applies until the velocity becomes zero again. The accelerating forces referred to are the spring, cross coupling, and exterior force, if any.

The equations for the simple two-degree-of-freedom system can be written:

$$m_1\ddot{x}_1 + F + k_1x_1 + a_1x_2 = 0$$
$$m_2\ddot{x}_2 + k_2x_2 + a_2x_1 = 0$$

where a_1 and a_2 are the coupling terms. The effect of the friction can be determined from the energy exchange as shown in phase-plane plots. The plot with no friction is shown in Fig. 1. The relationship between x_1 and x_2 is simply a straight line of slope $dx_1/dx_2 = a_1/k_1$. If we consider x_2 the primary variable, the addition of x_1 as another degree of freedom changes the spring rate but has no effect on the damping. With the addition of static friction to x_1, however, the motion can either add energy to or subtract energy from the x_2 system, respectively, either decreasing or increasing the damping, depending on the relative signs of a_1 and a_2.

The phase-plane plots of Fig. 2 are drawn for very small inertia, m_1—i.e.,

$$m_1 \doteq 0$$

in order to more clearly show the energy relationships due to friction. The energy added to the x_2 system would be

$$\Delta E = \oint a_2 x_1 dx_2$$

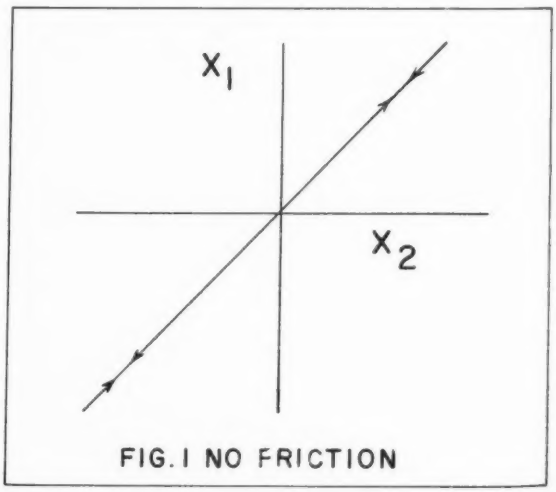

FIG. 1 NO FRICTION

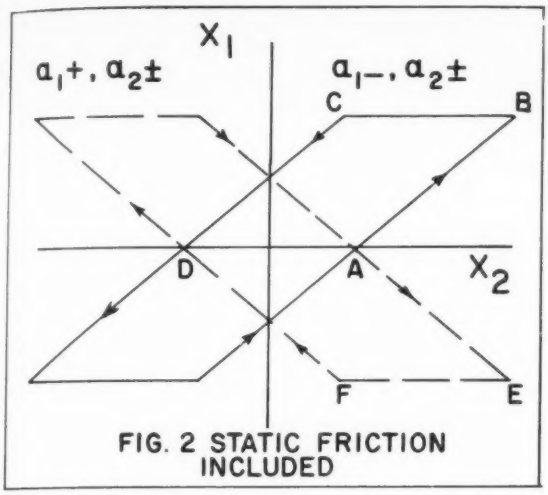

FIG. 2 STATIC FRICTION INCLUDED

where a resultant positive sign for ΔE would indicate energy added and decreased damping. Consider the case where a_1 and a_2 are both negative. From A to B, energy is added to the system. From B to D energy is subtracted in a larger amount (since dx_2 is negative). The resultant effect of the friction is damping, the other half cycle giving identical effect. The opposite would be true if the sign of a_2 were changed to positive. Now consider a_1 and a_2 both positive. From A to E energy is again added to the system and from E to D energy is subtracted with a resulting increase in damping. It is obvious that positive a_1 and negative a_2 would give the reverse. Any addition of energy must come from some outside source such as the air stream in the case of airplane dynamics.

It is interesting to note the part the cross coupling terms play. When the signs are alike, the effect of friction is increased damping, and when they are not alike, negative damping occurs.

Reference

[1] Den Hartog, J. P., *Mechanical Vibrations;* McGraw-Hill Book Company, Inc., New York, 1947.

Vaporization Into a Hypersonic Laminar Boundary Layer

Sinclaire M. Scala*
Research Engineer, Missile and Ordnance Systems Department, General Electric Company, Philadelphia, Pa.

May 27, 1958

Symbols

α	= vaporization coefficient
$\bar{c}_p = \sum_n c_n c_{p_n}$	= frozen gas specific heat
c_n	= mass fraction of species n
$\mathfrak{D}_n$	= diffusion coefficient of species n
$\vec{j}_n = \rho_n \vec{V}_n$	= diffusion flux vector of species n
Le	= Lewis Number
$\dot{m}_i$	= interphase mass transfer
M_n	= molecular weight of species n
p	= static pressure
Pr	= Prandtl Number
R	= universal gas constant
T	= temperature
$\vec{v}_n$	= absolute velocity of species n
$(du_e/dx)_s$	= stagnation point velocity gradient
$\theta = T/T_e$	= dimensionless temperature
ρ	= density
μ	= viscosity
η	= similarity variable

Subscripts

A	= atom
e	= edge of boundary layer
i	= interface between gaseous and condensed phases
eq.	= equilibrium
M	= air molecule
k	= vaporizing species
η	= denotes differentiation with respect to η

A STUDY of surface melting or sublimation requires a detailed consideration of the vaporization processes at the interface between the condensed phase and the gas phase. In Fig. 1 are indicated the various physicochemical processes which occur in the dissociated hypersonic boundary layer, in the mean free path, (shown to exaggerated scale) near a surface undergoing vaporization.

Heterogeneous atom recombination has been considered previously,[1] when mass transfer was absent. However, when vaporization occurs, a new set of constraints is applicable. Although these boundary conditions were utilized recently[2] in considering the problem of a melting surface, few details were given due to space considerations. Because of the current interest in this problem, the surface constraints will be presented here. In particular, the relationship between the interphase mass transfer $\dot{m}_i$, the diffusion rate of the vaporizing species j_{k_i}, the equilibrium vapor pressure $p_{k_{i_{eq.}}}$, and the partial pressure p_{k_i} will be discussed.

A body immersed in a high-temperature, high-velocity stream behaves initially as a pure heat sink. When the surface reaches a critical temperature, selected particles at favorable sites will become detached from the surface lattice structure. During the microscopic collision processes which follow, a number of particles are readsorbed by the surface, while others are transported away by convection and diffusion in the fluid stream.

If one assumes that the forward rate of vaporization from the surface is independent of the partial pressure in the gas phase p_{k_i}, and that the rate of condensation is proportional to the partial pressure p_{k_i}, then kinetic theory yields:

$$\dot{m}_i \cong (\alpha M_k / \sqrt{2\pi M_k R T_i})(p_{k_{i_{eq.}}} - p_{k_i}) \qquad (1)$$

as the net rate of vaporization where p_{k_i} is evaluated within one mean free path from the surface. This equation states that the actual partial pressure p_{k_i} is less than the equilibrium vapor pressure at the interface temperature T_i, when a finite interphase mass transfer occurs.

The interphase mass transfer, by convection and diffusion in the gas phase may be written

$$\dot{m}_i = (\sum_n \rho_n \vec{v}_n)_i = (\rho_A \vec{v}_A + \rho_M \vec{v}_M + \rho_k \vec{v}_k)_i \qquad (2)$$

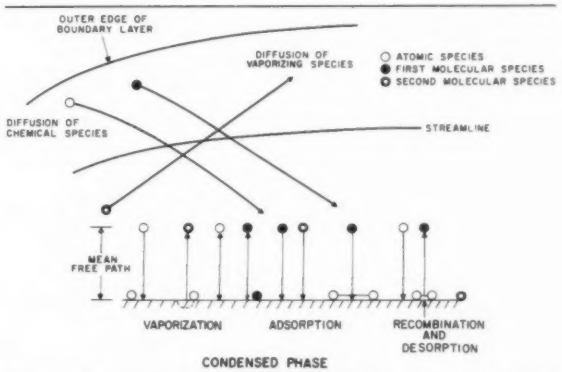

FIG. 1. Schematic model for vaporization in the dissociated hypersonic boundary layer.

* The author wishes to acknowledge the many helpful discussions held with Dr. Guido Vidale of the Aerosciences Laboratory, M.O.S.D., General Electric Company, Philadelphia, Pa.

This analysis is based upon work performed under the auspices of the USAF-B.M.D. contract No. AF 04(645)-24.

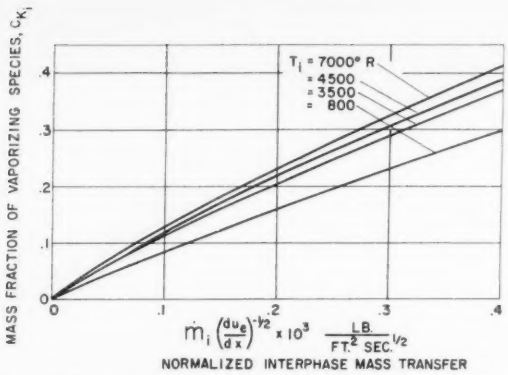

FIG. 2. Mass transfer of vaporizing species in the hypersonic laminar boundary layer. Stagnation point altitude 100,000 ft., Mach Number 20.

Heterogeneous atom recombination requires

$$(\rho_A v_A)_i = -(\rho_M v_M)_i \tag{3}$$

which yields the simple result:

$$\dot{m}_i = (\rho_k v_k)_i \tag{4}$$

Noting that $\sum_n \vec{j}_n = 0$, rearrangement of *either* Eq. (3) or Eq. (4) yields the single constraint:

$$\dot{m}_i = \vec{j}_{ki}(1 - c_{ki})^{-1} \tag{5}$$

Upon introducing Fick's law which is the first approximation to the diffusion flux of the kth species,

$$j_k = -\rho \mathfrak{D}_k (\partial c_k / \partial y) \tag{6}$$

Eq. (5) may also be written in terms of the similarity variables (3)

$$\dot{m}_i = -\sqrt{2\rho_i \mu_i (du_e/dx)_s}(Le/Pr)_i [c_{k\eta i}/(1 - c_{ki})] \tag{7}$$

at the stagnation point of an axially symmetric body. In the steady state, Eqs. (1) and (5) are equal. Hence, if the equilibrium vapor pressure can be determined as a function of temperature, for example, by integrating the Clausius-Clapeyron equation for the particular vaporizing material, and if the vaporization coefficient α of the surface is known, then and only then may one compute the actual partial pressure p_{ki} of the vaporizing species at the interface, a posteriori. If one merely assumes that the equilibrium vapor pressure is equal to the partial pressure, one may actually overestimate the vaporization rate, while solving the boundary-layer equations. The discussion presented above should be critically compared with the recent conclusions of Bauer and Zlotnick.[4]

Because of the similarity between the energy and diffusion equations, for a frozen hypersonic boundary layer, it can be shown that:[3]

$$c_{k\eta_i} \cong (\bar{c}_{pi}/\bar{c}_{pe})\, \theta\eta_i\, c_{ki}/[\theta_i(\bar{c}_{pi}/\bar{c}_{pe}) - 1] \tag{8}$$

Since the author has already correlated the functions $\theta\eta_i$ and $(\bar{c}_{pi}/\bar{c}_{pe})$ as a function of flight speed, altitude, mass-transfer rate, and surface temperature, for the binary mixture, hypersonic laminar boundary layer with mass transfer,[5] Eq. (8), when inserted into eq. (7), yields the typical results shown in Fig. 2 (which appeared previously as Fig. 4 of reference 2). The complete correlation of the function $\dot{m}_i$ as a function of c_{ki} for arbitrary flight conditions is presented in reference 6 and may be utilized in the analysis of arbitrary materials, vaporizing under the particular environmental conditions of interest.

REFERENCES

[1] Scala, S. M., *Hypersonic Heat Transfer to Catalytic Surfaces*, Journal of the Aeronautical Sciences, Vol. 25, No. 4, pp. 273, 274, April, 1958.

[2] Scala, S. M., and Sutton, G. W., *The Two Phase Hypersonic Laminar Boundary Layer—A Study of Surface Melting*, presented at the 1958 Heat Transfer and Fluid Mechanics Institute Symposium, pp. 231–240, June, 1958.

[3] Scala, S. M., *Vaporization into a Hypersonic Laminar Boundary Layer*, General Electric Co., Aerophysics T. M. 84, January, 1958.

[4] Bauer, Ernest, and Zlotnick, Martin, *Evaporation into a Boundary Layer*, AVCO RAD Report, May, 1958.

[5] Scala, S. M., *Transpiration Cooling in the Hypersonic Laminar Boundary Layer* (to be published).

[6] Scala, S. M., and Vidale, G., *Vaporization Processes in the Hypersonic Laminar Boundary Layer*, General Electric Co., Aerophysics Research Memorandum No. 14, July, 1958.

On Simplified Fuselage-Structure Stress Distributions

W. R. Jensen
Structural Methods Engineer, Grumman Aircraft Engineering Corporation, Bethpage, Long Island, N.Y.

April 3, 1958

IT IS GENERALLY AGREED that, in order to obtain an accurate stress distribution in a semimonocoque structure, a rather complex idealized structure is required. This is no longer an insurmountable obstacle to stress analysts, thanks to the large digital computers now available. Many engineers doing this work nevertheless believe that such problems should still be kept as simple as possible, avoiding in this way excessive preparation of data, increased possibility of making errors, and voluminous answers. However, little information is available as to what constitutes the minimum in an adequate idealization. The present note attempts to shed some light on this matter.

A well-known technique employed in idealizing these semimonocoque structures consists of combining the stringers and skin into a smaller number of equivalent stringers and combining the frames into a smaller number of equivalent frames. The skin in between is assumed to be a membrane which can carry shear only. In an attempt to decide how many equivalent stringers should be used, several such idealizations of an NACA test cylinder[1] were made, and solutions were obtained analytically. A comparison of these results with a more comprehensive analysis

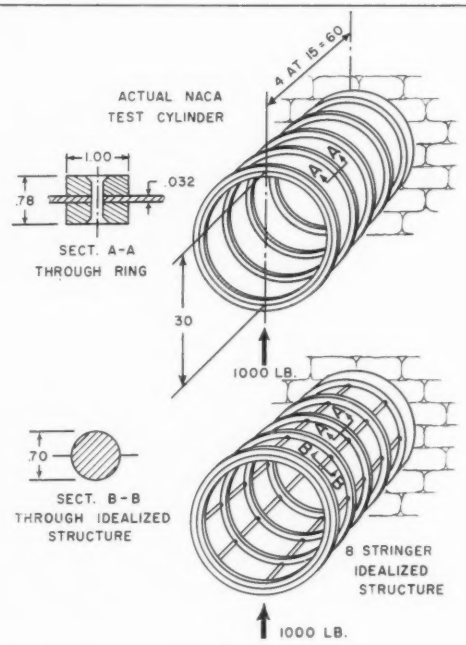

FIG. 1.

and with test data[1] indicates that a surprisingly small number of equivalent stringers may be adequate for the design of most fuselages.

The actual structure analyzed (see Fig. 1) consisted of a radially loaded ring supported by a four-bay cantilever shell. The shell had no stringers and the idealization consisted of considering the longitudinal load carrying material to be concentrated at six or eight symmetrically placed locations at the skin line (see Fig. 1). The more comprehensive analysis[1, 3] considers the longitudinal bending material to be continuously distributed around the shell. This latter analysis thus shows what can be expected when the number of stringers of the idealized structure is increased indefinitely.

If the loaded ring of the structure were rigid, the stress distribution in the shell would be according to engineering beam theory. Deformation of the loaded end ring induces self balancing loads in the shell. These redundant distributions can be found by using a least-work method[2] and superimposed on the engineering beam-theory distribution. Bending energy of the loaded ring and reinforcing rings, shear energy of the skin, and energy due to the longitudinal bending stresses (stringer stresses) were considered.

The six- and eight-stringer results are compared graphically with the more comprehensive solution, with test data, and with engineering beam-theory distributions in Figs. 2, 3, and 4. The ring bending moments for the six-stringer, eight-stringer, and distributed-stringer analyses are so close that they can only be plotted as single curves (see Fig. 2). The test data are in excellent agreement.

In Fig. 3 the curves represent the longitudinal bending stress for the distributed-stringer analysis. The stresses for the six- and eight-stringer analyses are plotted at their proper locations; as can be seen, faired curves through these points would agree very well with the distributed-stringer result. There are few test data for this comparison, however, excellent agreement is shown for the data available.

The shear-stress distributions in the shell are shown in Fig. 4. The six- and eight-stringer cases are step curves as a consequence

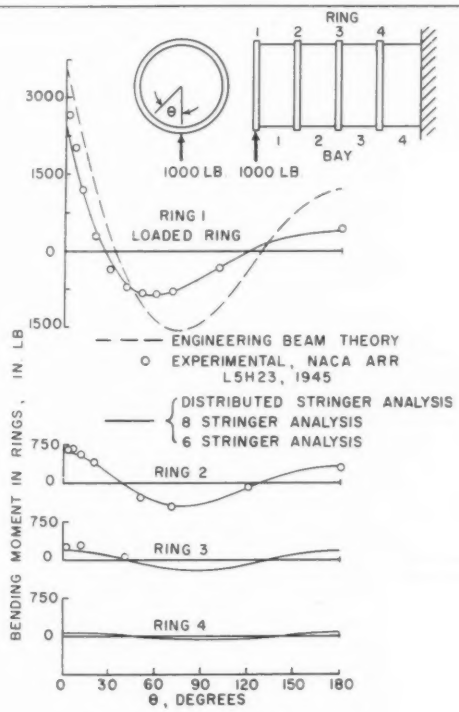

FIG. 2. Ring bending moment.

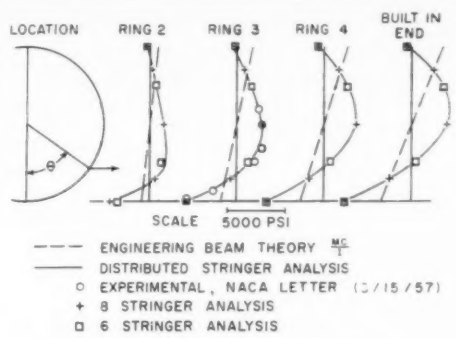

FIG. 3. Shell longitudinal bending stress.

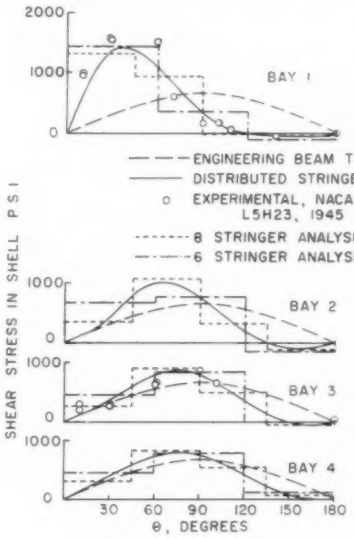

FIG. 4. Shear stress in shell.

of the idealization. Within this limitation, the agreement is satisfactory.

It can be concluded that, at least for a structure of the proportions and type of loading considered here, a very much simplified idealized structure with a small number of equivalent stringers will give satisfactory design information.

REFERENCES

[1] Kuhn, Paul, Duberg, John E., and Griffith, George E., *The Effect of Concentrated Loads on Flexible Rings in Circular Shells*, NACA, ARR No. L5H23, 1945.

[2] Wehle, L. B., and Lansing, Warner, *A Method for Reducing the Analysis of Complex Redundant Structures to a Routine Procedure*, Journal of the Aeronautical Sciences, Vol. 19, No. 10, pp. 677–684, October, 1952.

[3] Hoff, N. J., *Stresses in a Reinforced Monocoque Cylinder Under Concentrated Transverse Loads*, J. Appl. Mech., Vol. 66, pp. A-235–A-239, Dec., 1944.

Further Remarks on the Torsional Rigidity of Thermally Stressed Wings

R. L. Bisplinghoff
Professor of Aeronautical Engineering, Massachusetts Institute of Technology, Cambridge, Mass.

June 5, 1958

SEVERAL AUTHORS—e.g., references 1 through 6—have pointed up the important influence of finite deformations and initial

imperfections on the torsional rigidity of thermally stressed wings. The present brief note is intended primarily to communicate a comparison of theory with experiment for finitely twisted flat plates subjected to a chordwise temperature distribution. Referring to Fig. 1, suppose that a flat plate of thickness h, chord $2b$, and length $2a$ ($a \gg b$) with a chordwise distribution of temperature described by the even function $T(x_2)$ undergoes finite twisting deformations due to a torque, M_t. It is known that when warping restraint is neglected, the torque is related to the twist per unit length, θ, by

$$M_t = \theta\left[4bD(1-\gamma) + \int_{-b}^{+b} N_{11}(x_2)x_2^2 dx_2\right] \tag{1}$$

where $D = Eh^3/12(1-\gamma^2)$ is the flexural rigidity, γ is Poisson's ratio, E is Young's modulus and $N_{11}(x_2)$ is the stress resultant in the x_1 direction. It can be shown that the stress resultant has the simple form[7]

$$N_{11}(x_2) = (Eh\theta^2/6)(3x_2^2 - b^2) + (\alpha Eh/2b)\left[\int_{-b}^{b} T(x_2)dx_2 - 2bT(x_2)\right] \tag{2}$$

where α is the coefficient of thermal expansion. Assuming $T(x_2) = T_0 + \Delta T f(x_2)$, we obtain by substituting Eq. (2) into Eq. (1),

$$[M_t/4bD(1-\gamma)\theta] = 1 - (\Delta T/\overline{\Delta T}) + (4/15)(1+\gamma)(b^4\theta^2/h^2) \tag{3}$$

where $\overline{\Delta T}$ is the temperature differential required to produce thermal buckling.

$$\overline{\Delta T} = bh^2\Big/3\alpha(1+\gamma)\left[\int_{-b}^{b} f(x_2)x_2^2 dx_2 - (b^2/3)\int_{-b}^{b} f(x_2)dx_2\right] \tag{4}$$

The relative influence of the temperature differential, ΔT, and twist rate, θ, is indicated by the right-hand side of Eq. (3).

In Fig. 2, there is shown a comparison of Eq. (3) with experiments[7] in which a 7075 T-6 aluminum alloy flat plate is twisted under the three conditions of $\Delta T/\overline{\Delta T} = 0$, 0.4 and 1. A chordwise temperature distribution was produced by using identical line heat sources along the edges and a line heat sink along the mid-chord. The temperature distribution obtained in this way is shown by the sketch of Fig. 1.

In general, close agreement between Eq. (3) and the twisting experiments was found provided the initial imperfections were essentially eliminated and provided the thermal buckling temperature differential, $\overline{\Delta T}$, was obtained with precision. The comparison shown in Fig. 2 represents results obtained by giving careful attention to these two factors. Although reasonable agreement was found to exist between Eq. (4) and the experimentally obtained value of $\overline{\Delta T}$, the latter was used in preparing the solid lines in Fig. 2.

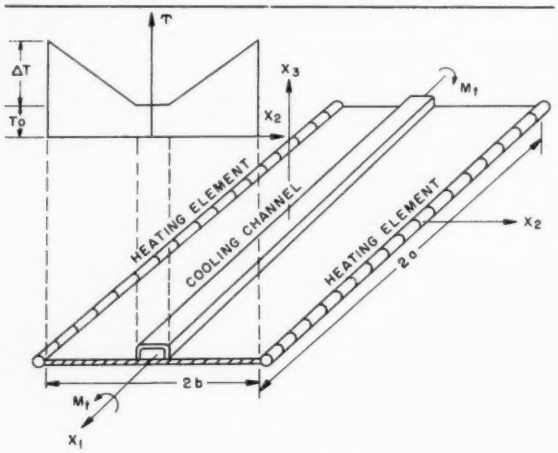

FIG. 1. Experimental model.

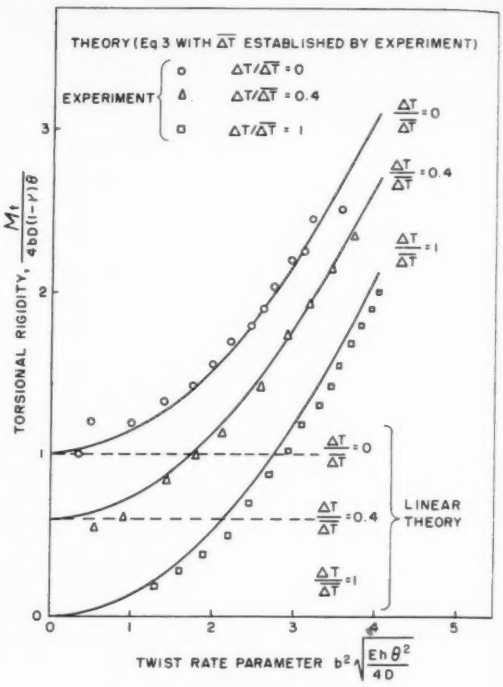

FIG. 2. Experiment and theory.

REFERENCES

[1] Bisplinghoff, R. L., and Dugundji, John, *Influence of Aerodynamic Heating on Aeroelastic Phenomena*, Presented at the Symposium on Structural Problems of High-Speed Flight at the Royal College of Aeronautics, Cranfield, England, August, 1956.

[2] Singer, J., and Hoff, N. J., *Effect of Changes in Thermal Stresses Due to Large Deflections on the Torsional Rigidity of Wings*, Journal of the Aeronautical Sciences, Readers' Forum, Vol. 24, No. 4, pp. 310, 311, April, 1957.

[3] Biot, M. A., *Influence of Thermal Stresses on the Aeroelastic Stability of Supersonic Wings*, Journal of the Aeronautical Sciences, Vol. 24, No. 6, pp. 418–420, 429, June, 1957.

[4] Heldenfels, R. R., and Vosteen, L. F., *Approximate Analysis of Effects of Large Deflections and Initial Twist on Torsional Stiffness of a Cantilever Plate Subjected to Thermal Stresses*, NACA TN 4067, August, 1957.

[5] Singer, J., *The Effect of Amplitude on the Torsional Vibrations of Solid Wings Subjected to Aerodynamic Heating*, Journal of the Aeronautical Sciences, Vol. 24, No. 8, pp. 420–422, August, 1957.

[6] Kochanski, S. L., and Argyris, J. H., *Some Effects of Kinetic Heating on the Stiffness of Thin Wings*, Aircraft Engineering, October, 1957.

[7] Bisplinghoff, R. L., *The Finite Twisting and Bending of Heated Elastic Ligting Surfaces*, Mitteilung Nr. 4, Aus dem Institut für Flugzeugstatik und Flugzeugbau, an der Eidgenössischen Technischen Hochschule in Zürich, 1957.

Polynomial Expressions for the Specific Heat and Prandtl Number of Air

Donald W. Boekemeier

Aerothermodynamic Engineer, Bendix Products Division—Missiles, Bendix Aviation Corporation, Mishawaka, Ind.

May 22, 1958

THE PURPOSE of this note is to present polynomial expressions and their associated coefficients for the specific heat and the third root of the Prandtl Number of air as functions of temperature.

SYMBOLS

C_p = specific heat of air
D = coefficients in polynomial expression of specific heat
E = coefficients in polynomial expression of $(Pr)^{1/3}$

Table I

Coefficients for Polynomial Expression of Specific Heat

Temp. Range = 300°-1200°R

Pressure = 0.10 ATM

D_0 = +3.4418923
D_1 = +4.8331520 x 10^{-4}
D_2 = -1.6621892 x 10^{-6}
D_3 = +2.4380548 x 10^{-9}
D_4 = -1.3228604 x 10^{-12}
D_5 = +2.4858005 x 10^{-16}
Maximum Error = 0.04%

Pressure = 1.00 ATM

D_0 = +3.5684716
D_1 = -2.0430912 x 10^{-4}
D_2 = -1.4616892 x 10^{-7}
D_3 = +8.1441984 x 10^{-10}
D_4 = -4.9535650 x 10^{-13}
D_5 = +9.0255235 x 10^{-17}
Maximum Error = 0.08%

Pressure = 4.00 ATM

D_0 = +4.0498617
D_1 = -2.8656884 x 10^{-3}
D_2 = +5.8753994 x 10^{-6}
D_3 = -5.9300099 x 10^{-9}
D_4 = +3.1877628 x 10^{-12}
D_5 = -6.8911711 x 10^{-16}
Maximum Error = 0.15%

Temp. Range = 1200°-3000°R

Pressure = 0.10, 1.00 and 4.00 ATM

D_0 = +3.2240709
D_1 = +2.5453604 x 10^{-4}
D_2 = +2.5222882 x 10^{-7}
D_3 = -1.2013920 x 10^{-10}
D_4 = +1.7003460 x 10^{-14}
D_5 = 0.0000000
Maximum Error = 0.50%

Temp. Range = 3000°-5400°R

Pressure = 0.10 ATM

D_0 = +6.9192916 x 10^{+1}
D_1 = -9.3467711 x 10^{-2}
D_2 = +5.2484476 x 10^{-5}
D_3 = -1.4268396 x 10^{-8}
D_4 = +1.8487752 x 10^{-12}
D_5 = -8.7463704 x 10^{-17}
Maximum Error = 1.50%

Pressure = 1.00 ATM

D_0 = +3.0927388 x 10^{+1}
D_1 = -3.8410018 x 10^{-2}
D_2 = +2.1331684 x 10^{-5}
D_3 = -5.6894998 x 10^{-9}
D_4 = +7.2132357 x 10^{-13}
D_5 = -3.3329913 x 10^{-17}
Maximum Error = 0.70%

Pressure = 4.00 ATM

D_0 = +2.2030860 x 10^{+1}
D_1 = -2.5433536 x 10^{-2}
D_2 = +1.3943727 x 10^{-5}
D_3 = -3.6624308 x 10^{-9}
D_4 = +4.5962131 x 10^{-13}
D_5 = -2.1299845 x 10^{-17}
Maximum Error = 0.35%

$(Pr)^{1/3}$ = Prandtl Number to the one-third power
R = universal gas constant, 1716.5 ft. lb.f/slug °R.
T = temperature, °R.

Since many heat-transfer problems are presently being solved by electronic computing machines, it is necessary that the thermodynamic and transport properties of air be either stored in the machine or calculated from equations. Properties such as the thermal conductivity and viscosity have accepted expressions as a function of temperature, for instance, reference 1. The specific heat and Prandtl Number do not have expressions commonly given; they are usually just tabulated.

Before the coefficients for these two expressions are determined, it is necessary to resolve what are the more widely accepted and agreed upon data presently available. After reviewing references 1 and 2, it is found that reference 1 accounts for the dissociation of the air at the higher temperatures whereas reference 2 does not. All other investigation verifies the fact that dissociation has a major effect on the properties of air at high temperatures and that the data given in reference 1 are the best information presently available in the temperature range 200 to 5,400°R.; therefore, these data are used for determination of the coefficients.

Three different constant pressures are taken for the determination of the coefficients for the specific-heat polynomial expression, the pressures being 0.10, 1.00 and 4.00 atm. The data are divided into three temperature ranges, and individual polynomial expressions are written for each pressure in these ranges. The ranges in which these data are divided are: 300–1,200°R., 1,200–3,000°R, and 3,000–5,400°R. All three pressures have nearly the same value of specific heat at a given temperature in the middle region, therefore, one set of coefficients suffices for the three.

The polynomial expression taken is of the general form:

$$C_p/R = D_0 + D_1T + D_2T^2 + D_3T^3 + D_4T^4 + D_5T^5$$

The constant coefficients for each pressure and temperature range are listed in Table 1 with the maximum deviation error indicated. It must be remarked here that even though the coefficients listed are for a certain temperature range, this does not sharply limit the use of these coefficients to this region. Their usage may be extended, but as it is extended the deviation error becomes larger, so it is advisable to limit this extension to 100°.

Table II

Coefficients for Polynomial Expression of Prandtl Number

Temp. Range = 300°-1800°R

Pressure = 1.00 ATM
E_0 = +0.93790000
E_1 = -0.95038890 x 10^{-4}
E_2 = -0.49383340 x 10^{-7}
E_3 = +0.16898148 x 10^{-9}
E_4 = -0.10339506 x 10^{-12}
E_5 = +0.20233196 x 10^{-16}
Maximum Error = 0.10%

Data for the Prandtl Number from reference 1 are given only for atmospheric pressure over the temperature range 300°–1,800° R. Only one set of coefficients is used for the entire range.

The polynomial expression taken is of the general form:

$$(Pr)^{1/3} = E_0 + E_1T + E_2T^2 + E_3T^3 + E_4T^4 + E_5T^5$$

The constant coefficients for the given pressure and temperature range are listed in Table 2 with the maximum error indicated. It might be noted that the indicated maximum error is less than the accuracy of the tabulated data source.

References

[1] Thermodynamics Section, National Bureau of Standards, *Tables of Thermal Properties of Gases*, U.S. Department of Commerce, Circular 564, November, 1955.

[2] Keenan, Joseph H., and Kaye, Joseph, *Gas Tables*, John Wiley & Sons, Inc., New York, 1950.

On a Complementary Energy Principle in Linear Thermoelasticity*

G. Herrmann
Associate Professor of Civil Engineering, Institute of Flight Structures, Columbia University, N.Y.
June 9, 1958

THE EQUATIONS of linear thermoelasticity, using in part the formulation given recently by Biot,[1] consist essentially of the following set of four equations

$$\tau_{ij,j} - \beta\theta_{,i} = 0 \tag{1}$$

$$\theta_{,i} + pTs_i/k = 0 \tag{2}$$

$$(u_{i,j} + u_{j,i}) = 2W_{,\tau_{ij}} \tag{3}$$

$$s_{i,i} + \beta u_{i,i} = -W_{,\theta} \tag{4}$$

Use is made of the summation convention. A comma preceding a subscript indicates differentiation with respect to that variable, except that i (or j) after a comma stands for differentiation with respect to the Cartesian coordinate x_i (or x_j).

In the above equations, $\tau_{ij} = \tau_{ji}$ denotes the components of stress if the temperature increment θ above a reference absolute temperature T vanishes. The total stress, in general, is thus $\tau_{ij} - \beta\theta\delta_{ij}$ (δ_{ij} is the Kronecker delta). Further, u_i and s_i indicate the components of solid and entropy displacement, respectively, k is the coefficient of heat conduction, and $p = d/dt$ is a time operator. W is Biot's thermoelastic potential, which consists of the sum of the isothermic mechanical energy (expressed here as a quadratic function of the stresses τ_{ij}) and the term $c\theta^2/2T$, where c is the specific heat of the unit volume in the absence of elastic deformation. It is recalled that the entropy displacement s_i is related to entropy s by the equation $s = -s_{i,i}$.

Eq. (1) represents the stress equation of equilibrium, in which the body force was omitted for simplicity. Eq. (2) is a particular form of the heat conduction equation. Eq. (3) is the (isothermal) stress-displacement relation (Hooke's law), and Eq. (4) may be called the "thermal" stress-displacement relation.

Biot has shown in reference 1 that Eqs. (1) and (2) may be derived by a variational procedure if the validity of Eqs. (3) and (4) is assumed. Since Biot applied the variation to the displacements u_i and s_i, his procedure appears to correspond to Green's method.

Thus, the question may be asked whether it might not be feasible to establish, for thermoelasticity, an associated principle of complementary energy which would then correspond to Castigliano's method in elasticity. The availability of such an extremum principle could be of considerable significance in the development of approximate methods of thermoelastic structural analysis.

In what follows, it is shown that it is, in fact, possible to formulate such a principle complementary to Biot's procedure. For the sake of brevity, the principle will not be presented here in its most general form. This applies in particular to the restriction in the type of boundary conditions.

We consider the functional

$$I = \int_V [W + D]dV - \int_A [u_i(F_i - \beta\theta_i) - s_i\theta_i]dA \tag{5}$$

and set its first variation δI equal to zero by varying τ_{ij} and θ. D is Biot's dissipation function, which can be expressed as a quadratic form of the temperature gradient $\theta_{,i}$ using Eq. (2), such that this equation may also be written in the form

$$D_{,\theta_{,i}} + s_i = 0 \tag{2'}$$

In Eq. (5) θ_i stands for θn_i, where n_i is the outward unit vector normal to the boundary A. F_i is the boundary traction in the isothermal case ($\theta = 0$). The 2nd integral in Eq. (5) extends over the surface A bounding a volume V. It can be transformed by means of the relations

$$\int_A u_i(F_i - \beta\theta_i)dA = \int_V [u_i(\tau_{ij,j} - \beta\theta_{,i}) + (1/2)(u_{i,j} + u_{j,i})\tau_{ij} - u_{i,i}\beta\theta]dV \tag{6}$$

$$\int_A s_i\theta_i dA = \int_V [s_i\theta_{,i} + s_{i,i}\theta]dV \tag{7}$$

It is assumed for simplicity that displacements u_i and s_i are prescribed on A.

The variation δI takes then the form

$$\delta I = \int_V \{[W_{,\tau_{ij}} - (1/2)u_{i,j} - (1/2)u_{j,i}]\,\delta\tau_{ij} + (W_{,\theta} + s_{i,i} + \beta u_{i,i})\delta\theta - u_i(\delta\tau_{ij,j} - \beta\delta\theta_{,i}) + (D_{,\theta_{,i}} + s_i)\,\delta\theta_{,i}\}dV \tag{8}$$

The last 2 terms of the integrand vanish because of Eqs. (1) and (2), and the first 2 terms yield, as required, Eqs. (3) and (4).

The complementary energy principle associated with Biot's formulation is thus established. It states, in words, that among all possible states of stress and temperature distribution which satisfy the equations of equilibrium and heat conduction in the interior of the body and the prescribed boundary conditions on its surface, the actually occurring states relate the stresses and the temperature to the solid and entropy displacements in such a manner as to make I stationary.

It was pointed out above that Biot's variational procedure appears to correspond to Green's method. It will be shown by the present author elsewhere that this procedure is actually a mixed one. This is due to the fact that the equation of heat conduction turns out to be not an equilibrium-type equation but a relation of the force-displacement type. The force in this case is the quantity conjugate to the entropy displacement.

It will be shown further that it is possible to establish, for thermoelasticity, a more general variational theorem on both displacements and stresses, as was done by Reissner[2] for isothermal elasticity ($\theta = 0$), which yields Eqs. (1) through (4) by means of a variational procedure. It is possible to show, moreover, as was done by Reissner[3] again for isothermal elasticity, that in the variational theorem for displacements (Green's method) one is concerned with a minimum problem while in the variational theorem for stresses (Castigliano's method) one is concerned with a maximum problem.

In conclusion it may be mentioned that extensions of the foregoing theorems to anisotropic bodies and to systems subjected to body forces are possible. Moreover, all of the above applies not only to the thermoelasticity but also to elasticity of porous materials because of the analogy established by Biot.[1] Furthermore, the new variational procedures may prove useful also in the particular case of purely thermal problems, if Biot's[4] approach to heat flow analysis is adopted.

REFERENCES

[1] Biot, M. A., *Thermoelasticity and Irreversible Thermodynamics*, J. Appl Phys., Vol. 27, No. 3, pp. 240–253, March, 1956.

[2] Reissner, E., *On a Variational Theorem in Elasticity*, J. Math. and Phys. Vol. 29, pp. 90–95, 1950.

[3] Reissner, E., *On Variational Principles in Elasticity*, Symposium on the Calculus of Variations and Its Applications, Am. Math. Soc., April, 1956.

[4] Biot, M. A., *New Methods in Heat Flow Analysis With Application to Flight Structures*, Journal of the Aeronautical Sciences, Vol. 24, No. 12, pp. 857–873, December, 1957.

* This investigation was supported by the USAF, through OSR of the ARDC under Contract AF 18(600)-1247.

Further Numerical Data on Blunt Bodies

H. Melvin Lieberstein
*Physics Section, Convair, A Division of General Dynamics Corporation, San Diego, Calif.**
June 2, 1958

AN ADVANTAGE of computing hypersonic flows over wind-tunnel measurement is the ease with which very high Mach

* The numerical work on this note was completed while the author was at The Ramo-Wooldridge Corporation.

Number cases can be treated. Of course, approach-flow Mach Number is an input parameter and the routine described in reference 1 includes the possibility of computing flows with an effective γ_1 defined by $h = [\gamma/(\gamma - 1)]\,(p/\rho)$, in the shock layer different from the approach flow—i.e., for $\gamma \neq \gamma_1$. The routine mentioned was tailored for close approximation of dissociation effects, but no data were quoted for dissociated flows in reference 1, and we wish to supply such data here.

Further, one is interested in current design criteria, and, in particular, we wish to test the merit of the modified Newtonian theory of Prof. L. Lees. We therefore submit the following data for four cases.

(r, z) = body coordinates
$\theta = \arctan v/u$ = inclination of body to approach-flow normal
M = Mach Number at point (r, z) on body
$C = \dfrac{P - P_1}{P_{max} - P_1}$ = ratio of pressure coefficient at a given point on body to pressure coefficient at stagnation

Case 1—Shock $(z + z_0)^2 = (M^2 - 1)\,(M^2 + r^2)$, $M = 5.8$, $\gamma = \gamma_1 = 1.4$; body (see Fig. 4 of reference 1) is approximately spherical shape for which data are given in detail in the reference; $\kappa h = .1585$.

Case 2—Shock $(z + z_0)^2 = 0.8\,(0.8 + r^2)$, $M = 5.8$, $\gamma = \gamma_1 = 1.4$; body (see Fig. 5 of reference 1) is a rounded cone; $\kappa h = 0.174$.

Case 3—Shock $(z + z_0)^2 = (M^2 - 1)\,(M^2 + r^2)$, $M = 20$, $\gamma_1 = 1.4$, $\gamma = 1.17$ (intended to approximate the gas law from real-gas tables for density at 100,000 ft. altitude); body is nearly spherical; $\kappa h = 0.0633$.

Case 4—Shock $(z + z_0)^2 = (M^2 - 1)\,(M^2 + r^2)$, $M = 1.2$, $\gamma = \gamma_1 = 1.4$; only two points on the body are given.

It will be seen that the modified Newtonian law, $C = \cos^2\theta$ is for Case 1, about 3 per cent high; Case 2, about 3 per cent low; Case 3, 6–7 per cent high; and Case 4, over 20 per cent high in the subsonic region.

TABLE 1
Case 1

r	z	M	φ (radians)	C
.04382	.11235	.07749	.0559	.9956
.10747	.11972	.18927	.1517	.9746
.16623	.13128	.29334	.2354	.9407
.22169	.14690	.39036	.3124	.8979
.24048	.15341	.42317	.3370	.8813
.28577	.17080	.50192	.3985	.8383
.33204	.19241	.58352	.4601	.7892
.35159	.20198	.61579	.4836	.7689
.42779	.24671	.74671	.5773	.6835
.45222	.26312	.78791	.6067	.6559
.51961	.31386	.90761	.6845	.5767
.568	.356	1.	.738	.5119

TABLE 2
Case 2

r	z	M	φ (radians)	C
.04278	.11026	.0799	.0483	.9954
.11151	.12479	.2575	.2255	.9538
.23554	.15325	.4086	.3569	.8888
.30722	.18362	.5072	.4402	.8352
.34316	.20139	.5508	.4763	.8093
.38213	.22242	.5938	.5114	.7829
.43428	.25320	.6447	.5519	.7504
.5152	.3061	.7102	.6032	.7076
.6123	.3769	.7699	.6493	.6681
.7089	.4530	.8208	.6779	.6340
1.14	.84	1.	.785	.512

TABLE 3
Case 3

r	z	M	φ (radians)	C
.02819	.05455	.0475	.0285	.9987
.07838	.05768	.1320	.0922	.9900
.13238	.06444	.2224	.1560	.9716
.16842	.07090	.2822	.1979	.9547
.20482	.07901	.3422	.2395	.9340
.21546	.08175	.3594	.2514	.9275
.23754	.08784	.3949	.2760	.9132
.27093	.09811	.4484	.3113	.8898
.33230	.12009	.5478	.3727	.8406
.40853	.15368	.6636	.4443	.7761
.47100	.18650	.7429	.4975	.7289
.72868	.37768	1.1053	.7372	.5058

TABLE 4
Case 4

r	z	M	φ (radians)	C
.06703	.3740	.2949	.0630	.9567
.19667	.4160	.6149	.5024	.6155

REFERENCE

1 Garabedian, P. R., and Lieberstein, H. M., *On the Numerical Calculation of Detached Bow Shock Waves in Hypersonic Flow*, Journal of Aeronautical Sciences, Vol. 25, No. 2, pp. 109–118, February, 1958.

Errata—"On Unsteady Interaction Between a Weak Thermal Layer and a Strong Plane Oblique Shock"*

C. T. Chang
Research Fellow, Hydrodynamics, Harvard University, Cambridge, Mass.

June 13, 1958

ON PAGE 319, sentence after Eq. (2.6), "In terms of the polar coordinates, Eq. (2.5) becomes," instead of Eq. (2.4).

On page 321, Eq. (3.10), the differential operator should be $[\rho(\partial p/\partial\rho)]$ instead of $[\rho(\partial p/\rho)]$.

On page 322, Eq. (3.19), the factors appearing in the numerator and denominator should be

$$(1 - \alpha\varepsilon^{-i\phi})\zeta e^{i\phi} \text{ and } (1 + \alpha\varepsilon^{-i\phi})\zeta e^{i\phi}$$

instead of

$$(1 - \alpha\varepsilon^{i\phi})\zeta e^{i\phi} \text{ and } (1 + \alpha\varepsilon^{i\phi})\zeta e^{i\phi}$$

respectively.

* Journal of the Aeronautical Sciences, Vol. 25, No. 5, pp. 317-323, May, 1958.

Similar Solution of a Laminar Boundary Layer With Rotational Free Stream

Franklin D. Hains*
Aerodynamicist, Research Division, Bell Aircraft Corporation, Buffalo, N.Y.
June 6, 1958

THE BOUNDARY-LAYER EQUATION for flow over a curved or plane surface is

$$\psi_y\psi_{yx} - \psi_x\psi_{yy} = -\rho^{-1}p_x + \nu\psi_{yyy} \tag{1}$$

where ψ is the stream function, ρ the density, p the pressure, and ν the kinematic viscosity. x and y are the coordinates measured along the surface and normal to the surface, respectively.

A solution will be given which satisfies the boundary conditions

$$y = 0: \quad u = v = 0, \qquad y = \infty: \quad u_y = \alpha \tag{2}$$

in such a way that for $x > 0$ the slope of the streamlines is everywhere finite. In order to avoid a controversy similar to that between Glauert[1] and Li[2] over the correct boundary condition at $\eta = \infty$, no attempt is made to describe the "free stream" in the region $x < 0$ ahead of the body. A typical streamline and velocity profile for the accelerating flow is shown in Fig. 1.

Introducing

$$\eta = 2\alpha^{1/3}\nu^{-1/3}x^{-1/3}y, \quad \psi = 3\alpha^{1/3}\nu^{2/3}x^{2/3}f(\eta) \tag{3}$$

Eq. 1 is transformed into

$$(f'^2/2) - ff'' = [(f'^2/2) - ff'']_{\eta=\infty} + f''' \tag{4}$$

and Eq. (2) becomes

$$\eta = 0: \quad f = f' = 0, \qquad \eta = \infty: \quad f'' = 1/12 \tag{5}$$

The solution to Eq. (4) is obtained in the form of a power series near $\eta = 0$ and an asymptotic expansion for large values of η. The asymptotic expansion is taken to be

$$f = f_1 + f_2 + \ldots, \quad f_1 > f_2 > f_3 > \ldots \tag{6}$$

The first term, suggested by Eq. (5) is

$$f_1 = (\eta^2/24) + B\eta + E \tag{7}$$

Because $f(\infty) = f_1(\infty)$, Eq. (4) becomes

$$f''' - ff'' + (1/2)[B^2 - (E/6) - f'^2] = 0 \tag{8}$$

As a first approximation,

$$f = f_1, \quad f' = f_1', \quad f'' = f_1'' + f_2'', \quad f''' = f_2''' \tag{9}$$

and Eq. (8) becomes

$$f_2''' + [(\eta^2/24) + B\eta + E]f_2'' = 0 \tag{10}$$

* Presently, Aerodynamicist, Boeing Scientific Research Laboratory, Seattle, Wash.

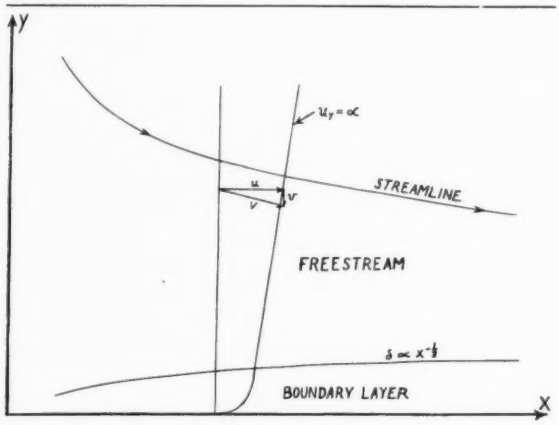

FIG. 1. Boundary layer with rotational free stream.

Integrating,

$$\left.\begin{aligned} f_2'' &= e^{-\xi}, \quad f_2' = \int_{\infty}^{\eta+12B} e^{-r\lambda^2 - t\lambda - q}\, d\lambda \\ f_1 &= (\eta + 12B)e^{-q}\, f_2' - \int_{\infty}^{\eta+12B} \lambda e^{-r\lambda^2 - t\lambda - q}\, d\lambda \end{aligned}\right\} \tag{11}$$

where

$$\left.\begin{aligned} q &\equiv 12B(4B^2 - E), \quad r = 1/72 \\ t &\equiv E - 6B^2, \quad \xi \equiv (\eta^2/24) + B\eta + E \end{aligned}\right\} \tag{12}$$

By repeated partial integrations, an asymptotic expansion is obtained for f_2 so that the first two terms of Eq. (6) become

$$f = f_1 + f_2 = \xi + \{\xi^{-2} - [(\eta/4) + 3B]\xi^{-4} + [39(\eta + 12B)^2 - 2E + 12B^2](\xi^{-6}/6) - \ldots\} \times \exp[(-\eta^3/72) - B\eta^2 - E\eta] \tag{13}$$

The power series development near $\eta = 0$ is

$$f = (A\eta^2/2!) + (C\eta^3/3!) - (A^2\eta^4/2!4!) + [A^2 - (4/3)AC](\eta^5/5!) + [(7/8)A^3 - C^2 + 3AC](\eta^6/6!) + [(133/30)A^2C - (21/5)A^3 + 3C^2](\eta^7/7!) + \ldots \tag{14}$$

where $C \equiv (E/12) - (B^2/2)$

The power series Eq. (14) and the asymptotic expansion Eq. (13) are joined at a suitable point $\eta = \eta^*$ where both series are valid. The three constants A, B, and E are found by making the values of f, f', and f'' of both series equal at $\eta = \eta^*$. The higher derivatives are then automatically satisfied.

REFERENCES

[1] Glauert, M. B., *The Boundary Layer in Simple Shear Flow Past a Flat Plate*, Journal of the Aeronautical Sciences, Readers' Forum, Vol. 24, No. 11, pp. 848, 849, November, 1957.

[2] Li, Ting Yi, *Author's Reply*, Journal of the Aeronautical Sciences, Readers' Forum, Vol. 24, No. 11, p. 849, 850, November, 1957.

Some Experiments on Effects of Yaw on Boundary-Layer Development in Supersonic Cone Flow*

D. G. DeCoursin and W. S. Bradfield
Rosemount Aeronautical Laboratory, University of Minnesota, Rosemount, Minn.; and Senior Staff Scientist, Scientific Research Laboratory, Convair, A Division of General Dynamics Corp., San Diego, Calif.; Respectively
June 16, 1958

THIS NOTE is a summary of a study of the effect of small angles of yaw on boundary-layer development on a cone[1] including turbulent boundary-layer data previously obtained in connection with a more general experimental program.[2, 3] Details of the experiments are given in references 1 and 2.

In Fig. 1 the effect of yaw on the laminar velocity boundary layer on the windward side of a cone is presented. It can be seen that at the meridianal plane as the angle of yaw increases the boundary layer thins and the velocity gradient becomes steeper.

On the leeward meridianal plane (Fig. 2), however, the effect is markedly to increase the thickness of the boundary layer and even to change the apparent character of the boundary layer from laminar to turbulent. This effect has occurred already as the angle of attack is changed from zero to 1.2° as shown in the figure.

By plotting the shape parameter for these apparently turbulent boundary-layer profiles for comparison with other profiles which were taken from the normally turbulent boundary layer at zero yaw, it was found[3] that the shape parameters thus determined fell together with normal turbulent boundary-layer shape parameters. Therefore, one inclines to the belief that normal turbulent

* The experiments presented here were carried out under Contract Number AF18(600)-384, sponsored by the USAF, Office of Scientific Research.

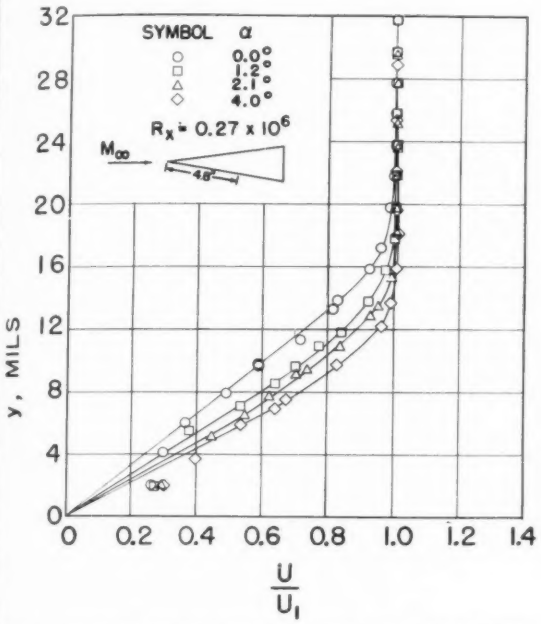

FIG. 1. Effect of yaw on laminar velocity profiles on the windward surface of a 15° cone at $M_\infty = 2.73$.

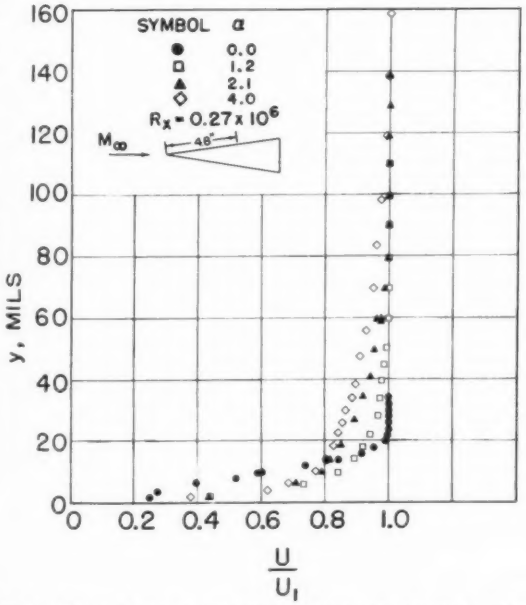

FIG. 2. Effect of yaw on velocity profiles on the leeward surface of a 15° cone at $M_\infty = 2.73$.

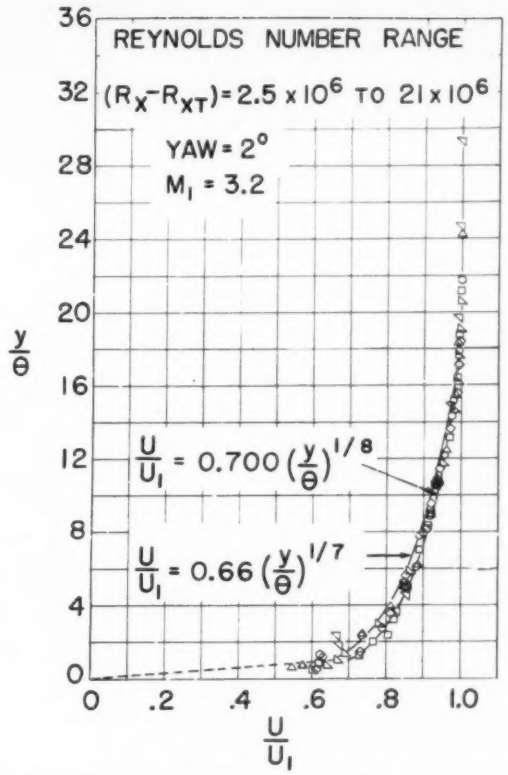

FIG. 3(a). Effect of variation of Reynolds Number at constant yaw.

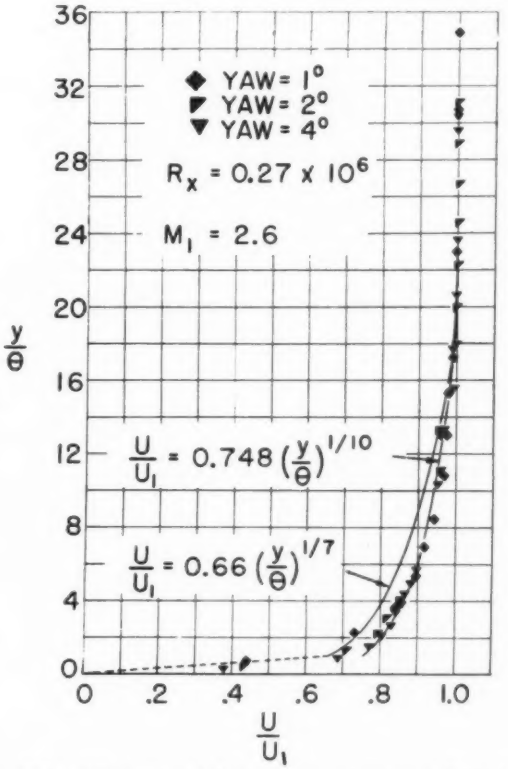

FIG. 3(b). Effect of variation in yaw at constant Reynolds Number.

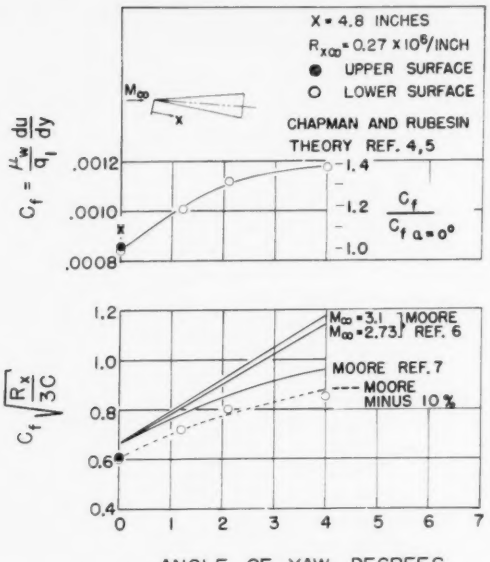

FIG. 4. Effect of yaw on local skin friction coefficient for laminar flow over a 15° cone at $M_\infty = 2.73$.

mixing characterizes the flow along the upper meridianal plane, at least at these small angles of yaw. It is of interest to note that the Reynolds Number $R_x = 0.27 \times 10^6$ for these experiments is far below that at which natural transition to turbulent flow occurs for smooth unyawed cones at this Mach Number. Obviously, it is the crossflow which triggers transition. Since the crossflow is an important factor here, one might expect R_θ to be a more meaningful correlation parameter in conjunction with some crossflow pressure gradient parameters than Reynolds Number based on x.

The results of Fig. 2 are replotted on Fig. 3(b) in the y/θ dimensionless representation. It is clear that the profiles are similar when so plotted.

Shown for comparison [Fig. 3(a)] are profiles taken at constant yaw but for a wide range of Reynolds Number.[2] The Mach Number in this case was $M_1 = 3.2$. Again, the profiles are similar despite the fact that measurements on both the windward and leeward sides are included.

Both sets of data are fitted by power profiles and are compared with the 1/7 profile chosen as characteristic of unyawed data in this range. For the data of Fig. 3(b), a 1/10 power profile seems suitable whereas for the data of Fig. 3(a), a 1/8 profile works very well. In the case of the 1/10 power profile, the crossflow pressure gradient is greater than for the data of Fig. 3(a) because the measuring station was closer to the cone tip.

Fig. 4 shows the experimental variation of laminar skin friction coefficients on the windward side with yaw at $M_\infty = 2.73$ on the 15° total angle cone. It can be seen from these results that the skin friction coefficient varies rapidly for $0 < \alpha < 1$ and that further increases in yaw have a less strong effect on skin friction coefficients. A comparison of these experimental results with theoretical analyses is shown.

When the angle of yaw of the cone increased to approximately one half the nose angle, separation of the boundary layer from the upper surface of the body starting from the tip occurred.[1]

REFERENCES

[1] DeCoursin, D. G., *An Experimental Study of the Effect of Small Angles of Attack on the Laminar Boundary Layer of a Cone*, University of Minnesota, Aeronautical Engineering Department, RR. 121, August, 1955.

[2] Bradfield, W. S., DeCoursin, D. G., and Blumer, C. B., *Characteristics of Laminar and Turbulent Boundary Layer at Supersonic Velocity*, University of Minnesota, Department of Aeronautical Engineering, RR. 83, July, 1952.

[3] Bradfield, W. S., *Research on Laminar and Turbulent Boundary Layers at Supersonic Speeds—Final Summary Report*, University of Minnesota, Aeronautical Engineering Department, RR. 131, December, 1957.

[4] Chapman, D. R., and Rubesin, M. W., *Temperature and Velocity Profiles in the Compressible Laminar Boundary Layer with Arbitrary Distribution of Surface Temperatures*, Journal of the Aeronautical Sciences, Vol. 16, No. 9, pp. 547–565, September, 1949.

[5] Hantzsche, W., and Wendt, H., *The Laminar Boundary Layer on a Cone in a Supersonic Airstream*, Translation RAT-6, Douglas Aircraft Co., Santa Monica.

[6] Moore, F. K., *Laminar Boundary Layer on a Circular Cone in Supersonic Flow at a Small Angle of Attack*.

[7] Moore, F. K., *Three Dimensional Laminar Boundary Layer Flow*, Journal of the Aeronautical Sciences, Vol. 20, No. 8, pp. 525–534, August, 1953.

[8] Allen, C. B., and Perkins, R. S., *A Study of Effects of Viscosity on Flow Over Slender Inclined Bodies of Revolution*, NACA Report 1048, 1951.

Boundary-Layer Equation for Axially Symmetric Flow . . .

(*Continued from page 634*)

is due to different methods of calculation. If our method of calculation is applied to Tomotika's data, the corresponding curve of friction obtained coincides with ours.

Up to $\theta = 50°$, we used the values of a corresponding to Hartree's solution; therefore, the curve of friction could not have lower values. Fage[4] calibrated his appliance to measure friction by using Tomotika's calculations. This should account, at least partially, for the difference between Fage's results and ours.

REFERENCES

[1] Meksyn, D., *The Laminar Boundary Layer Equations*, Proc. Roy. Soc., Series A, 192, p. 545, 1948.

[2] Goertler, H., *A New Series for the Calculation of Steady Laminar Boundary Layer Flows*, J. Math. and Mech., Vol. 6, No. 1, p. 1, 1957.

[3] Mangler, W., *Zusammenhang zwischen ebenen und rotationssymmetrischen Grenzschichten in compressiblen Flüssigkeiten*, Zeit. für angew. Math. & Mech., Vol. 28, p. 97, 1948.

[4] Fage, A., *Experiments on a Sphere at Critical Reynolds Numbers*, ARC R&M, London, No. 1766, 1937.

[5] Meksyn, D., *Integration of the Boundary Layer Equations*, Proc. Roy. Soc., Series A, 237, p. 543, 1956.

[6] Hartree, D. R., *On the Equation Occurring in Falkner and Skan's Approximate Treatment of the Equations of the Boundary Layer*, Proc. Cam. Phil. Soc., Vol. 33, p. 223, 1937.

[7] Falkner, V. M., and Skan, S. W., *Some Approximate Solutions of the Boundary Layer Equations*, ARC R&M, London, No. 1314, 1930.

[8] Tomotika, S., *Laminar Boundary Layer on the Surface of a Sphere in a Uniform Stream*, ARC R&M, London, No. 1678, 1935.